

Alma Mater Studiorum – Università di Bologna

**DOTTORATO DI RICERCA IN
GEOFISICA**

CICLO XXIX

Settore Concorsuale di afferenza: 04/A4-GEOFISICA

Settore Scientifico disciplinare: GEO/10-GEOFISICA DELLA TERRA SOLIDA

***Tracking space and time changes of physical properties in
complex geological media***

Presentata da: Grazia De Landro

Coordinatore Dottorato

Prof. Nadia Pinardi

Relatore

Prof. Aldo Zollo

Esame finale anno 2017

Abstract

An important issue in seismology concerns the characterization of the propagation medium, aiming to analyse the behaviour of rocks in relation to the generation of earthquakes (both natural and human-made). The basic idea is that seismic waves can be used to image the medium's physical properties.

In this context we placed our research project, concerning the reconstruction of the **spatial and temporal changes of physical properties** (*velocity, attenuation, rock parameters*) in **complex geological media**.

In the first part of this thesis we present a detailed description of known and new methodologies useful to track the seismicity, the propagation medium's features and their temporal variation. In particular, a new *rock modelling approach* is constructed, allowing the conversion of velocity and attenuation values in rock micro-parameters; and a new *equalization procedure* for the 4D tomography is developed, allowing at once to optimize the choice of time-windows in the case of massive data-sets and to completely handle seismic tomography issues.

In the second part, we show the results obtained by applying this methodologies to three complex areas: *the Irpinia fault zones, The Geysers geothermal area and the Solfatara volcano*. The relevance of these three areas lies not only in their different physical nature, but also in their different dimension. The obtained results show how the described methodologies can be used in seismogenic and volcanic areas to improve the knowledge of the medium's properties, in order to mitigate the risk associated to destructive events, and in geothermal areas, to monitor the induced seismicity through the tracking of the medium properties' temporal variation.

Therefore, this thesis represents a useful tool for the characterization of the propagation medium, by providing a compendium of different methodologies and by showing the results of their application to three complex areas characterized by different physical nature and dimensional scale.

Contents

<u>INTRODUCTION</u>	5
<u>PART ONE: METHODS</u>	8
<u>CHAPTER 1 : TRACKING SPACE CHANGES OF PHYSICAL PROPERTIES</u>	10
<u>1. INTRODUCTION</u>	10
<u>1.1 MACRO-parameters tracking</u>	12
<u>1.1.1 Seismic Velocity</u>	12
<u>1.1.1.1 Tomographic inversion strategy</u>	14
<u>1.1.1.2 Assessment of solution quality</u>	17
<u>1.2.1 Seismic Attenuation</u>	18
<u>1.2.1.1 t^* measurements</u>	19
<u>1.2.1.2 Tomographic inversion strategy</u>	20
<u>1.3 MICRO-parameters tracking</u>	21
<u>1.3.1 Rock physics modelling: up-scaling</u>	22
<u>1.3.2 Rock physics modelling: down-scaling</u>	28
<u>CHAPTER 2 : TRACKING TIME CHANGES OF PHYSICAL PROPERTIES</u>	31
<u>2. INTRODUCTION</u>	31
<u>2.1 FAST tracking methods</u>	35
<u>2.1.1 Station residuals variation tracking</u>	35
<u>2.1.2 V_p/V_s ratio variation tracking</u>	35
<u>2.2 COMPREHENSIVE tracking methods : Time-lapse tomography</u>	37
<u>CHAPTER 3 : TRACKING CHANGES OF SEISMICITY DISTRIBUTION</u>	42
<u>3 INTRODUCTION</u>	42
<u>3.1 3D double-difference earthquake locations</u>	43
<u>3.1.1 Relative location method</u>	44
<u>3.1.2 Synthetic tests</u>	46

<u>PART TWO: APPLICATIONS</u>	53
<u>CHAPTER 1 : IRPINIA FAULT SYSTEM</u>	56
<u>3.1 INTRODUCTION AND STATE OF ART</u>	56
<u>1.1 Geological settings</u>	59
<u>1.2 Seismic network and data</u>	61
<u>1.3 Station residuals variations</u>	62
<u>1.4 Absolute and double-difference location of micro-earthquakes</u>	65
<u>1.5 Attenuation tomography</u>	75
<u>1.5.1 Data processing</u>	75
<u>1.5.2 Inversion strategy</u>	76
<u>1.5.3 3D P- and S-wave attenuation tomography</u>	77
<u>1.5.4 Discussion</u>	83
<u>1.6 Rock physics modelling</u>	84
<u>1.6.1 Inversion strategy and comparison with attenuation images</u>	84
<u>1.7 Conclusion</u>	88
<u>CHAPTER 2 : THE GEYSERS GEOTHERMAL FIELD</u>	90
<u>2. INTRODUCTION AND STATE OF ART</u>	90
<u>2.1 Seismic network and data</u>	95
<u>2.2 3D P and S velocity models</u>	96
<u>2.3 V_p/V_s ratio temporal variation</u>	101
<u>2.4 Time-lapse tomography</u>	103
<u>2.5 Results and conclusion</u>	105
<u>CHAPTER 3 : THE SOLFATARA VOLCANO</u>	107
<u>3. INTRODUCTION</u>	107
<u>3.1 RICEN experiments and catalogue construction</u>	108
<u>3.2 State of the art</u>	109
<u>3.3 Velocity tomography</u>	110
<u>3.3.1 Data processing and inversion strategy</u>	111

<u>3.3.2</u>	<u>3D P and S velocity models</u>	115
<u>3.3.3</u>	<u>Resolution analysis</u>	118
<u>3.3.4</u>	<u>Multi-parametric analysis</u>	122
<u>3.3.5</u>	<u>Conclusion</u>	127
 <u>CONCLUSION</u>		128
 <u>REFERENCES</u>		133

Introduction

An important branch of geophysics, in particular of seismology, concerns the characterization of the propagation medium through the analysis of seismic waves. The basic idea concerns the fact that the ray path of the seismic waves is controlled by the physical properties of the crossed medium. These properties are influenced, among other things, by the presence and motion of fluids in the medium. Thus, seismic waves contain information on rock composition and fluid content, and can be used to image the physical characteristics of the medium. This characterization aims not only to get information about the composition and the geological structure of the subsoil, but also to analyse the rheological behaviour of rocks in relation to the generation of earthquakes.

In this context is placed our research project, which concerns the reconstruction of **space and time changes of physical properties** (*velocity, attenuation, rock parameters*) in **complex geological media** such as *tectonic, volcanic and geothermal environments*. The aim of the project is to investigate the influence of physical parameters in dynamic processes during the preparatory phase of earthquakes (both natural and human-made), by tracking the seismicity, the propagation medium features and their temporal variation.

With regard to the **spatial changes** of elastic and anelastic properties, *seismic tomography* has become a rather standard tool to investigate the variation of smooth velocity and attenuation in complex geological environments. The tomographic images allow to infer qualitative considerations about the geological characteristics of the medium and the presence of pore fluids (Nur and Simmons, 1969; Elliot and Wiley, 1975; Domenico, 1976; Toksoz et al., 1979; Thurber et al., 1995). We will present an iterative, linearized, tomographic approach in which the P and S arrival times are simultaneously inverted for the earthquakes location and velocity parameters (Latorre et al., 2004) to retrieve accurate 3D velocity images of investigated areas and the related resolution. Then, we will explain the procedure adopted in our analysis to modify the velocity code in order to obtain the 3-D attenuation quality factor Q images using as data the t^* parameter.

However, the reconstructed velocity and attenuation images do not allow to obtain any quantitative estimates about the physical micro-parameters of rocks, such as porosity, saturation or type of permeating fluids. In order to solve this issue, the first part of our research project incorporates the developing of a *rock physical modelling*, to apply downstream of velocity and attenuation tomography. This modelling allows to obtain

quantitative information about the rock micro-parameters through the direct inversion of the velocity and the attenuation values obtained through tomography.

In the interest of reveal the **temporal changes** of physical properties within rock volumes, the *4D seismic tomography*, i.e. a 3D seismic tomography repeated in different time windows, can be introduced. This approach has been used in tectonic (Chiarabba et al., 2009) geothermal and volcanic areas (Julian et al., 1998; Foulger et al., 2003; Gunasekera, 2003) and in hydrocarbon surveillance (Guerin et al., 2000). In order to optimize 4D seismic-difference anomalies, an equalization of the co-registered repeated data of the survey is required. When a permanent seismic acquisition network is available, the only equalization process concerns the different position of passive seismicity sources, and thus the equalization of the seismic images resolution in the different time windows. An important purpose of our research project concerned the methodological development of a new *equalization procedure in passive seismic* for the 4D tomography. The novelty of this procedure lies not only in its ability to optimize the choice of time-windows in the case of massive data-sets, but also in a complete handling of the issue associated to the seismic tomography, which includes the choice of inversion parameters, the choice of the optimal model parameterization, the analysis of the model resolution, etc.

To track the time changes of physical properties, the 4D tomography requires a long time-span to record a consistent data-set. Thus, in the second part of our research project, beside 4D tomography, we deal with "*fast*" methods that have the advantage of quickly computation as soon as the single seismogram is available.

Another seismic observable that can be related to fluid-flow in propagation medium is the seismicity pattern. Indeed, many authors (Nur and Booker, 1972; Hainzl, 2004; Antonioli et al., 2005; Hainzl and Ogata, 2005) test the hypothesis that the space distribution and temporal evolution of seismicity can be used to analyse the presence and diffusion of a pore-pressure perturbation in a poro-elastic fluid saturated medium. It is clear that an accurate knowledge of the seismicity pattern is crucial in these analyses in terms of space and time location. A small part of this research project focused on providing a high accurate probabilistic *double-difference earthquake location method*, which allows the use of a 3D velocity model for location in complex media. The main advantages of this method are the determination of comprehensive and complete solutions through the probability density function (PDF), the use of differential arrival times as data and the possibility to use a 3-D velocity model for both absolute and double-difference locations, all of which help to obtain accurate differential locations in structurally complex geological media.

In addition to the analysis and development of different methodologies, an important aspect of our research project concerns the application of these methods to **three complex areas: the Irpinia fault zones, The Geysers geothermal area and the Solfatara volcano**. The relevance of these three areas lies not only in their different rheological and structural nature, but also in their different dimensional scale. These different features enable us to consider the areas as "*seismological laboratories*", i.e. areas of interest which allow the application, validation and development of different methodologies.

The Thesis is organized in two different parts: methods and applications.

PART I (methods) is subdivided in three chapters, regarding the description of the methodology used to track the changes of the medium's properties in space (Ch. 1) and time (Ch. 2), and the distribution of seismicity (Ch. 3). The first chapter incorporates the seismic velocity and attenuation tomography and the rock physical modelling. The second chapter contains a description of "fast" and comprehensive methods, such as 4D tomography, which aim to track the time variation of the medium's properties. Finally, in the third chapter we present the highly accurate 3D double-difference location method that aims to track the space and time variation in the seismicity pattern.

PART II (application) is organized in three chapters, each one regarding a different investigated area: the Irpinia fault zones (Ch. 1), The Geysers geothermal area (Ch. 2) and the Solfatara volcano (Ch. 3). Depending on the characteristics, the available data-sets, the associated problems and the state of art of each area, we have chosen to apply several of the methods of analysis and investigation explained in part I. Thus, the three chapters contain the application and results of different methodologies to the three complex areas.

PART ONE: METHODS

The study of the earthquake nucleation phase is one of the most important topics in the seismological community (Lee and Delaney, 1987; Ellwort and Beroza, 1995; Dodge et al., 1995; Kanamori, 2005; Olson and Allen, 2005), and its aim is the monitoring of seismogenic areas for the prevention/prediction of seismic events, which always cause huge losses in social and economic terms. There are different points of view from which we can analyse this issue. In our case, the study of the preparatory phase of earthquakes is done by measuring the spatial and temporal variations of the propagation medium physical properties in the region of seismic sources (Nur, 1972; Kisslinger and Engdahl, 1973; Whitcomb et al., 1973; Chiarabba et al., 2009b; Lucente et al. 2010; Valoroso et al., 2011).

First-arrival travel time tomography can be used to image the Earth's interior at various scales, from near-surface to global, by using active and passive sources. The velocity tomographic models allow to image the physical properties of the host environment and the effects of pore-fluid on them (Nur and Simmons, 1969; Elliot and Wiley, 1975; Domenico, 1976; Michael and Eberhart-Phillips, 1991). Moreover, attenuation tomography may provide useful and complementary insights on the physical properties of fluids permeating host rocks (Hauksson and Shearer, 2006). However, the above observables (i.e. velocity and attenuation parameters) cannot single out a quantitative estimation of rock parameters, like porosity or saturation (Dupuy et al., 2016), which can be obtained only by using the physical modelling of a rock.

Is well known that the transient processes occurring along active faults, such as fluid migration and pore pressure changes, are thought to promote the occurrence of moderate to large earthquakes (Nur and Booker, 1972; Scholz et al., 1973; Sibson, 1992; Cox, 1995; Caine et al., 1996; Antonioli et al., 2005). In addition, fluid migration and pore pressure changes can provoke transient variations of the medium elastic and anelastic properties. Thus, the complex processes that can trigger seismicity may be monitored by tracking the temporal variation of physical parameters. 4-D tomography in space and time represents a very comprehensive method to track the spatio-temporal variation of parameters (Gunasekera et al., 2003; Foulger et al., 2003; Patanè et al., 2006; Chiarabba et al., 2009b; Lin and Shearer, 2009; Julian and Foulger, 2010). Beside the 4D tomography, "fast" methods can be used, with the advantage that the temporal variation of parameters is quickly computed, that is, as soon as the seismogram is available (Chiarabba et al., 2009; Valoroso et al., 2011).

Finally, the relationship between fluid-flow and seismicity patterns is well known (Nur and Booker, 1972; Hainzl, 2004; Antonioli et al., 2005; Hainzl and Ogata, 2005). Thus, the spatial distribution and temporal evolution of seismicity can be used to analyse the presence and diffusion of a pore-pressure perturbation in a poro-elastic fluid-saturated medium. In order to ensure the high precision of earthquake location, we present a new probabilistic, double-difference location method, which allows the joint use of differential time, to minimize the error due to the uncertainties of the velocity model, and a 3D velocity model, in order to take into account the lateral heterogeneity in complex areas.

In this first part of the thesis we present the different methodologies that have been analysed and/or developed in our research project. In detail, the first chapter regards the tracking of the spatial changes of the elastic and anelastic parameters, i.e. velocity and attenuation, through seismic tomography. Moreover, in this chapter a rock physical modelling allowing the conversion of tomographic information in rock micro-parameters is presented in details. The second chapter concerns the tracking of the temporal changes of physical properties. This chapter contains the detailed explanation of the new equalization procedure for the 4D tomography, which must be applied to the passive-seismic data-sets, and of two “fast” methods that allow to rapidly monitor the temporal variation of parameters. Finally, in the third chapter we present the new highly-accurate double-difference location method that allows the use of the 3D velocity model in complex media.

Chapter 1: *Tracking SPACE changes of physical properties*

1. Introduction

The knowledge of the soil geological characteristics, especially regarding the presence of fluids, is nowadays an important issue concerning both the environmental (natural risks, geotechnics, groundwater pollutions, etc.) and resources (aquifers, oil and gas, CO₂ storage, etc.). Because of the erosion and deposition process, the porous materials represent a large part of the upper crust geological structures. These are mainly characterized by empty interstices, between the granules of the solid matrix, filled with fluids, which modify the rheological characteristics of the multiphase porous media. Seismic waves traveling through the Earth's crust are greatly distorted by these rheological heterogeneities and therefore contain information on the rock composition and fluid content. Hence comes, the idea to characterize the propagation medium in terms of porosity and fluids composition by using the velocity and attenuation (visco-elastic) parameters obtained by first-arrival travel time seismic tomography.

In recent years, first arrival time tomography has become a standard tool to investigate the smooth velocity variations in complex geological environments. The velocity tomography allows to obtain 3D images of investigated areas. Those models allow to study the relationship between the behaviour of a fault and the physical-mechanical properties of the host environment (Michael and Eberhart-Phillips, 1991). The effect that pore fluids have on seismic velocities is well documented (Nur and Simmons, 1969; Elliot and Wiley, 1975; Domenico, 1976). In particular, Thurber et al. (1995) emphasized the relationship between the V_p/V_s parameter and the changes in the physical properties of the rocks in seismogenic areas.

Beside to velocity images, attenuation tomography may provide useful and complementary insights on the physical properties of fluids permeating host rocks (Hauksson and Shearer, 2006). Although not yet a routine tool, attenuation tomography using local or regional seismicity and artificial sources has been well known for a number of years. The approaches used for calculating the spatial distribution of attenuation vary depending on whether one considers the inversion scheme (Ho-Liu et al., 1988; Shukri and Mitchell, 1990) or the calculation of the whole path attenuation (Evans and Zucca, 1993; Lees and Lindley, 1994).

Toksoz et al (1979) showed, through laboratory measurements, how the attenuation of P- and S-wave in rocks strongly depends on the physical state and saturation, rather than on the

seismic velocities. In particular, the Q_s/Q_p ratio can reveal the types of attenuation mechanisms and the possible effects of the crustal fluids percolation and migration on body wave anelastic attenuation (Hauksson and Shearer, 2006).

Rock physics can be used to link the P-wave and S-wave velocity and attenuation models, obtained from earthquake travel-time inversion, to rock properties. In fact, rock physics provides the link between rock and fluid properties and seismic response. There are numerous empirical models, relating the P and S wave velocities to rock properties like density (ρ) or porosity (φ) (Wyllie et al., 1956; Han et al., 1986; Raymer et al., 1980; Castagna et al., 1993; Dvorkin et al., 1995; Brocher, 2005). However, these models are strongly dependent on the rock lithology and are very simplified, since the wave velocity only depends on porosity (or on density). Since we are interested in investigating complex porous media characterized by different lithologies, we have developed an approach based on the Pride (2005) poro-elastic rock modelling, which is valid within a wide range of frequencies and consolidated rock lithologies.

By combining seismic imaging methods and rock physics models, we developed a two-step method in order to evaluate the poroelastic micro-parameters of the host porous medium. In the first step, we use the seismic imaging technique in order to obtain visco-elastic effective macro-parameters (velocity and attenuation). From these visco-elastic parameters, we develop an up-scaling method, based on Biot's theory (1956), in order to estimate micro-scale properties (porosity, mechanical moduli, fluid phase properties, and saturation) through the direct comparison between observed and up-scaled macro-parameters.

Finally, we plan to develop a complete inversion procedure of the velocity and attenuation models in order to obtain the corresponding images of micro-parameters, and therefore to infer a complete interpretation about the physical state of the hosting porous medium.

In the first two paragraphs we describe the method that allows macro-parameters tracking, i.e. velocity and attenuation tomography, detailing the general problem, the inversion strategy and the assessment of solution quality. The third paragraph concerns the micro-parameter tracking. It contains the description of rock physical modelling for the up-scaling procedure, and the related down-scaling procedure for the complete inversion.

1.1 MACRO-parameters tracking

First-arrival travel time tomography can be used to image the Earth's interior at various scales, from near-surface to global, by using active and passive sources. For seismic imaging, the determination of the near-surface velocity structure is a key step when trying to image deeper structures. After the Aki and Lee (1976) work, earthquake location and tomography have become widely used means to deduce active and passive structures of the Earth's interior from the available seismological data. In particular, by using seismological observables, such as the arrival time of the P and S primary seismic waves and their attenuation measured in the frequency domain through the parameter t^* (i.e. the ratio between the time of the first arrival of seismic phases and the quality factor Q), it is possible to perform a 3D imaging, thus obtaining the velocity and the attenuation structure of the crust.

The imaging of crustal seismic velocity provides significant constraints on the physical properties of host rocks and on the potential presence of fluids, in particular in the volume embedding fault systems. Indeed, the contribution of pore fluid in pressure changes to earthquake triggering at different rupture scales is recognized worldwide (Hardebeck and Hauksson, 1999; Husen and Kissling, 2001). Fluid movements can be tracked by analysing V_P/V_S ratio space-time changes (e.g. Hamada, 2004; Chiarabba et al. 2009; Lucente et al, 2010; Valoroso et al. 2011).

Seismic attenuation studies provide important independent constraints on Earth properties since their sensitivity to temperature, fluids, compositional differences, and other rock properties (Toksoz et al., 1979; Hauksson and Shearer, 2006) complementary from that provided by P- and S-wave velocities. Tomographic inversions are now commonly applied to determine the three-dimensional attenuation (quantified by $1/Q$) structure in a manner comparable to velocity tomography.

However, the above observables (i.e. velocity and attenuation parameters) cannot single out, for example, the type of fluid mixing and the relative percentage of saturation (Dupuy et al., 2016), which are necessary factors to define a reliable picture of the host rock physical properties.

1.1.1 Seismic Velocity

The propagation velocity of the waves depends on density and elastic moduli of the medium.

The P-wave velocity is related to the elastic properties of the medium by the following expression:

$$v_p = \sqrt{\frac{K + 4/3\mu}{\rho}} \quad (1)$$

where K is the bulk modulus, μ is the shear modulus and ρ is the density. The S-wave velocity can be related to the elastic properties of the medium by the following expression:

$$v_s = \sqrt{\frac{\mu}{\rho}} \quad (2)$$

S waves propagate through materials more slowly than P waves. In addition, S waves cannot propagate through fluids, as fluids do not support shear particle motion.

The bulk modulus, shear modulus and density depend on the mineralogy and structure of a rock, its porosity, the pore fluid type and the related saturation. Thus, these are the parameters that affect the seismic P- and S-wave seismic velocities.

The body wave travel time T from an earthquake i to a seismic station j is expressed using ray theory as a path integral (Thurber, 1993)

$$T_{ij} = \int_{source}^{receiver} u ds \quad (3)$$

where u is the slowness field (reciprocal velocity) and ds is the elementary path length. The real observations are the arrival times t_{ij} , where

$$t_{ij} = \tau_i + T_{ij} \quad (4)$$

and τ_i is the earthquake origin time.

In order to obtain the arrival time of a phase (picking), the common procedure involves the manual measuring of P- and S- arrivals on recordings of a single event at a time. However, the growing number of dense seismic monitoring networks installed in areas of high seismicity offers a continuously increasing availability of high-quality three-component recordings which has motivated the study of techniques for automatic picking. The approaches to automatic picking can be divided into main categories. The first one is to analyse a single

event at a time doing the picking on each seismogram independently from the others (Allen, 1978; Diehl et al., 2009; Dai and MacBeth, 1997). A second approach works on several seismograms at once, exploiting the similarity of waveforms from nearby events (Rowe et al., 2002). This approach can be used on the manually picked data-sets in order to obtain highly accurate readings.

1.1.1.1 Tomographic inversion strategy

In terms of inverse problem theory (Menke, 1989) the observed arrival times are the data, while the source coordinates, the origin times, the ray-paths, and slowness field are the unknowns (model parameters). Given a set of arrival times t_{ij}^{obs} measured at a network of stations, the calculated arrival times t_{ij}^{cal} are determined from equations 3.1 and 3.2 using trial hypocenters and origin times and an initial seismic velocity model. The mistfit between observed and predicted (calculated) arrival times are then the residuals r_{ij}

$$r_{ij} = t_{ij}^{obs} - t_{ij}^{cal} \quad (5)$$

The residuals can be related to the desired perturbation to both the hypocentre than to the velocity model by using a linear approximation

$$r_{ij} = \sum_{k=1}^3 \frac{\partial T_{ij}}{\partial x_k} \Delta x_k + \Delta \tau_i + \int_{source}^{receiver} \delta u ds \quad (6)$$

All the linearized local earthquake tomography methods are based on equation 3.4 and then diversify to some extent, according to different treatment of some or all of the following aspects of the problem:

- the scheme adopted for representing of the velocity model;
- the technique for travel time and ray-path calculations;
- the treatment of the hypocentre-velocity structure coupling;
- the inversion procedure.

The tomographic inversion method used by Latorre et al., (2004) is based on an iterative scheme operating on a linearized delay-time inversion to estimate both velocity models than earthquake locations. Slowness is modelled via trilinear interpolation on a 3D regular grid (the inversion grid. First arrival travel times of wavefronts are computed through a finite-difference solution of the eikonal equation (Podvin and Lecomte, 1991) in a finer grid. For each source-receiver pair, travel times are recalculated by numerical integration of the slowness on the inversion grid along the rays traced in the finite-difference travel time field.

At each node of the inversion grid, travel time Fréchet derivatives are computed for the P and S slowness, hypocentre location and origin time.

The parameters are inverted using the damped LSQR method (Paige and Saunders, 1982). It consists in finding a solution in the sense of least squares, which searches for the vector x which minimizes the function

$$\min \|Ax - b\|_{L2} \quad (7)$$

Since the problem is underdetermined the solution may not be unique; it is therefore necessary to introduce regularization as an additional condition that allows the convergence towards a single solution. A classical approach to solve the underdetermined problems is to search for a solution in sense of the damped least-squares (Menke, 1989). The system to be solved becomes

$$\begin{pmatrix} A \\ \epsilon I \end{pmatrix} x = \begin{pmatrix} b \\ 0 \end{pmatrix} \quad (8)$$

where I is the identity matrix and ϵ is the parameter that controls the damping level. This parameter defines the damping of the perturbation amplitudes compared to the reference model, otherwise known as the distance between the initial parameters and the final parameters of the model. This value in turn controls the relationship (trade-off) between the standard deviation of the data (misfit) and the variance of the model obtained. The equation (7) can be written as

$$\min \|Ax - b\|_{L2} + \|\epsilon Ix\|_{L2} \quad (9)$$

and the final solution is

$$\vec{x} = (A^T A + \epsilon^2 I)^{-1} A^T b = A^{-g} b \quad (10)$$

Where A^{-g} is the generalized inverse (Backus & Gilbert, 1970). The damping parameter defines the perturbation amplitudes in accordance with the reference model, i.e. the distance between the initial parameters of the model and final parameters. Model roughness is bonded imposing that the Laplacian of the slowness must vanishes during the inversion procedure (Benz et al., 1996; Menke, 1989).

Each iteration consists of the following operations:

- trilinear interpolation of the velocity model on a finer grid;
- calculation of the theoretical arrival times with the finite difference technique of Podvin and Lecomte (1991), in order to obtain a first estimate for each station of the travel time at each node of the finer grid;
- ray tracing technique of back ray-tracing for each source-receiver pair along the gradient of the travel time estimates;
- accurate calculation of the travel time field by integrating slowness along the ray path;
- calculation of the Fréchet derivatives of the travel time field simultaneously for P and S slowness, hypocentral coordinate and origin time of earthquakes;
- preconditioning and smoothing of the matrix of derivatives. The first is the normalization and scaling of the matrix of derivatives in order to control the quality of the estimated parameters. This operation is controlled by a set of four hyper-parameters, one for each class of estimate parameters. The smoothing is achieved by requiring that the Laplacian of the slowness field counts zero (Benz et al., 1996);
- inversion of linear system of equations, scaled and weighed, with the algorithm LSQR (Paige and Saunders, 1982).

The regularization of the inversion is achieved through the damping factor. The chosen value is the damping for which a small variance in the data corresponds to a small variance in the model, for each of the four classes of parameters simultaneously. To determine the optimal combination of hyper-parameters we performed sensitivity tests, i.e. synthetic tests using the real earthquakes-station configuration and the same parameters chosen for the tomographic inversions.

The velocity model is parameterized by a nodal representation, described by a tridimensional grid. Since no single scheme can faithfully represent all the aspects of the crustal heterogeneities, a good inversion strategy is a multiscale approach: a series of inversions is carried out refining the velocity grid progressively, the starting model for each inversion being the final model of the previous one. This procedure, which was first introduced for velocity estimation by Lutter et al. (1990), allows us to determine the large-scale components of the velocity model and then to progressively estimate the smaller-scale components.

1.1.1.2 Assessment of solution quality

To assess the reliability of the final solution, the resolution matrix may be numerically computed. The full resolution matrix is calculated starting from the tomographic matrix using the relation:

$$R = A^{-g}A \quad (11)$$

The full resolution matrix is represented in terms of its resolution diagonal elements RDE and the spread function S_j (Micheline and McEvelly, 1991) related to off-diagonal elements. The S_j is defined as:

$$S_j = \log \left(|s_j|^{-1} \sum_{k=1}^N \left(\frac{s_{kj}}{|s_j|} \right)^2 D_{jk} \right) \quad (12)$$

where s_j is the L2 norm of diagonal j element of resolution matrix, and can be interpreted as a weighting factor that takes into account the value of the resolution kernel for each parameter, s_{kj} is the elements of j -th row of resolution matrix, and D_{jk} is the distance between model parameter j and k . So, S_j is calculated by compress each row of the resolution matrix into a single number, which describes how peaked is the resolution for the corresponding diagonal element. The lower the S_j the more peaked is the resolution.

In addition to RDE and S_j , we used for the definition of resolved area the derivative weight sum (DWS), that measures the ray density in the neighbourhood of every node. Therefore, we used the DWS as a measure of the information density provided by the ray coverage. The DWS of the n -th V parameters is defined as

$$DWS(V_n) = N \sum_i \sum_j \left\{ \int_{P_{ij}} \omega_n(x) ds \right\} \quad (13)$$

where i and j are indices for event and station ω_n is the linear interpolation weight that depends on coordinate position, P_{ij} is the ray path from i to j , and N is the normalization of the volume influenced by V_n (Tomey and Fougler, 1989). The ray-path P_{ij} is computed into the final model obtained by observation, and take into account the real ray-path geometry.

1.2.1 Seismic Attenuation

The seismic waves propagating across the Earth crust undergo energy dissipation processes, which cause their amplitude to attenuate as a function of travel distance and wave frequency.

There are several different theories explaining the pore fluid attenuation mechanism. Mavko and Nur (1979) proposed a model in which liquid droplets in a partially saturated crack flow in response to crack compression or dilatation. Kjartansson and Denlinger (1977) have presented a model in which the compression of pore fluid gaseous phase causes the adiabatic heating of the gas followed by an irreversible flow of heat into the rock and pore water. Those two mechanisms predict that attenuation should increase with the degree of saturation and then rapidly decrease at total saturation. For fully saturated rock, O'Connell and Budiansky (1977) proposed a model which involves "squirting" flow between cracks because, having different orientations with respect to the passing wave and aspect ratios, they undergo differential compression. This shows that the mechanism may cause significant shear attenuation over a broad frequency range, and that shear attenuation should be much larger than compressional attenuation.

Johnston et al (1979), through the application of these models to the ultrasonic data of Toksöz et al (1979), showed that friction on thin cracks and grain boundaries is the dominant attenuation mechanism for consolidated rocks under most conditions in the Earth's upper crust. Increasing pressure decreases the number of cracks contributing to attenuation by friction, thus decreasing the attenuation. Water wetting of cracks and pores reduces the friction coefficient, facilitating the sliding and thus increasing the attenuation. In saturated rocks, fluid flow plays a secondary role in friction.

These models shows how the attenuation of P- and S-wave in rocks strongly depends on the physical state and saturation condition, and how it generally varies much more than the seismic velocities as a result of the changes in the physical state of materials (Toksoz et al 1979).

The parameter which describes the anelastic attenuation is the quality factor Q , measuring the fraction of energy that is lost per wave cycle through the friction phenomena occurring during the wave propagation from a source at depth to the receiver placed at the Earth surface. The quality factor Q is linked to the coefficient t^* via the formula:

$$t^* = \int \frac{dl}{vQ} \quad (14)$$

where dl is the ray element and the terms Q and v are the quality factor and the velocity along the ray path, respectively.

1.2.1.1 t^* measurements

t^* is the most used parameter to evaluate the effect of the anelasticity in the Earth.

Different are the technique that allowing the measure of this parameter. Here we mainly focus on frequency domain based techniques.

The displacement spectrum U of a seismic signal is described as:

$$U(f) = S_0(f)G(f)R(f)I(f) \quad (15)$$

The function $S_0(f)$ describes the source spectrum, $G(f)$ accounts for the geometrical spreading, the radiation pattern and the anelastic body-wave attenuation along the travel path, and $R(f)$ is the site transfer function. Lastly, $I(f)$ is the instrument response curve.

The attenuation function $G(f)$ is:

$$G(f) = C'_s e^{-\pi f t^*} \quad (16)$$

where a distance-dependent term C'_s accounts to direct P and S-wave amplitude variations due to the velocity structure. t^* measurement from spectrum analysis, as suggested by equation (2), needs the removal of the frequency-dependent contribution of site transfer function, instrumental response and source spectrum. Both the instrumental response and the site transfer function may be de-convolved or considered as a constant static factor in the whole frequency range of interest.

In their work on source parameters calculation along the Irpinia Fault zone, Zollo et al. (2015) used two different approach to calculate the t^* for earthquake grater or smaller than $ML=1.0$. For small magnitude earthquakes (e.g. $ML < 1.0$) t^* is has been determined from the low-frequency spectral decay in a frequency band whose upper limit is given by the event corner frequency. For the larger events in the data-set, t^* is was instead computed by using a multi-step, iterative inversion of spectral parameters (i.e. Ω_0 , ω_c , γ , and t^* in figure 1; Zollo et al., 2015).

For active seismic data, the cross-correlation of the sweep with velocity seismograms allows to properly remove the source contribution to provide the Green's functions of the propagation medium (Brittle et al., 2001). Then, the natural logarithm of the displacement spectrum yields can be computed as:

$$\ln U_{i,j}(f) = \ln(C'_s) - \pi t_{i,j}^* f \quad (17)$$

where i, j are the indices for source and station, respectively. The spectral decay produced by the anelastic attenuation may be fit in the least-squares sense. The attenuation parameter t^* may be inferred from the slope of the best-fit curve of the spectrum (Figure 1).

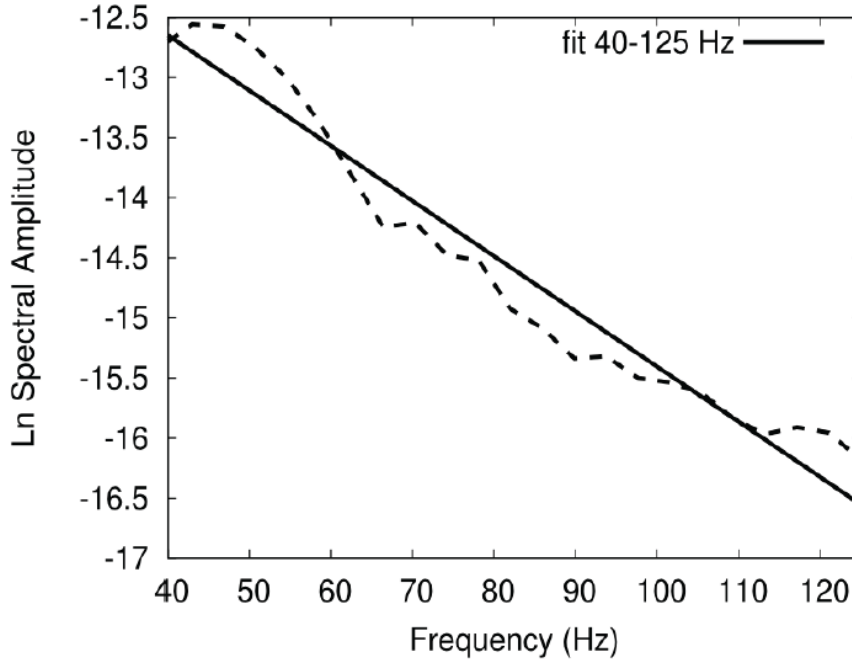


Figure 1. t^* measurement by means of a fitting procedure. Example of a displacement spectrum (dashed line) plotted in a log-linear scale and fit in the least-squares sense in the frequency range 40-125 Hz.

1.2.1.2 Tomographic inversion strategy

If the velocity model is known and the t^* parameter has been estimated along the corresponding path, the 3-D attenuation quality factor Q of the medium along this path could be solved by an appropriate inversion method. The usual assumption is that the velocity model is fixed, so ray paths do not change during the inversion procedure and the problem is linear from a mathematical point of view.

In order to perform the 3D tomographic inversion of t^* data, we have adapted the code originally developed by Latorre et al. (2004) and used by Amoroso et al. (2014) in order to retrieve the velocity model of the area under examination.

To obtain an attenuation model, we used the residual of t^* , $\delta t^* = t^{*obs} - t^{*cal}$, that can be expressed as a function of partial derivatives, by the formula

$$\delta t^* = \frac{\partial t^*}{\partial(1/v)} \delta \left(\frac{1}{v} \right) + \frac{\partial t^*}{\partial(1/Q)} \delta \left(\frac{1}{Q} \right) \quad (18)$$

To determine the parameter Q we modified the code of Latorre et al. (2004). Both the velocity than the hypocentre parameters are kept fixed during the inversion. The modifications of the algorithm preserve the inversion procedure, but they imply changes concerning inputs and computation of the Fréchet derivatives. In particular the entire inversion procedure can be summarized in successive steps, as follows:

- ray-tracing in the fixed velocity model (*a priori* known from previous analyses) for all the station-event couple for which t^* are available;
- calculation of the theoretical t^* by the integral formulation (x), and residuals $\Delta t^* = t_{obs}^* - t_{cal}^*$;
- set up of the equations system to solve by matrix inversion;
- smoothing of the matrix (Benz et al., 1996);
- inversion of the matrix system $\Delta t^* = H\delta\eta$, where Δt^* is the matrix of the residuals, H is the Fréchet derivatives matrix, and $\delta\eta$ is the matrix of the attenuation perturbation, using the LSQR method (Paige and Saunders, 1982);
- once we get the Q attenuation model, the RMS of residuals is evaluated, and if these values are below a given threshold the final model is obtained, otherwise the procedure is reiterated from item 2 onwards.

As in the velocity tomography case, to assess the reliability of the final solution, the resolution matrix may be numerically computed. Moreover, in addition to RDE and S_j , we used for the definition of resolved area the derivative weight sum (DWS), that measures the ray density in the neighbourhood of every node. The details about these quantities can be found in previous 1.1.1.2 paragraph.

1.3 MICRO-parameters tracking

In the past decades, velocity and attenuation seismic tomography have been used to image the spatial variation of elastic/anelastic rock properties within complex geological media. Then, these properties were qualitatively interpreted in terms of fluid presence and migration within the considered crustal volume (Di Stefano et al 2009, Amoroso et al 2014, Zucca et al 1994, Gunasekera et al 2003, Husen et al 2004, Hakusson and Shearer 2006). In these works, the inferences about pore fluid and the physical condition of the host medium are made from the trends of V_p/V_s and Q_s/Q_p ratio on the basis of laboratory measurements.

Although these works are based on widely accepted methodologies, the inferred information are entirely qualitative, or are derived from the comparison with laboratory results which do not take into account the complexity of the physical conditions of the analysed media. If we are interested in a quantitative interpretation of seismic attributes in terms of micro-parameters values, we need to introduce the poro-elastic rock modelling, taking into account as far as possible the complexity of the host medium physical condition.

There are numerous empirical models, which relate the P and S wave velocities to rock properties like density (ρ) or porosity (φ) (Wyllie et al., 1956; Han et al., 1986; Raymer et al., 1980; Castagna et al., 1993; Dvorkin et al., 1995; Brocher, 2005). However, these models are strongly dependent on the rock lithology and the P-wave velocity depends only on porosity (or density) without taking into account the drained medium rigidity or the possible saturation in fluids (gases or liquids) which play an important role in constraining the macro-parameters (Dupuy et al., 2016).

During my internship at ISTERre, l'Istitut des Sciences de la Terre at the J. Fourier University of Grenoble, we developed an approach based on the poro-elastic, rock modelling developed by Pride (2005), which is valid within a wide range of frequencies and consolidated rock lithologies.

Pride (2005) identifies connections between effective parameters at the mesoscale and macroscale seismic parameters obtained by seismic imaging. These connections provide the basis for our reconstructions of the mesoscale effective-medium parameters starting from inverted velocities and attenuation values. That is, we assume that the effective two-phase parameters can be reconstructed from seismic velocities and attenuation values and that these quantities also can be up-scaled from multiphase microscale rock physics.

1.3.1 Rock physics modelling: up-scaling

Using the effective medium theory and the Biot-Gassmann theory, we performed an up-scaling modelling to predict the expected macro-parameters for a given host rock characterized by a set of micro-parameters which would describe the physical properties of the solid and fluid phases. In particular, we have considered possible saturations with combination of different types of fluids, gases and liquids, permeating the investigated rock volume. The final aim is the evaluation and the characterization of the possible fluid saturation from the direct comparison between the up-scaling predicted values of the macro-parameters (P and S velocities and attenuation parameters and their respective ratios) and those ones inferred from the velocity and attenuation tomography. Our approach allows calculating the macro-parameters from the dry rock properties. The Biot's theory deals with the elasticity of a two-phase medium: a solid, permeable, skeleton saturated with viscous

fluid. The Gassman relations provide the estimates of the bulk modulus of the drained medium during a fluid substitution. The Biot-Gassmann relations are applicable under the following assumptions: a) the mechanical moduli are computed at low frequency, i.e., in static conditions; b) the medium is assumed to be isotropic; c) the frame consists of identical grains and the pores are saturated with a single fluid phase. Pride (2005) extended this theory to the dynamic cases, in the hypothesis of signal wavelengths larger than grain size.

Since we are interested in examining porous rocks composed by different solid phases and saturated with different fluid phases, the description of porous media requires a homogenization approach of both fluid than solid phases at the meso-scale, halfway between the macro-scale related to seismic waves and the micro-scale related to rock physics. Homogenization allows us to extract subseismic-scale information without involving the intrinsic complexities related to detailed rock-physics description (Chopra and Marfurt, 2007; Mavko et al., 2009). For this purpose we used the effective medium theory (e.g., Burridge and Vargas, 1979; Berryman, 1980a, 1980b), which allows homogenizing the multi-phase saturated medium to obtain an equivalent single fluid, which saturates the solid skeleton at the meso-scale.

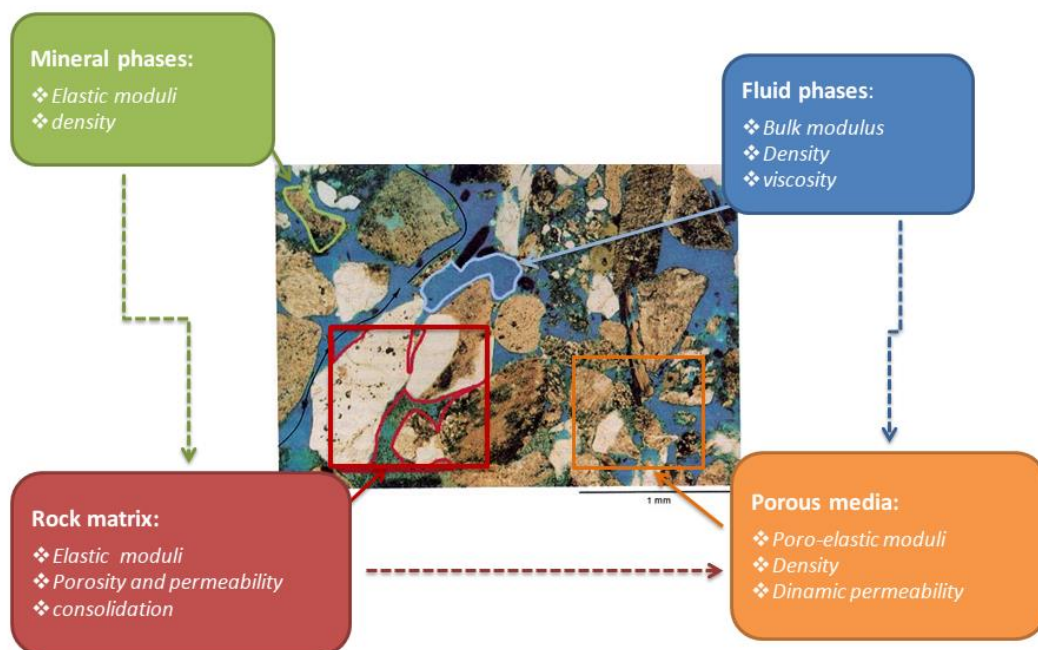


Figure 2. Thin section of rock sample under the microscope. The different boxes indicate the phases making up the porous medium and their characteristic parameters: in green the mineral phases; in blue the fluid phases; in red the rock matrix composed by the homogenization of mineral phases; in orange the porous media composed by the homogenization of fluid and solid phases.

The parameter that defines respective proportions of fluid and solid phases is the porosity $\varphi = V_V/V_T$, i.e. the ratio between void and total volumes. The parameters describing fluids and associated flows through the solid matrix are a un-compressibility modulus K_f , a density ρ_f and a viscosity η . A non-viscous fluid has a viscosity η equal to zero. The viscosity can be introduced with the intrinsic permeability k_0 introduced in the Darcy's law. Auriault et al. (1985) and Johnson et al. (1987) generalized this law with a dynamic permeability $k(\omega)$ depending on the pulsation ω (assuming a time dependency in $e^{-i\omega t}$). This permeability, which is a complex number, is defined through the dispersive relation:

$$k(\omega) = \frac{k_0}{\sqrt{1 - iP \frac{\omega}{\omega_c} - i \frac{\omega}{\omega_c}}} \quad (19)$$

and at low-frequencies is exactly the hydrological permeability k_0 of the sample, while at high frequencies it includes inertial effects associated with relative fluid-solid movement (Pride, 2005).

The non-dimensional number P is equal, by default, to 0.5 but it hasn't much influence on the seismic frequency bands (Pride, 2005). The separation between the low frequency domain, where viscous effects are dominant, from the high frequency one, where inertial effects prevail, is given by cut-off pulsation ω_c . Using Archie's law, the pulsation ω_c is defined as:

$$\omega_c = \frac{\eta}{\rho_f k_0 \varphi^{-m}} \quad (20)$$

where m is the cementation exponent, related to the electrical cementation factor and to the pore tortuosities (Brown, 1980). Then, the dynamic loss of energy due to the fluid flow with an explicit frequency dependence can be introduced as the flow resistance density term $\tilde{\rho}$. This term is responsible for the intrinsic scattering of waves in the Biot poroelasticity theory (Biot, 1956) and it is expressed in the frequency domain as:

$$\tilde{\rho} = \frac{i\eta}{\omega k(\omega)} \quad (21)$$

Considering the solid skeleton, this is entirely described by the association of grains in a solid matrix. The grains are characterized by an un-compressibility modulus K_s , a shear solid modulus G_s and a solid density ρ_s . If different mechanical structures exist in the skeleton, we assume that a homogenization has already been performed. In consolidated media, this solid skeleton is described by an un-compressibility drained modulus K_D , a shear modulus G and a consolidation parameter c_s , which describes the degree of consolidation of solid matrix grains,

larger values representing less consolidated rocks (Pride, 2003). With the help of the porosity, empirical formulae (Pride, 2005) defined as:

$$K_D = K_S \frac{1 - \varphi}{1 + c_s \varphi} \quad (22)$$

$$G = G_S \frac{1 - \varphi}{1 + \frac{3}{2} c_s \varphi} \quad (23)$$

links mineral properties to the parameters that characterize the skeleton itself. The consolidation parameter c_s and the porosity φ are key ingredients for up-scaling constitutive parameters.

Concerning the fluid phases homogenization procedure, we used the Voigt–Reuss–Hill (VRH) average (Mavko, 2009) in the gas-gas case and the formula of Brie et al. (1995) in the liquid-gas case. The Voigt–Reuss–Hill average is the arithmetic average of the Voigt upper bound and the Reuss lower bound:

$$M_{VRH} = \frac{M_V + M_R}{2} \quad (24)$$

Where

$$M_V = \sum_{i=1}^N f_i M_i \quad (25)$$

$$\frac{1}{M_R} = \sum_{i=1}^N \frac{f_i}{M_i} \quad (26)$$

the terms f_i and M_i are the volume fraction and the modulus (K or G) of the i -th component, respectively. Brie et al. (1995) suggest an empirical fluid mixing law, given by

$$K_{Brie} = (K_{liquid} - K_{gas})(1 - S_{gas})^e + K_{gas} \quad (27)$$

where K indicates the bulk modulus of the gas and liquid phases, and S represents the saturations.

The density of the porous medium is the arithmetic mean of fluid and solid phases weighted by their own volumes via the porosity, so that:

$$\rho = (1 - \varphi)\rho_s + \varphi\rho_f \quad (28)$$

After obtaining the *effective medium* by the homogenisation process of the solid and fluid phases, we are able to apply the Gassmann relations (Gassmann, 1951) that lead to the following definitions of parameters that explicitly describe the homogenised porous medium: un-compressibility modulus K_U , the Biot C modulus and the fluid storage coefficient M .

Relationships between coefficients K_U , C and M and the modulus functions of K_D , K_s , K_f and φ are given by

$$K_U = \frac{\varphi K_D + (1 - \frac{(1 + \varphi)K_D}{K_S})K_f}{\varphi(1 + \Delta)} \quad (29)$$

$$C = \frac{(1 - K_D/K_S)K_f}{\varphi(1 + \Delta)} \quad (30)$$

$$M = \frac{K_f}{\varphi(1 + \Delta)} \quad (31)$$

Where

$$\Delta = \frac{1 - \varphi K_f}{\varphi K_S} \left(1 - \frac{K_D}{(1 - \varphi)K_S}\right) \quad (32)$$

The shear modulus of the porous medium G is independent from the fluid characteristics and, therefore, equal to the shear modulus of the drained solid skeleton through the relation where only the porosity φ and the consolidation parameter c_s are present.

Biot theory provides connections between effective parameters at the mesoscale and macroscale seismic parameters obtained by seismic imaging. Biot developed dynamic equations which govern particle motions in saturated porous media and which were confirmed by many authors (Burridge and Keller, 1981; Pride et al. 1992; Pride and Berryman, 1998). Assuming a time dependency in $e^{-i\omega t}$, Pride (2005) formulated these equations, that control isotropic poroelastic response, as:

$$\nabla \cdot \vec{\tau}^D - \nabla P_c = -\omega^2(\rho\vec{u} + \rho_f\vec{w}) \quad (33)$$

$$-\nabla p_f = -\omega^2\rho_f\vec{u} - i\omega\frac{\eta}{k(\omega)}\vec{w} \quad (34)$$

$$\vec{\tau}^D = C(\nabla\vec{u} + (\nabla\vec{u})^T - \frac{2}{3}\nabla \cdot \vec{u}\mathbf{I}) \quad (35)$$

$$-P_c = K_U \nabla \cdot \vec{u} + C \nabla \cdot \vec{w} \quad (36)$$

$$-p_f = C \nabla \cdot \vec{u} + M \nabla \cdot \vec{w} \quad (37)$$

where the stress tensor is denoted by τ and the fluid pressure by P . The displacement u can be considered coinciding with the solid grains displacement u_s and w is the relative displacement between fluid and solid phases, $w = \phi(u_f - u_s)$. The terms $\vec{u}, \vec{w}, \vec{\tau}^D, P_c$ and p_f represent the average response in volume that are much larger than the grains of the material but much smaller than the wavelengths.

Equation (33) represents the total balance of forces on each rock sample. Equation (34) is itself a force balance on the fluid from a frame of grains, i. e. a generalized Darcy law. Equations (35), (36) and (37) are the constitutive equations.

To obtain velocity and attenuation parameters, one need to insert the stress/strain relation into the force balances considering a homogeneous porous continuum, as in the elastic case. Then, putting the plane-wave response into these equations, we obtain the different equations solution corresponding to different types of wave.

In particular, Biot's theory predicts three wave types: a shear wave similar to those propagating inside an elastic medium and two compressional waves, one similar to those propagating inside an elastic medium, and another, called Biot wave, slow and strongly diffusive and attenuated at low frequencies. This Biot wave behaves as either a diffusive signal or a propagative wave depending on the frequency content of the source with respect to the cut-off pulsation or characteristic frequency. The slowness of the shear wave is given by the following equation (Pride, 2005)

$$s_S^2 = \frac{\rho - \rho_f^2 / \tilde{\rho}}{G} \quad (38)$$

while slownesses of compressional waves, the P and Biot waves, are given by

$$s_P^2 = \frac{\gamma}{2} - \frac{1}{2} \sqrt{\gamma^2 - \frac{4(\rho \tilde{\rho} - \rho_f^2)}{HM - C^2}} \quad (39)$$

$$s_{Biot}^2 = \frac{\gamma}{2} + \frac{1}{2} \sqrt{\gamma^2 - \frac{4(\rho \tilde{\rho} - \rho_f^2)}{HM - C^2}} \quad (40)$$

where

$$\gamma = \frac{\rho M + \tilde{\rho} H - 2\rho_f C}{HM - C^2} \quad (41)$$

$$H = K_U + \frac{4}{3} G \quad (42)$$

From these equations we can deduce the correspondent velocity and quality factors (Pride, 2005):

$$V_{P,Biot,S} = \frac{1}{Re(s_{P,Biot,S})} \quad (43)$$

$$Q_{P,Biot,S} = \frac{1 Re(s_{P,Biot,S})}{2 Im(s_{P,Biot,S})} \quad (44)$$

The Biot slow waves velocities and quality factors are not measurable with classical seismic records, so they were not considered in our analysis.

The procedure described above allows to obtain the up-scaled macro-parameters values, which were compared with the macro-parameters obtained with seismic tomography. We defined a likely set of micro-parameters as the one for which the resulting up-scaled macro-parameters fall within the range of the observed values.

The up-scaling procedure has been implemented in a fortran 90 code.

1.3.2 Rock physics modelling: down-scaling

In order to obtain three-dimensional models of micro-parameters, starting from the velocity and attenuation ones, we could construct a complete non-linear inversion procedure. The first step consists in establishing a parameterization of the host volume, i.e. in determining a minimal set of model parameters whose values completely characterize the system. Then, we could construct a forward modelling, i.e. discovery the physical laws allowing to make predictions on the results of some observable parameters. In our case, this is represented by the rock modelling described in the previous paragraph. Lastly, we could construct the inverse modelling, i.e. a procedure that allows to obtain, for each node of the model grid, an optimized estimation of the micro-parameter value from the comparison between the observed value of the macro-parameters and the one obtained one by the above up-scaling procedure.

The cost function expression plays a key role in the inversion procedure. In fact, we have to pay attention to the fact that the four macro-parameters used in the inversion process have a

different physical nature. Because of that, we have introduced a cost function based on relative residuals of macro-parameters, in which the velocity and the attenuation factor are differently weighted:

$$F(V_l, Q_l) = \sqrt[p]{\frac{\sum_l \left[\omega_{Vl} \left(\frac{V_l^{obs} - V_l^{cal}}{V_l^{obs}} \right)^p + \omega_{Ql} \left(\frac{Q_l^{obs} - Q_l^{cal}}{Q_l^{obs}} \right)^p \right]}{\sum_l (\omega_{Vl} + \omega_{Ql})}} \quad (45)$$

Here $l=P,S$ and the ω are the weights.

In order to provide a better definition of the cost function, several tests were planned to optimize the choice of:

- The value of the p -norm, which can be 1 or 2 depending on the weight we want to give to the outliers;
- The value of the weight ω on the velocity and attenuation parameters, depending on the accuracy of the observed macro-parameter values;
- The possibility to use a combination of velocity and/or attenuation parameters, i.e. product or ratio, in the cost function, in order to improve the procedure resolution.

By taking into account the micro-parameters continuity into the realistic host medium, we can improve the cost function resolution considering in the inversion of one grid node, the information of the six neighbouring nodes. In this way, the complete cost function is defined as the sum of the cost functions in the current node plus the ones of the six neighbouring nodes, properly weighted.

Because of the not uniqueness of the inverse problem solution, a more complete description of the solution can be obtained by using a probabilistic approach (Tarantola and Valette, 1982). Assuming that the distributions of micro-parameters and related errors are Gaussian around the predicted value, we can write the probability density function (PDF) for each node $x_{i,j,k}$ of model as:

$$P(x_{i,j,k}) = \frac{1}{(2\pi)^{1/2} \sigma} k e^{-\frac{\varphi^2}{2\sigma^2}} \quad (46)$$

Here σ represents the mean deviation of the distribution, i.e. the error on the observed macro-parameters, φ is the cost function and k is a normalization factor, i.e. the sum of all the

different micro-parameters models. The posterior density function (PDF) given by the equation (?) represents a complete, probabilistic solution to the inverse problem, which includes information on uncertainty and resolution. Another advantage of the probabilistic approach is the possibility to easily introduce any a-priori information on the observed parameters or parameters distribution.

The minimum misfit point of the complete, non-linear location PDF is selected as an "optimal" micro-parameter value. The significance and uncertainty of this "optimal" micro-parameter cannot be assessed independently of the complete solution PDF. "Traditional" Gaussian or normal estimators, such as the expectation $E(\mathbf{x})$ and covariance matrix C , may be obtained from the gridded values of the normalised location PDF or from samples of this function (e.g. Tarantola and Valette, 1982). For the grid case with nodes at $x_{i,j,k}$,

$$E(\mathbf{x}) = \Delta V \sum_{i,j,k} x_{i,j,k} P(x_{i,j,k}) \quad (47)$$

Where ΔV is the volume of a grid cell. The covariance matrix is then given by:

$$C = E((\mathbf{x} - E(\mathbf{x}))(\mathbf{x} - E(\mathbf{x}))^T) \quad (48)$$

The 68% confidence ellipsoid can be obtained from the singular value decomposition (SVD) of the covariance matrix C , following Press et al. (1992). The SVD gives:

$$C = \mathbf{U}(\text{diag } w_i)\mathbf{V}^T \quad (49)$$

where $\mathbf{U} = \mathbf{V}$ are square, symmetric matrices and w_i are singular values. The columns V_i of \mathbf{V} give the principal axes of the confidence ellipsoid. The Gaussian estimators and the resulting confidence ellipsoid will be good indicators of the uncertainties in the location assuming that the complete, non-linear PDF has a single maximum and an ellipsoidal form.

Chapter 2: *Tracking TIME changes of physical properties*

2. Introduction

The characterization of the propagation medium in terms of elastic/anelastic and rock parameters and the possibility of making inferences about the presence of fluid are very important tool to track fluid migration within the host medium.

A very important application of the temporal variation tracking of seismic properties concerns the prediction of earthquakes. Several authors (Whitcomb et al., 1973; Chiarabba et al. 2009; Lucente et al., 2010) found a large precursory change in seismic body-wave velocities occurring before earthquakes. This phenomenon is well explained by considering the key role of fluid diffusion in earthquake nucleation and the consequent effects of rock dilatancy on fluid-filled, porous media (Frank et al., 1965; Nur, 1972). The authors also suggest that similar processes may be observed in the preparatory phases of future earthquakes.

Moreover, the tracking of fluid migration and its consequences on induced seismicity, play a key role in the seismic monitoring of a producing reservoir (Wang et al., 1998; Lumley, 2001; Vesnaver et al., 2003; Gunasekera et al., 2003; Gritto et al., 2014). In fact, the aim of seismic reservoir monitoring is to image fluid flow in a reservoir during its production. This is possible because, as fluid saturations and pressures in the reservoir change, the seismic elastic and anelastic response changes accordingly.

Finally, the question of whether a high level of seismic activity is a precursor to an impending eruption is very relevant for volcanic monitoring. The study of the physical properties temporal variation inside the volcano (for instance the measurement of a variable related to the state within the hydrothermal system) would help in assessing the possible size of an eruption or the occurrence of volcanic instability (Ratdomopurbo and Poupinet, 1995; Duputel et al., 2009).

Depending on the needs, “fast” methods should be adopted since they allow the monitoring of large scale medium properties for each recorded seismic event, therefore in a short time after the event. Despite the necessity of a long time-span to record a consistent data-set required to achieve a good resolution, more comprehensive methods (e.g. tomographic inversion)

allow to obtain 3D images in different time intervals of the investigated parameters. This results in a better characterization of the location, shape and magnitude of the related anomalies. The “fast” techniques provide complementary information to the results of the comprehensive methods and its advantage is that it can be quickly computed as soon as the seismogram is available (Chiarabba et al., 2009; Lucente et al. 2010; Valoroso et al., 2011). Moreover, the “fast” methods can be used as a preliminary analysis tool, in order to select the appropriate temporal windows and optimize the source-receiver geometry for each of the analysed time window for the 4D tomography.

Among the “fast” methods we analyse:

- the station residuals variation analysis, that consists in tracking the temporal variation of the time residuals of the location obtained in a 3D model. The time residuals are indicators of the temporal and spatial differences between the actual velocity model and the average one;
- the V_p/V_s ratio variation analysis, which consists in tracking the V_p/V_s ratio, a quantity that is directly correlated with the presence of fluids within the crust. The V_p/V_s ratio is tracked as a function of time for each of the station couples and through their comparison to each other, in order to identify both spatial and temporal changes of medium properties (Wadati, 1933; Kisslinger and Engdahl, 1973; Chiarabba et al., 2009b; Lucente et al. 2010; Valoroso et al., 2011; Gritto et al., 2014).

The analysis of V_p/V_s ratio temporal variation was used by Lucente et al. (2010) to reconstruct the preparatory phase of the 6 April 2009 Mw 6.3 L’Aquila earthquake, in central Italy. Approaching the earthquake, about a week before, the authors observed clear variations in the V_p/V_s ratio temporal trend. The change of the V_p/V_s ratio during the foreshock sequence suggests that seismic waves travel through a fractured medium, and that fracture field properties vary with time (Nur, 1972; Scholz et al., 1973; Aggarwal et al., 1973; Whitcomb et al., 1973). This variation is modelled through a complex sequence of dilatancy and fluid-diffusion processes affected the rock volume surrounding the nucleation area. The authors inferred that the key role played by the process of fluid diffusion in the L’Aquila earthquake nucleation may be observed in the preparatory phases of future earthquakes in Italy and elsewhere. A similar result was retrieved by Valoroso et al. (2011) analysing the seismicity at the Val d’Agri in southern Italy, and Chiarabba et al. (2009) considering the 1997 Umbria-Marche sequence in central Italy. As a consequence, the authors of these works suggested a better monitoring of temporal variation of the elastic properties in order to mitigate the seismic hazard in highly vulnerable area. In this framework, a method allowing the rapid estimation of the V_p/V_s ratio is fundamental in earthquakes prediction/prevention issue.

Among the more comprehensive methods, the most widely used is the time-lapse seismic reservoir monitoring. This method consists in the process of acquiring and analysing multiple seismic surveys, which were repeated at the same site over calendar time, in order to image the fluid-flow effects in a producing reservoir. Time-lapse seismic reservoir monitoring has advanced rapidly over the past decade and is quickly becoming a vital engineering reservoir management tool (see, e.g., Ebrom et al. 1998; Landrø et al., 1999; Johnston et al., 2000; Davis and Benson, 2001; Gunasekera et al., 2003). In fact, 4-D seismic can monitor the progress of costly injected fluid fronts (water, gas, steam, CO₂, etc.) that can save hundreds of millions of dollars in optimizing injection programs and can map reservoir compartmentalization and the fluid-flow properties of faults (Lumley, 2001). The goal of 4-D seismic data processing is to obtain excellent 3-D seismic images for each data set, and simultaneously optimize time-lapse repeatability in regions of no subsurface change. In order to minimize non-reservoir 4-D image differences, equalize spectral bandwidth and phase, amplitude gain variations, differential statics, and event positioning, a “cross-equalization stage” is required (Altan, 1997; Eastwood et al., 1998; Rickett and Lumley, 1998).

Moreover, the 4D seismic tomography can be applied in a seismogenic area where a permanent network of sensors is available and a consistent data-set of seismic events is then recorded. This technique consists in applying the three-dimensional tomography in different time-windows. By analysing the tomographic images obtained for each time-window, after having ensured the same resolution for each of them, it is possible to map out the spatial and temporal changes in elastic/anelastic seismic parameters. Then, these changes can be correlated to the fluid saturations changes in the propagation medium to infer information about earthquake nucleation processes.

A very explicative example of this technique is the application performed by Chiarabba et al. (2009) at the 1997 Umbria-Marche sequence in central Italy. The authors showed the observations of rock fracturing and fluid overpressure propagation along a fault system by using time repeated velocity tomography. In particular, they computed the variations of V_p/V_s anomalies (4D variations) that accompanied earthquake migration and preceded large aftershocks. The authors inferred that V_p/V_s increase observed before the mid-October earthquakes was related to a pore-pressure increase on fluid-filled cracks in the volume around the fault. Thus, the 4D seismic tomography represents a very useful tool for track pore-pressure and elastic properties variation around the nucleation area.

The first paragraph regards the “fast” tracking methods, the station residual variation and the V_p/V_s ratio tracking. The second paragraph contains details about the time-lapse tomography. In particular, in the second paragraph is described a new automatic procedure of cross-equalization for passive seismic data-set.

2.1 FAST tracking methods

2.1.1 Station residuals variation tracking

This method is used to evaluate the variations of the 3D velocity model, and hence of the sub-soil structure, from the temporal variation of the arrival time residuals of the first P and S-waves. If we consider the 3D velocity model for an area calculated by inverting a data-set of events which occurred over a long period of time, the obtained model averages possible model variations over time in the analysed period. The arrival time residuals, separately evaluated for the P and S phases, in a given time interval, are indicators of the temporal and spatial differences between the actual velocity model and the average one. In particular, we can consider the change with time of residuals at the same station for different events that occurred in the given time lapse (Figure 3, left panel), or the residual time changes of closely located events at different stations (Figure 3, right panel). In the first case, we will obtain information about changes of medium properties located near the surface and beneath the selected station. In the second case, we can infer possible time changes of medium properties in the volume of events occurrence. An important aim of this residual analysis could be the selection the appropriate temporal windows for the 4D tomography. The criterion underlying this choice is to maximize the spatial resolution and its homogeneity in all the different studied time intervals, optimizing the source-receiver geometry.

2.1.2 V_p/V_s ratio variation tracking

The V_p/V_s ratio is a quantity directly correlated to the presence of fluids within the crust. The analysis of the temporal variation of the V_p/V_s ratio is a technique that aims to image the large-scale medium properties. This technique provides complementary information to the results provided by a tomographic inversion procedure, and its advantage is that it can be quickly computed as soon as the seismogram is available.

The V_p/V_s ratio value can be computed from the time difference between the S- and P-wave arrival times at a given station (respectively indicated by t_p and t_s), divided by the P-wave travel-time from the hypocentre to the station (Lucente et al., 2010; Wadati, 1933; Kisslinger and Engdahl, 1973; Chiarabba et al., 2009b; Gritto et al., 2014).

$$t_s - t_p = \frac{R}{V_p} \left(\frac{V_p}{V_s} - 1 \right) = t t_p \left(\frac{V_p}{V_s} - 1 \right) \quad (50)$$

$$\frac{t_s - t_p}{tt_p} = \left(\frac{V_p}{V_s} - 1 \right) \quad (51)$$

Here R is the hypocentral distance and tt_p is the P wave travel-time. The above relation holds for a uniform V_p/V_s ratio along the travel path (Scholz et al., 1973; Whitcomb et al., 1973).

As in the previous analysis, we can consider the change of the V_p/V_s ratio at the same station for different events that occurred in the given time lapse, in order to image the changes in the crustal volume beneath the considered station (Figure 3, left panel); or we can compute the V_p/V_s ratio for several events that occurred in the same source region, and have been recorded at different pairs of nearby stations, in order to reveal possible changes in crustal volume next to the source region (Figure 3, right panel). The basic idea is to analyse the graphs of the V_p/V_s ratio is a function of time for each couple of the station, and to identify both spatial and temporal changes by comparing them to each other.

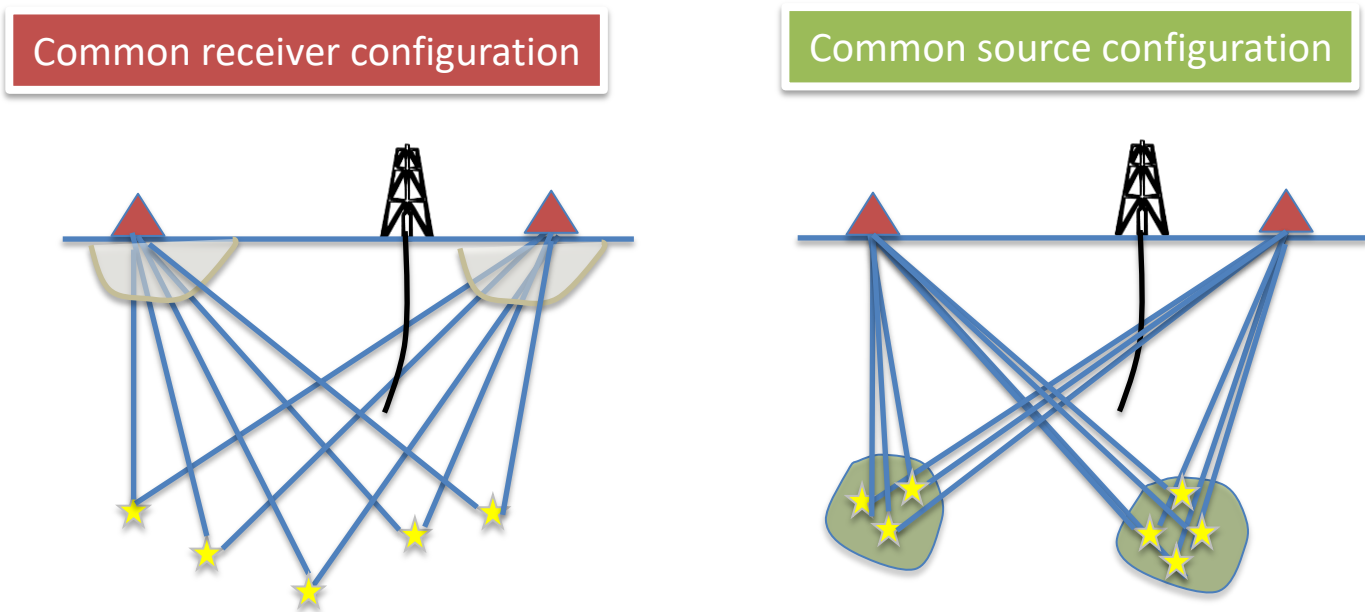


Figure 3. Schematic representation of the rays path for a given sources-stations geometry. The yellow stars represent the seismic sources, the red triangles the receivers and the blue lines the ray-paths. The calculated value of residual or V_p/V_s ratio is associated at the area common of all considered source-receiver ray-paths. In the left panel the common area of all the rays is the region beneath the stations; in the right panel the common area of all the rays is the sources region.

2.2 COMPREHENSIVE tracking methods: Time-lapse tomography

The goal of the 4-D seismic data processing is to obtain 3-D high-resolution seismic images for each data-set, while minimizing non-reservoir 4-D image differences (Lumley et al. 1995; Lumley, 2001; Vesnaver et al., 2003). These custom processing tools have generally come to be known in the industry as “cross equalization”. The procedure consists in equalizing spectral bandwidth and phase, amplitude gain variation, different statics, and in the event positioning of co-register repeated survey data in order to optimize 4D seismic difference anomalies.

We are interested in reconstructing the fluid flow in the medium through the application of time-lapse tomography to a continuous data-set of seismic events recorded with the same permanent acquisition network. This implies that the parameter to be equalized in the first step of time-lapse tomography is only the geometry of the sources, which are not fixed or controlled when working in passive seismic. The equalization is based on the choices of time windows (epochs) dividing the data-set, ensuring to have the same high-resolution of the tomographic images at all epochs.

In the application realized so far, the choice of time-windows has either been bound to a specific physical event to analyse, i.e. an earthquake in a seismic area, fluid injection/extraction in a reservoir area or eruption events in a volcanic area (CO₂ reservoir: Saito et al., 2006; Volcanic area: Patane et al. 2006; Seismogenic area: Chiarabba et al. 2009; Valoroso et al. 2011), or has been done by considering separate time periods (Gunasekera et al. 2003). In the first case, in particular, the entire time period to analyse is not too long, i.e. at most about one year, and the 4D tomography is performed on a few time-epochs (two or three). It is clear that in these cases a complex procedure is not required to select the optimal time-windows. As an example, in the work of Chiarabba et al. (2009), the authors explained that the choice of epochs was done by subdividing the entire data-set in fixed time intervals, and then by comparing the resolution in the different obtained epochs, in order to ensure a consistent model resolution.

In this framework, the last part of our research project has focused on the development of a new equalization procedure for the massive seismic data-set recorded on a long-time period (of the order of several years), on which we are still working on. The novelty of this procedure lies not only in its ability to optimize the choice of time-windows (that may have different durations in passive seismic) in the case of massive data-sets, but also in a complete handling

of the issue associated to the seismic tomography, which includes the choice of inversion parameters, the choice of the optimal model parameterization, the analysis of the model resolution, etc. Moreover, a *multi-scale* procedure is included in the method.

It is clear that this complex procedure should be included in a code system allowing to automatically optimize the entire process. We started to develop this code from the existing tools of tomographic inversion and resolution analysis that are described in the first chapter of this thesis. Below, in table 1, we report the operating scheme of the complete procedure of “*cross-equalization of the passive seismicity catalogue*”. The procedure is divided in four parts:

1. Parameter setting and definition of the reference model;
2. Setting of the first epoch time-length;
3. Estimation of the time-windows length;
4. Comparison between tomographic images.

The first part of the equalization procedure consists in a preliminary 3D analysis, which aims to achieve a reference 3D velocity model for the entire data-set and the related resolution. The resolution can be assessed from the ray coverage, the derivative weight sum (DWS) (Toomey and Foulger, 1989) or the diagonal element of the resolution matrix or of the spread function (S_j) (Micheline and McEvilly, 1991) (for further details see par. 1.1.1.2).

Since the inversion method is linearized, there is the need for an initial velocity model. This initial velocity model must be the same for all the inversions in the different epochs, in order to minimize the contaminant effect of the 4D variation. The choice of the initial velocity model can be done by using a-priori or complementary information (i.e. geological prospection, well logs, etc.). An interesting choice could be the use of the 3D reference model as the initial model for the inversion in each epoch. In this way, the resulting 3D images will directly show the variation with respect to the reference model.

An important step of this part is the setting, considering the entire data-set, of optimal model parameterization, and of the optimal inversion parameters, i.e. the damping factor and iper-parameters. The first step is achieved by testing different model parameterizations, by halving the step size every time, and by stopping the iterative procedure in accordance with the Akaike criterion (Akaike, 1974), i.e. when the best compromise between the inversion rms (root mean square of time residuals) and the complexity of the model is reached. The second step is achieved by performing sensitivity tests with different values of damping and iper-parameters, and by choosing the combination for which a small variance in the data corresponds to a small variance in the model. This step is performed for every selected recursive parameterization.

The second part of the procedure regards the setting of the time-length of the first epoch. First, we fix three different time lengths (e.g. chosen by using a priori information), then we invert the correspondent three data-sets by using the inversion parameter set in the previous part, thus obtaining the 3D models and calculating the related resolution. The optimal time length is the minimal one for which the area that we want to investigate falls inside the well-resolved one.

This result is crucial, since it represents the benchmark for the resolution analysis in the individual epochs.

The third part regards the adaptive selection process of the temporal duration of each epoch. It consists in selecting specific time-windows and using the data-set recorded within this time interval to achieve a 3D tomography. The solution is evaluated and then compared with the one obtained in the first epoch with the use of the *semblance* function as a measure of similarity of resolved areas (Fig. 4). This comparison is performed for each recursive parameterization, and the semblance function has to be sufficient at least for the wider parameterization (Fig. 5). If the resolution is too low with respect to the benchmark one, the length of the time-window has to be increased so as to include more data. In order to have a consistent model resolution between the different epochs, the epochs may have different durations.

Once a 3D well-resolved model for each epoch has been obtained, the last part consists in the comparison of these models. According to what one wants to investigate, the comparison may be made between each epoch and the first one, or between each epoch and the reference model obtained with the use of the whole data-set, or even between the different epochs. The variation found in the obtained images can thus be interpreted in terms of fluid motion in preparation, or as a result of an investigated physical phenomenon (i.e. a seismic event, fluid injection/extraction, hydrothermal depletion, etc.).

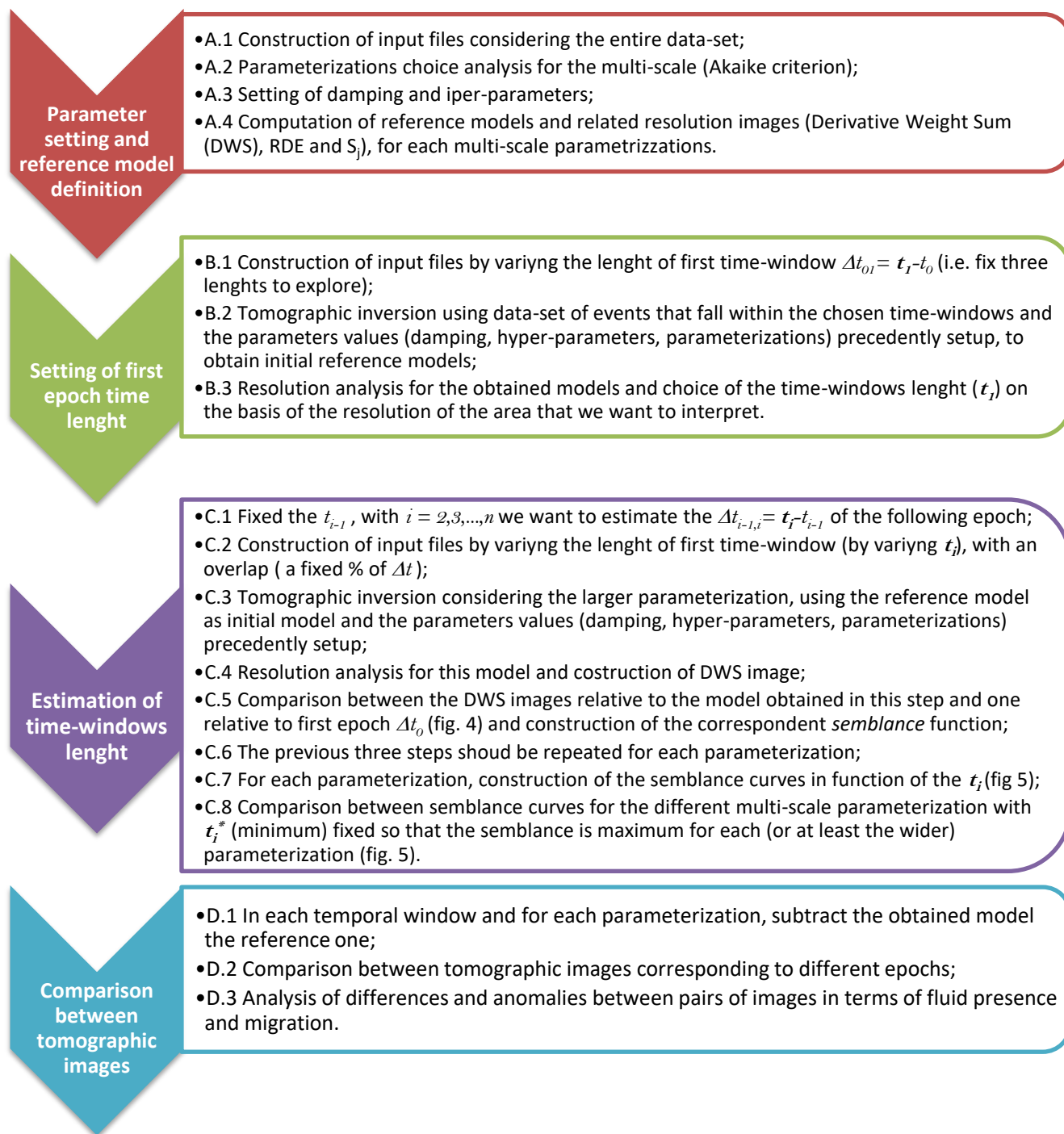


Table 1. Overview for the operation scheme of the code for cross-equalization of passive seismicity catalogue.

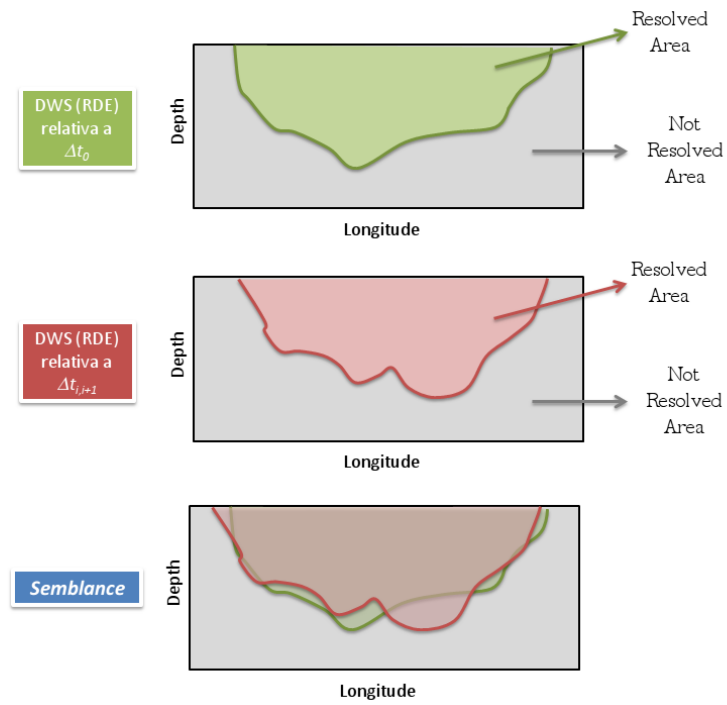


Figure 4. Assessment of high resolution area in 4D tomography. Comparison between the DWS images of different epochs. The last bottom panel shows the construction of semblance function.

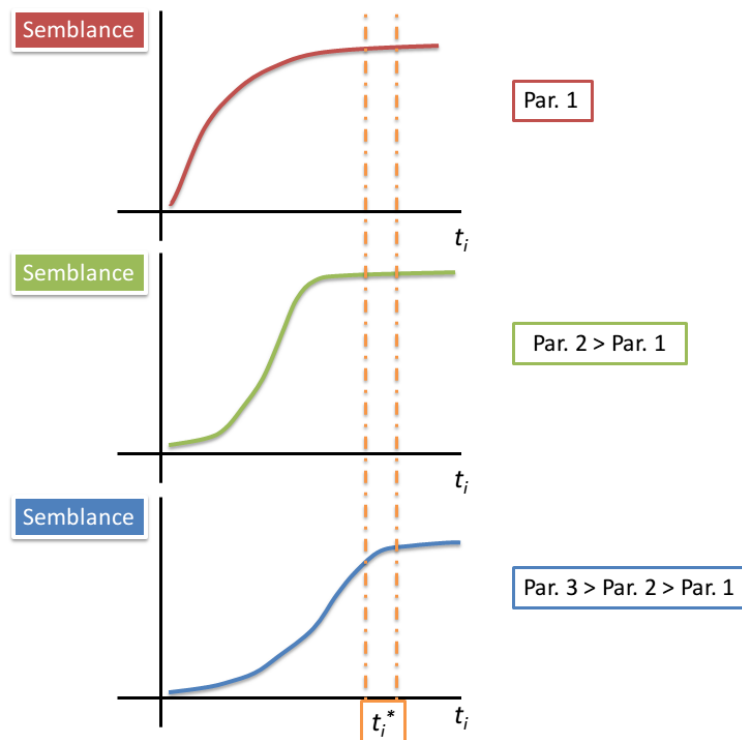


Figure 5. Curves of semblance values in function of length of current epoch time-windows for the different multi-scale parameterizations.

Chapter 3: *Tracking changes of SEISMICITY distribution*

3 Introduction

It is widely recognized that pore-fluid flow may play a dominant role in triggering seismicity (Nur and Booker, 1972). Diffusive processes of pore pressure relaxation in fractured and saturated rocks have been proposed to explain both earthquakes (Noir et al., 1997; Bosl and Nur, 2002) and induced seismicity (Talwani and Acree, 1985). Furthermore, the injection or production of fluids can induce micro-seismic events in hydrocarbon and geothermal reservoirs.

According to Nur and Booker (1972), considering the behaviour of aftershocks, large shallow earthquakes can induce changes in the fluid pore pressure causing a slowly decrease of the rock strength and, therefore, an attractive mechanism for aftershocks. Hainzl (2004) analyses the earthquake swarms as a result of an intrusion of fluids into the seismogenic zone, which reduces the resistance of faults (Kisslinger, 1975; Noir et al., 1997) and causes seismicity patterns which significantly differ from aftershock sequences.

Because of this relationship between fluid-flow and seismicity patterns, many authors (Nur and Booker, 1972; Hainzl, 2004; Antonioli et al., 2005; Hainzl and Ogata, 2005) test the hypothesis that the space distribution and temporal evolution of seismicity can be used to analyse the presence and diffusion of a pore-pressure perturbation in a poro-elastic fluid saturated medium.

Moreover, from the point of view of monitoring, the use of information about the source locations, timing, and mechanisms of the induced seismic events is crucial to make inferences about the structure of a reservoir or the changes that are associated with injections during the production from the reservoir (Grasso and Wittlinger, 1990; Aki et al., 2005; Maxwell et al., 2010).

Another important issue concerning the spatiotemporal distribution of seismicity lies into the possibility to identify the geometry and kinematics of the activated fault segments during a seismic sequence (De Luca et al., 2000; Boncio et al., 2004; Chiaraluce et al., 2011).

It is clear that an accurate knowledge of the seismicity pattern is crucial in these analyses in terms of space and time location. In the following paragraph, we present a high accurate non-linear, global-search, probabilistic double-difference earthquake location method,

implemented in the NLDiffLoc (Non Linear Differential Location) code. The location method uses P- and S-wave differential arrival-time data, and related uncertainties, to determine refined location solutions in complex 3D media. Moreover, we report the results of several synthetic tests, which have been carried out in order to evaluate the performance of the method by varying the seismicity distribution, the velocity model and the accuracy of the data-set of arrival times.

3.1 3D double-difference earthquake locations

The knowledge of the spatial distribution of micro-seismicity allows the identification and geometrical characterization of active fault structures (e.g., Got et al. 1994; Waldhauser & Schaff 2008), the study of the regional stress field (e.g., De Matteis et al. 2012), the characterization of the small-scale variability of faulting style, stress and strength (e.g., Hardebeck 2006; Stabile et al. 2012), the evaluation of the source parameter scaling and radiation efficiency (e.g., Zollo et al. 2014), and the assessment of the seismic hazard (e.g., Emolo et al. 2011) in active seismic regions.

The uncertainty on seismicity location parameters is strongly influenced by the network geometry, the knowledge of the crustal structures, and the number and quality of phase readings (Pavlis 1986; Gomberg et al. 1990). On the other hand, the effects due to the inaccuracy of the crustal velocity model can be minimized using relative location methods (Poupinet et al. 1984; Got et al. 1994). When the hypocentral distance between two earthquakes is, in fact, small if compared to the event-station distance and to the scale length of velocity heterogeneity, the ray paths between the source region and a common station are similar. Then, when ray geometry is favourable, the travel times difference for two events observed at one station can be attributed to the spatial offset between the events, which can be estimated with high accuracy (Got et al. 1994; Waldhauser & Ellsworth 2000).

The double-difference, relative location method has been widely used to determine fine-scale fault geometry and produces high precision earthquake locations with linearized inversion in the assumption of a one-dimensional (1D) seismic wave propagation model (Got et al. 1994; Hauksson & Shearer, 2005; Valoroso et al. 2013).

However, it has been demonstrated that the use of an incorrect velocity model can produce artefacts in the location of hypocentres even applying the double-difference method (Michelini & Lomax 2004). The use of a simple 1D velocity model may be not appropriate in

crustal volumes with strong lateral variation in velocity and irregular topographic surface and a three-dimensional (3D) velocity model may be needed to get a proper account of this crustal heterogeneity.

3D crustal seismic velocity models are increasingly available from seismic travel-time inversion and eventually from geologic and geophysical interpretations. Probabilistic, absolute earthquake location using non-linear, global-search methods allows the use of complex 3D models and produces comprehensive uncertainty and resolution assessment (Lomax et al. 2000; Lomax et al. 2009). On the other hand, the use of differential travel-times with 3D velocity models is restricted to linearized, double-difference tomography (Thurber et al. 2004; Monteiller et al. 2005; Bannister et al. 2011); in this case the relative event locations can be determined jointly with the 3D velocity model.

In the following paragraph, we present a non-linear, global-search, probabilistic double-difference earthquake location method, implemented in the NLDiffLoc (Non Linear Differential Location) code, which uses both P- and S-wave differential arrival-time data and related uncertainties to determine refined location solutions in complex 3D media. This analysis has been presented in the paper of De Landro et al. (2015).

3.1.1 Relative location method

For absolute, non-linear, global-search location in 3D models we use the methodology proposed by Lomax *et al.* (2000), implemented in the NonLinLoc (Non Linear Location. Lomax, 2005; <http://www.alomax.net/nlloc>) software, where the complete probabilistic solution of the earthquake location problem is represented by a *posterior* probability density function (PDF).

In order to perform double-difference (dd) earthquake locations, we propose a methodology that optimizes the relative spatial x , y , z , and t (origin time) coordinates for a set of hypocentres according to a given a set of differential phase arrival times measured at each station for multiple hypocentres. The method is an “annealing Metropolis” algorithm search (Mosegaard & Tarantola 1995; Lomax *et al.* 2000; Lomax *et al.* 2009). It has a temperature parameter which allows to search using a large step-size in x,y,z,t for event perturbation initially, with a “cooling”, but not “freezing” to an “adaptive”, nearly constant step size for later sampling. Thus the later sampling becomes Metropolis sampling to define the pdf for each hypocentre in x,y,z,t . This Metropolis sampling uses an adaptive step size for each event which is slowly increased when the acceptance rate for new, perturbed event’s hypocentres is high (e.g. $> 1/4$) and decreased more rapidly if the acceptance rate is low (e.g. $< 1/4$). The method is

presumably much faster than a pure Monte-Carlo approach and likely faster, simpler and more thorough than a cascading grid-search.

An important reason for using a non-linear, directed, Metropolis-type stochastic search instead of a linearized approach, in addition to the simple use of 3D models (3D travel-time fields) with arbitrary complexity and parameterization, is the chance to explore complicated cost functions with multiple minima, curved, irregular and non-parabolic valleys in a better way. The extreme high-dimensionality of the multi-event inverse problem (“curse of dimensionality”) does make this extremely difficult whatever methods are used (including and sometimes especially linearized methods). The disadvantage of this method, compared with a linearized one is that the computation time is certainly much longer and the maximum number of differential times and events that can be processed is much less.

In the exploration space of model parameters, the algorithm seeks the parameter solution that maximizes the likelihood function (based upon the misfit between measured and calculated differential phase arrival times) while perturbing the hypocentre coordinates. In particular, the misfit and the solution likelihood are determined by evaluating the dd eq. (4) proposed by Waldhauser & Ellsworth (2000).

The equation describing the likelihood for a set of arrival-time difference measures, which concerns an event i with coordinates x, y, z , and origin time t_0 is:

$$L_i(x, y, z, t) = \exp \left\{ -\frac{1}{2} \sum_k \left[w_k^2 \frac{[(t_k^i - t_k^j)^{obs} - (t_k^i - t_k^j)^{cal}]^2}{\sigma^2 T^2} \right] \right\} \quad (52)$$

where $(...)^{obs}$ is the difference between the arrival-times of an event i and of another event j at the same station k , $(...)^{cal}$ is the calculated arrival-time difference of these two events i and j at the station k , σ is the uncertainty for a differential time measure, and T is the current Metropolis (simulated annealing) “temperature” parameter ($T \geq 1.0$) (Lomax *et al.* 2000).

During the application of the Metropolis random walk, one of the hypocentres, i , whose current likelihood is $L_i^{current}$ (Equation 1), is perturbed in x, y, z , and t . Next, the likelihood for the perturbed hypocentre i , $L_i^{perturbed}$, is evaluated to check if the perturbation improves the fit to the data, in the sense of the Metropolis rule:

- always accept the perturbed solution if $L_i^{perturbed}$ has a higher likelihood than $L_i^{current}$;

- otherwise, accept it with probability $L_i^{perturbed}/L_i^{current}$ (see Mosegaard & Tarantola 1995).

Note that this application of the Metropolis rule acts on the partial likelihood L_i for the event i , and not on the total likelihood L for all the hypocentres and over arrival-time difference measures.

The maximum likelihood point of the complete, non-linear location PDF is selected as an "optimal" hypocentre. The significance and uncertainty of this maximum likelihood hypocentre cannot be assessed independently of the complete solution PDF. Indeed, the Gaussian or normal estimators, such as the expectation $E(x)$ and covariance matrix C may be obtained from the gridded values of the normalised location PDF or from samples of this function (e.g. Tarantola and Valette, 1982; Sen and Stoffa, 1995) in the same way as in NonLinLoc (Lomax *et al.* 2000).

We made several synthetic tests in order to show how the two methods (absolute and dd) works depending on the choice of the velocity model, of the maximum possible inter-event distance and on the accuracy of the arrival times data-set.

3.1.2 Synthetic tests

In order to evaluate the performance of the method, we performed synthetic tests with a regular distribution of 112 events, which covers the same occurrence area as in real events of Irpinia micro-seismicity (red stars in Fig. 6) and has depths of 10 km, and the configuration of ISNet stations. For these events, we calculated the theoretical arrival times (Time2Eq, NLLoc package) in the 3D velocity model (Amoroso *et al.* 2014), assuming that all the stations record the P phase and half the S phase. Through this procedure we have obtained a data-set consisting of 2912 P phases and 1456 S phases.

Then, this events distribution has been located:

- with the 3D velocity model, considering maximum distance of 5 and 10 km to select the events couple to calculate the differential times, to analyse the influence of the inter-events connections on the location results (Fig. 6-7),
- with the 1D velocity model, to analyse the influence of the uncertainty in the velocity model on the absolute and relative location results (Fig. 8),
- with the 3D velocity model and arrival times with an added error, to analyse the influence of the arrival-time errors on the relative location results (Fig. 9).

From the results of the first test it is clear that the number of connections, and therefore the number of differential data, for single event is crucial. In the case of 10 km maximum distance

the locations are improved in terms of distance from the true position and of location errors that decrease on an average of about 100 m. Considering a 5 km maximum distance, every event has a maximum of 8 connections and at least one single connection (Fig. 7a). With this condition the obtained locations have mean distance from the true position of about 200 m in plane and 200 m in depth (Fig. 6c, blue). Considering a 10 km maximum distance, every event has at least 7 connections and a maximum of 16 connections (Fig. 7b). With this condition the obtained localizations are significantly improved, in fact, the mean distance is about 30 m in plane and 25 m in depth (Fig 6c, green). Thus the minimum number of necessary connections to constrain the position of a single event is about 10, which is equal to the number of connections of the central events of finer grid. In the case of real locations, Fig. 7c, for the catalogue data-set with the use of the sections every event has an average of 40 connections, while for the refined data-set, since the maximum distance is 5 km, every event has an average of 15 connections (see Fig 12b).

For the test with the 1D velocity model, the synthetic arrival times were inverted with the 1D velocity model in order to calculate the initial absolute locations with NLLoc. For the relative location we built the differentials arrival times by considering every possible combination of events with a maximum distance of 5 and 10 km, and then we located by considering the 1D velocity model (Matrullo et al, 2013). The results of this test, underlines the potential of the use of double difference if you locate by using an oversimplified velocity model compared to the complexity of the survey area. Both the seismicity distribution and the histograms show how the double-differences locations are much closer to the true position of events. Indeed, the distance decreases on average of 1.5 km both in plane and in depth, the RMS is reduced of 0.05 s on average and also the location errors decrease of about 250 m on average. In any case, even considering a double-differences technique, the use of a 1D model can however lead to errors in location of even more than 1 km (Michelini & Lomax, 2004). In particular those events in NE have a location that is far from the real one, because in this area the 3D velocity model has a lateral anomaly that the 1D model cannot obviously take into account.

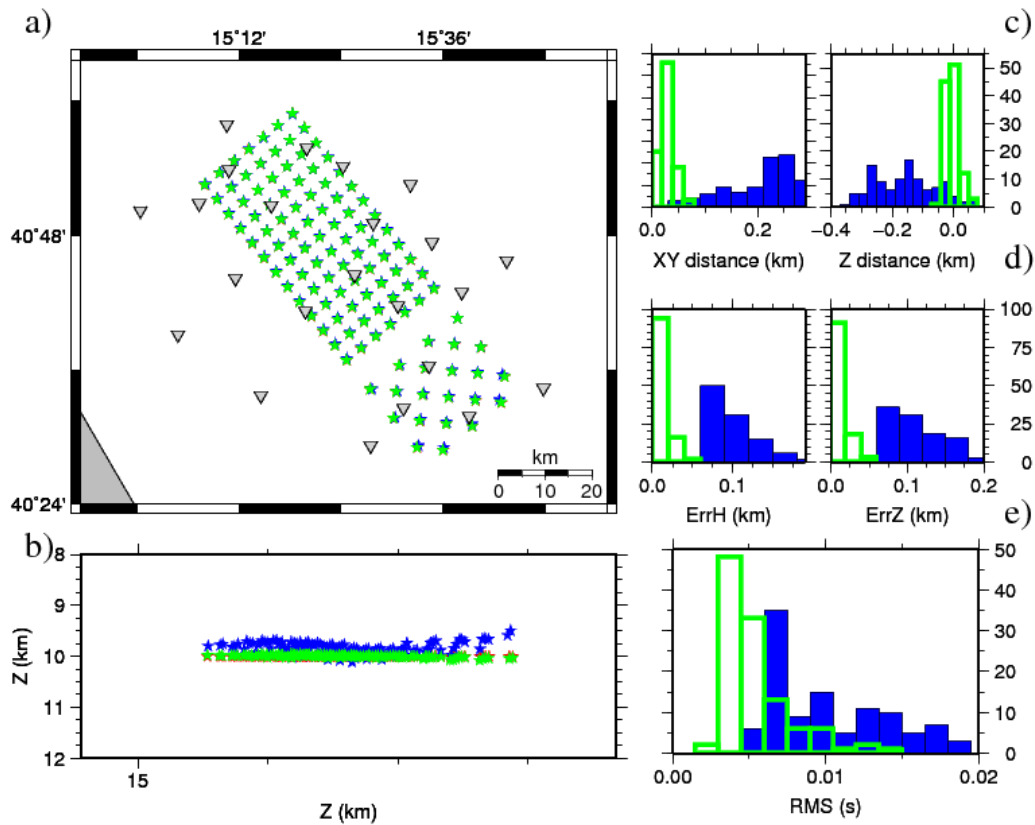


Figure 6. Test with the 3D velocity model: max. dist. 5 vs 10 km. Comparison between the *dd* location results of the synthetic events with the 3D velocity model considering a maximum distance of 5 km (blue) and 10 km (green) to calculate the differential times. Red stars indicate the reference positions of the events. Grey triangles are the ISNet seismic stations. a) Seismicity distribution in plane. (b) East-West vertical section of the seismicity. c) Distance in plane between the calculated and the true position (left) and distance between the calculated and the true depth of the events (right). d) Horizontal (left) and vertical (right) locations errors. e) RMS distribution.

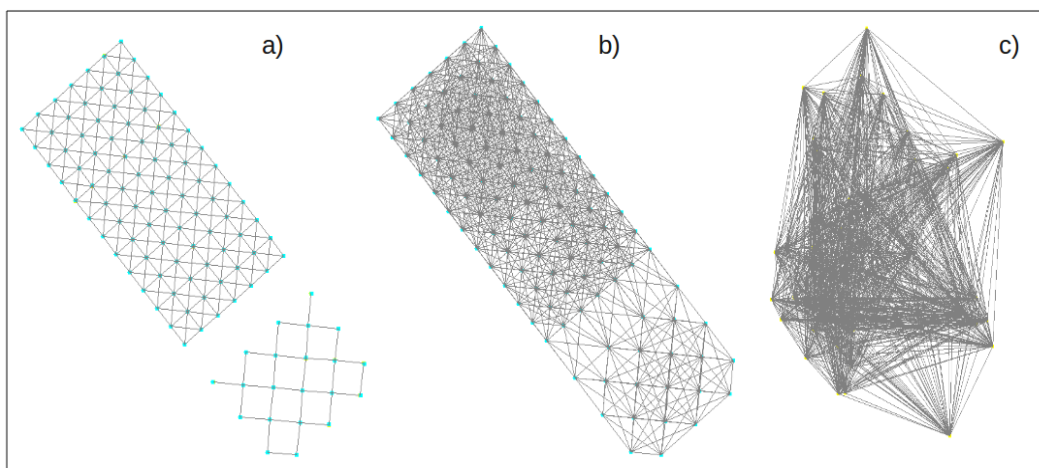


Figure 7. Plot of events inter-connection. a) Connection between events considering a 5 km maximum distance. b) Connection between events considering a 10 km maximum distance. c) Case of real locations, for the catalogue data-set with the use of sections every event has an average of 40 connections, while for the refined data-set, since the maximum distance is 5 km, every event has an average of 15 connections (see Fig. 12-b).

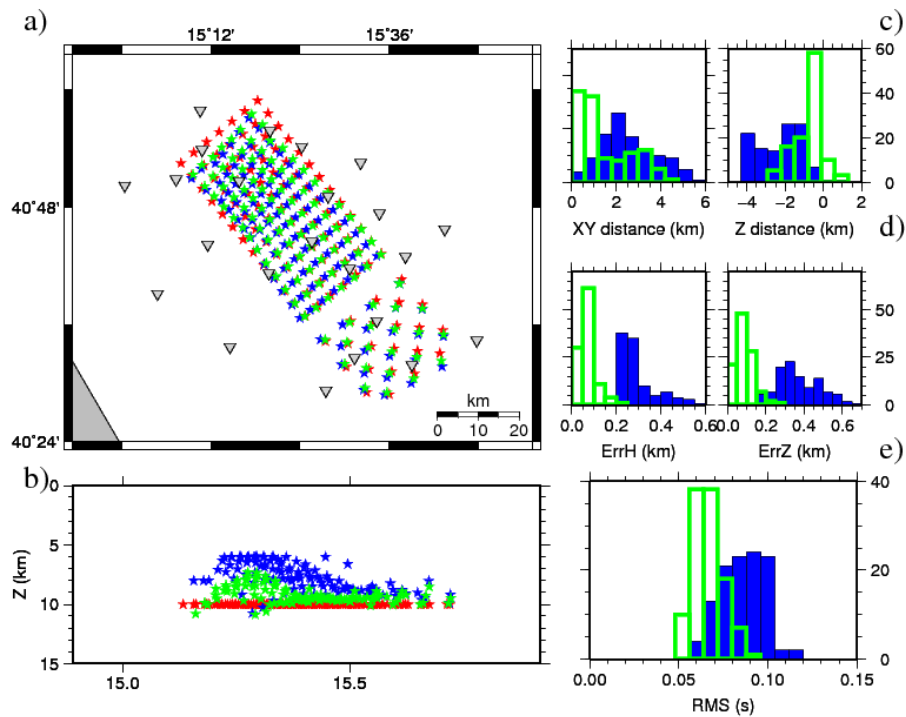


Figure 8. Test with the 1D velocity model: absolute vs. relative locations. a) Comparison between the absolute initial location (blue) and the double-difference final location of the synthetic events with the 1D velocity model. Red star indicate the events reference positions. Grey triangles are the ISNet seismic stations. a) Seismicity distribution in plane. (b) East-West vertical section of the seismicity. c) Distance in plane between the calculated and the true position. d) Distance between the calculated and the true depth of the events. e) RMS distribution.

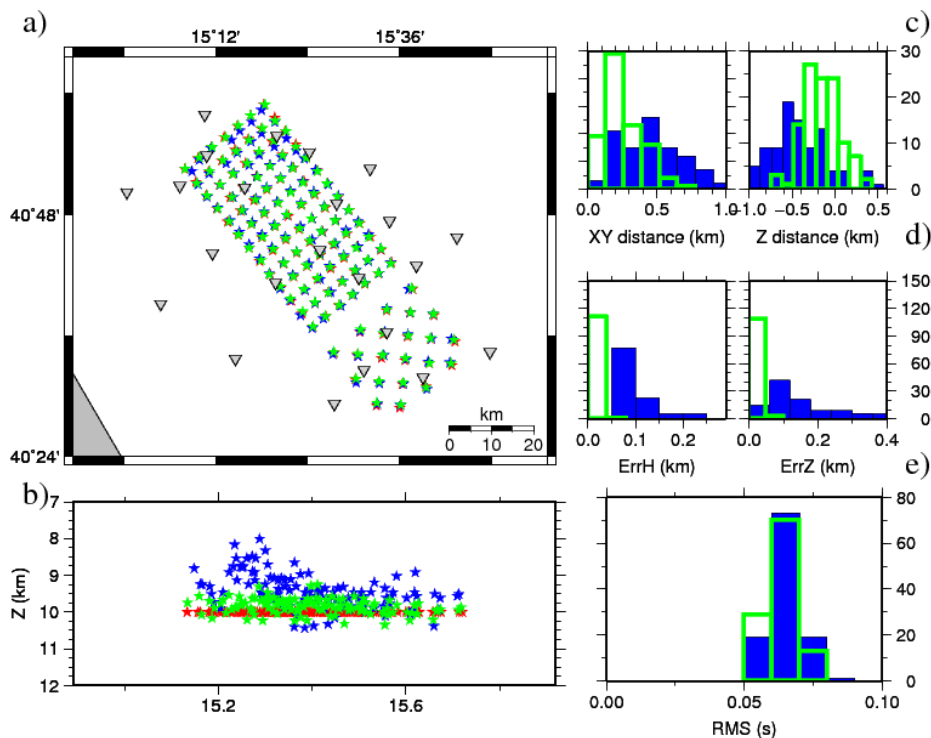


Figure 9. Test with 3D velocity model and data with errors. a) Comparison between the absolute initial location (blue) and the double-difference final location (green) of the synthetic events with the 3D velocity model. Red stars indicate reference positions of the events. Grey triangles are the ISNet seismic stations and red stars are the reference positions of the events. a) Seismicity distribution in plane. (b) East-West vertical section of the seismicity. c) Distance in plane between the calculated and the true position. d) Distance between the calculated and the true depth of the events. e) RMS distribution.

In order to analyse the code performances by considering a 3D velocity model and a data-set with an errors distribution, we performed a test whose results are showed in Fig. 9. The errors on arrival times were generated according to the distribution of the observed arrival times errors, i. e. a Gaussian distribution with a mean of 0 and a standard deviation of 0.08 for the P-phase and 0.12 for the S-phase. These errors were randomly added to the synthetic arrival times and, then inverted to calculate the initial absolute locations with NLLoc. For the relative location we built the differential arrival times considering every possible combination of events with a maximum distance of 10 km. Considering that from the arrival times without errors an average distance of about 30 meters from the reference position was obtained, we can state that the error on the data, with a similar distribution to the real one, influence the location with an error of the order of a few hundreds of meters. In this case too, as in the previous test, the double-differences location is able to improve the results in terms of both distances with respect to the reference position, which decrease of about 500m on average, and of localization errors, which decrease of about 100-150 m on average.

In Fig. 10 we show the results of a test that was performed to study the influence of the event selection criterion for the real catalogue data-sets on location accuracy. In particular, the Fig. 10 represents the double-difference location of the catalogue data-set with the 3D velocity model, considering all the events with a 5 km max distance (turquoise dots) and the subdivision in sections of $10 \times 10 \times 30 \text{ km}^2$ (grey dots). The Fig. 10 is useful to show how the use of cubic sections, initially introduced to locate a large number of events with the code NLDiffLoc and, now optimized, has proved to be necessary to obtain accurate localization for the catalogue data-set. It is clear that, if we use all the events by fixing a maximum distance, there are several locations that are placed outside of the seismicity distribution and the corresponding errors are very high (greater than 3-4 km, Fig. 10). This result indicates that with this configuration, the code fails to converge to a good solution, and in consequence the probability distributions are very irregular too (some localizations are "ABORTED") despite the fact that for each event there is a large number of connections (see Fig. 12-b). With the introduction of the 10 km sections, we have the possibility to obtain more stable solutions and lower localization error, reaching a maximum of 500 m, even though there is an increase of the RMS values. We emphasize that within the sections all the possible connections between events are considered thus ensuring a large data-set to be made for each location (see Fig. 7c). In addition, the sections are overlapped to ensure that an event placed on the edge of a section is in the centre of the next, and so that it could have a sufficient number of connections.

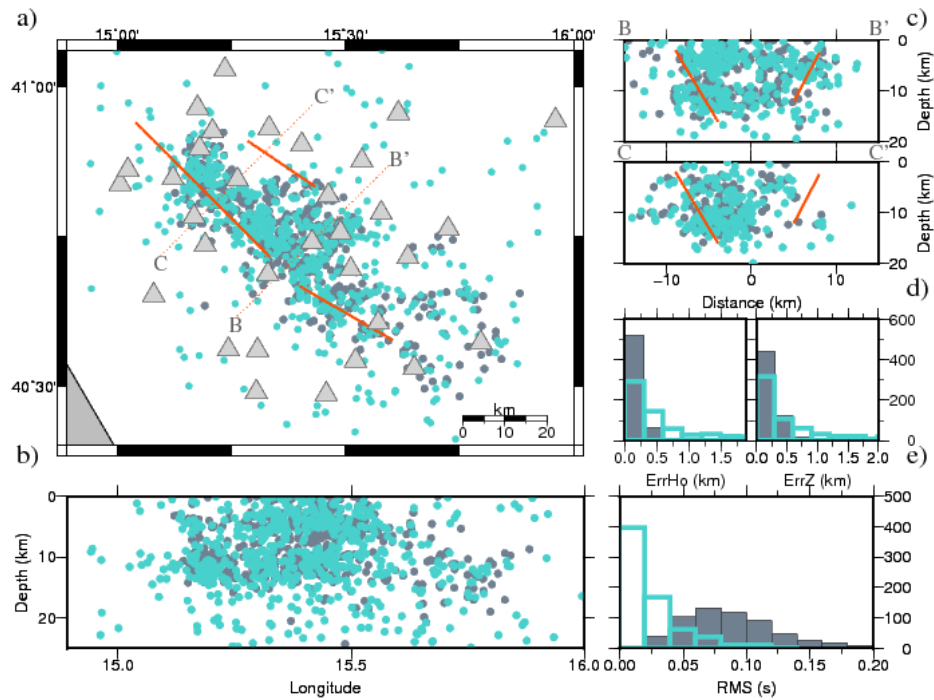


Figure 10. Test on the events selection criterion for the real catalogue data-sets. Double-difference location of the catalogue data-set with the 3D velocity model considering all the events with a 5 km max distance (turquoise dots) and the subdivision in section of $10 \times 10 \times 30 \text{ km}^2$ (grey dots). Grey triangles are the seismic stations. a) Seismicity distribution in plane. b) East-West vertical section of the seismicity. c) Anti-appenninic section according to the dotted red lines in a). d) Horizontal (right) and vertical (left) locations error distribution. e) RMS distribution.

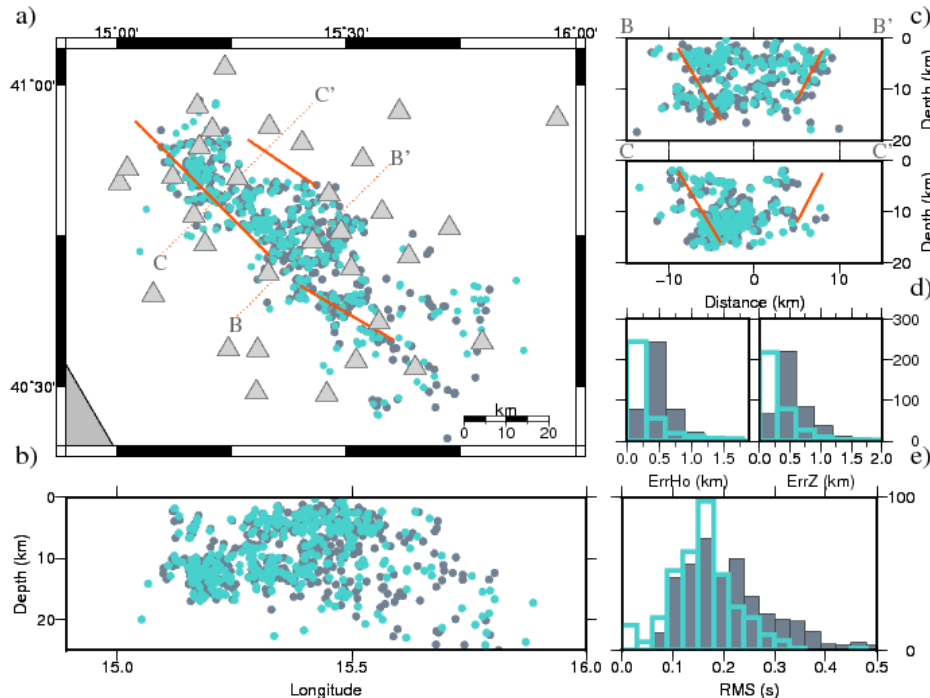


Figure 11. Test on the events selection criterion for the real re-fined data-sets. Double-difference location of the re-fined re-picking data-set with the 3D velocity model considering all the events with a 5 km max distance (turquoise dots) and subdivision in section of $10 \times 10 \times 30 \text{ km}^2$ (grey dots). Grey triangles are the seismic stations. a) Seismicity distribution in plane. b) East-West vertical section of the seismicity. c) Anti-appenninic section according to the dotted red lines in a). d) Horizontal (right) and vertical (left) locations error distribution. e) RMS distribution.

The same test is performed using the re-fined data-set. The results are shown in Fig. 11. In particular, the figure shows the double-difference location of the refined re-picking data-set with the 3D velocity model considering all the events with a 5 km max distance (turquoise dots) and subdivision in sections of $10 \times 10 \times 30 \text{ km}^2$ (grey dots). In the case of the refined re-picking data-set, the localization obtained by considering all the events with a 5 km maximum distance (turquoise dot in Fig. 11) turns out to be similar to the one obtained through the sections (grey dot in Fig. 11), if not better, in terms of seismicity distribution, locations errors and RMS.

The two distributions are very similar, the one without the sections appears more clustered and only a few events are localized outside the pattern. Such events, not well localized, are those with few connections (see Fig. 12a).

The arrival times of the refined re-picking data-set, despite being absolute times, contain the information on the cross-correlation, and then on the similarity of the seismic traces. This allows to obtain an accurate pick, such as to be able to locate without the introduction of cubic sections as in the case of the catalogue data-set.

Finally, in the Fig. 12 we show interconnection of the events for the refined and for the catalogue data-set. The selection of pairs of events according to the maximum distance is made by considering the initial absolute localization and 5 km as a maximum distance between pairs of events. It is clear from Fig. 12-b that many events are localized outside the distribution, very far from their initial position.

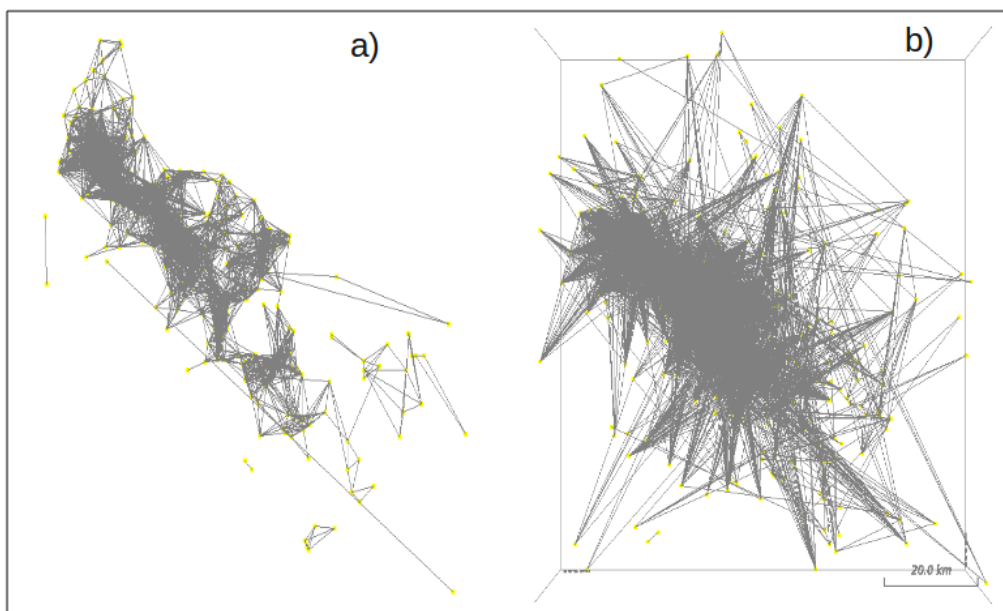


Figure 12. Plot of events inter-connections for the re-fined (a) and for the catalogue (b) data-set considering 5 km as maximum distance.

PART TWO: APPLICATIONS

The described methods allow to analyse the geological and structural characteristics of complex areas and to monitor the presence and migration of fluids assessing their role in the dynamics of tectonic, geothermal and volcanic systems.

In this thesis we chose three different complex areas of investigation: the Irpinia fault zones, The Geysers geothermal area and the Solfatara volcano.

The relevance of these three areas lies not only in their different rheological and structural nature, as they represent a seismogenic, a geothermal exploration and a volcanic area, respectively, but also in their different dimension. In particular, the investigated Irpinia area has a characteristic dimension of about 100 km; the Geysers geothermal system has a characteristic dimension of the order of few tens of km; and the scale of the Solfatara crater is of the order of one hundred meters. These different features enable us to consider the areas as "seismological laboratories", i.e. areas of interest which allow the application, validation and development of different methodologies. Depending on the characteristics, the available data-sets, the associated problems and the state of art of each area, we have chosen to apply several of the methods of analysis and investigation explained in the previous chapters.

The Irpinia fault zone is a crustal volume in southern Italy, embedding the still active fault system that generated the 1980 M 6.9 earthquake. Since 2005, the capability of detecting and locating small magnitude events in this area has been greatly improved (Stabile *et al.* 2013) through the deployment of the Irpinia Seismic Network, a dense, permanent and wide dynamic range network (ISNet; Iannaccone *et al.* 2010). Different authors (De Matteis *et al.* 2012; Matrullo *et al.* 2013; Ascione *et al.*, 2013; Amoroso *et al.* 2014) showed that the low magnitude ($M_L < 3.5$) background seismicity does not occur on a single major fault, but rather in a volume delimited by the master faults that were reactivated during the Irpinia earthquake. So the question arises whether is possible to delineate the faults using an accurate location method.

Therefore, we applied the double-difference location method in order to establish the true nature of the diffuse seismicity patten characterizing the Irpinia area (Ch. 1.4 part II).

Amoroso *et al.* (2014) adopted an iterative, linearized, tomographic approach in order to obtain P- and S-wave velocity models for the Irpinia region. The retrieved velocity models, in particular the V_P/V_S ratio one, highlight a significant fluid accumulation in highly fractured

rocks, where most of micro-seismicity occurs, within a 15-km wide volume called the 'earthquake reservoir'. Therefore, the authors assumed that the background micro-seismicity is related to the pore-pressure changes in fluid-filled cracks surrounding major faults.

On these basis, the open question was whether it is possible to deepen our knowledge of the complex area with attenuation images to better characterize the 'earthquake reservoir' in terms of porosity, saturation or fluid type. Is it possible also to make some *quantitative* consideration about the seismicity-triggering mechanism?

The answer to these questions was given through the joint use of two methods, that is, attenuation tomography and rock physical modelling. The details can be found in the next chapters (Ch. 1.5 and 1.6 part II).

The Geysers area is the greatest Enhanced Geothermal System (EGS) in the world, located in California. Geothermal systems have the potential to provide a significant contribution to the world's energy demand. In particular, an EGS consists in increasing the permeability in the rock and steam production by injecting high-pressure water into the reservoir. However, fluid injection, steam extraction and reservoir stimulation in EGS lead to induced seismicity, whose monitoring is important for both the mitigation of the side effects of industrial operations, and the continuous assessment of the reservoir's conditions. To this purpose, the dense Lawrence Berkeley National Laboratory Geysers/Calpine (BG) surface seismic network was permanently deployed in the area. The dominant interests for this area are therefore the tracking of spatial and temporal variations, on both short and long term, and the tracking of the propagation-medium parameter through the use of the high-quality seismic dataset collected at the geothermal field. The methodologies applied to this purpose are the velocity tomography, the V_p/V_s ratio temporal variation and a preliminary analysis to the implementation of the 4D tomography. The details of the application and the results can be found in the next chapter (Ch. 2 of part II).

Finally, we considered the volcanic area of the Solfatara crater, located within the active Campi Flegrei caldera, in southern Italy. Solfatara and its surroundings are characterized by the impressive magnitude of the diffuse degassing process that confirmed the relevance of the fluid and heat transport (Chiodini et al., 2001) and prompted for further research, aiming to improve the understanding of the hydrothermal system that feeds the surface phenomenon. In order to provide time-varying high-resolution images of the structure of Solfatara, a repeated active seismic experiment was carried out between September 2013 and November 2014. In this frame, the interest of our application has been to obtain an ultra-high-resolution 3D reference velocity image of the shallow hydrothermal structure of the Solfatara crater's

central part, by applying seismic tomography to the data-set acquired during the first campaign. Moreover, considering that the presence of fluids and their circulation may greatly affect the rock volume and therefore the average compressional wave velocity, we expect that the tomographic images can constrain the possible location and phase of the permeating fluids. To this purpose, we compared our seismic tomography with 2D cross-sections of resistivity (ρ) and with temperature and CO₂ flux measurements. The application details and the results can be found in the next chapter (Ch. 3 of part II).

Chapter 1: *IRPINIA* fault system

3.1 Introduction and state of art

The southern Apennines of Italy are a seismically active belt characterized by a complex crustal environment, in response to a very intense geodynamic activity. This area experienced moderate to large earthquakes in the past century. Its complex architecture is derived from the deformation of three main paleogeographic domains (Fig. 13b): the shallow water carbonates of the Apennine Platform to the West and of the Apulia Platform to the East, and the intervening Lagonegro basin, (e.g. Scandone, 1972). The crustal extension controls active tectonics and earthquake generation processes in the mountain chain, with the background seismicity being characterized by low to moderate magnitude events. The latest destructive event, the so-called Irpinia earthquake (M_s 6.9), occurred on November 23rd, 1980. This event has activated several normal fault segments during the same rupture episode itself (Bernard and Zollo, 1989).

The Irpinia fault system is a graben-like structure, characterized by two SE dipping boundary faults: the North East Boundary Fault (NEBF), and the South West Boundary Fault (SWBF). The antithetic Central Fault (CF) is contained within the crustal volume comprised between the two boundary faults (Ascione et al., 2013). The deeper part of the fault system was activated during the Irpinia earthquake, and the complex normal faulting involved the activation of both the CF and the NEBF faults (Fig. 13b-c). The highly segmented fault system at the surface is decoupled from the deep-seated major structure (Ascione et al., 2013). The decoupling is due to a sharp rheological contrast generated by a clay-rich, fluid-saturated *mélange* zone (Mazzoli et al., 2001), which is interposed between the Apulian Platform carbonates at depth and the allochthonous units (Apennine Platform and Lagonegro basin strata) located at shallow levels.

The background seismicity that characterizes chain does not occur on a single major fault, but rather in a volume, delimited by the master faults – of which only one of them, i.e. the NEBF, has been reactivated during the Irpinia earthquake (Ascione et al., 2013; Amoroso et al., 2014; De Landro et al., 2015). Plus, it occurs on an inner cluster of sub-parallel, predominantly normal faults (De Matteis et al., 2012). The present-day low-magnitude seismicity follows the same pattern of the 1980 event aftershocks, with a main elongation parallel to the strike of the fault segments activated during the Irpinia earthquake. The earthquakes occurring at the core of the Apennine chain affect the uppermost 20 km of the crust. Most the earthquakes

occur in carbonate rocks and in the underlying crystalline basement (Picentini and Marzano Mounts). In general, the depth distribution is almost nearly uniform, except in the Sele River Valley area, where a seismic gap in the upper crust above about 8 km depth is observed. This is likely due to the presence of a thick sedimentary cover that probably infills a paleo-valley (Amato & Selvaggi 1993).

We ascribed to the background seismicity the micro-seismicity characterizing the 1990-91 Potenza seismogenic fault system, suggesting that this EW striking, sub-vertical, right-lateral structure is still active at the low magnitude level. The “Potenza” earthquakes were generated within the most internal buried foreland, where it tends to deepen below the outer front of the Apulia anti-formal stack (i.e., the deepest part of the Apennine chain; Boncio et al. 2007). This means that, where present, right-lateral EW striking shear zones could be active at least as far as the buried Adriatic foreland is not involved in thrusting. With respect to the Apennine chain, the foreland buried below the outer front of the Apulia anti-formal stack is the most internal structural domain where active tectonics and seismicity are known to occur along EW striking shear zones.

There is a general consensus that EW striking structures, cutting the foreland crust, are older, pre-existing faults inherited at least from the Mesozoic times, and that the associated widespread seismicity associated is due to their reactivation under the present-day stress field, although it is not always perfectly oriented with respect to it (e.g., Di Bucci et al. 2010; Latorre et al. 2010). These structures are large regional fault zones, which dissect the foreland crust and have experienced long-lasting activity under different tectonic regimes, that is to say, under different kinematics at different times (Di Bucci et al. 2013).

The principal stress orientations, based on the inversion of micro-earthquake focal mechanisms, suggests that a unique NE trending, from horizontal minimum compression maximum (σ_3), could explain the two different faulting styles characterizing the earthquakes that occur along the chain and the E-W faults dissecting the belt (De Matteis et al., 2012), although a permutation between the maximum (σ_1) and intermediate (σ_2) stress axes is certainly required to pass from the extensional faulting in the former to the strike-slip faulting in the latter.

The analysis of micro-earthquake sequences, such as events clustered in space and time, has revealed that micro-seismicity is primarily concentrated in very limited regions along the Irpinia earthquake fault zone. These weakness zones produce repeated earthquakes and swarm-like sequences that are possibly related to pre-existing geometrical barriers.

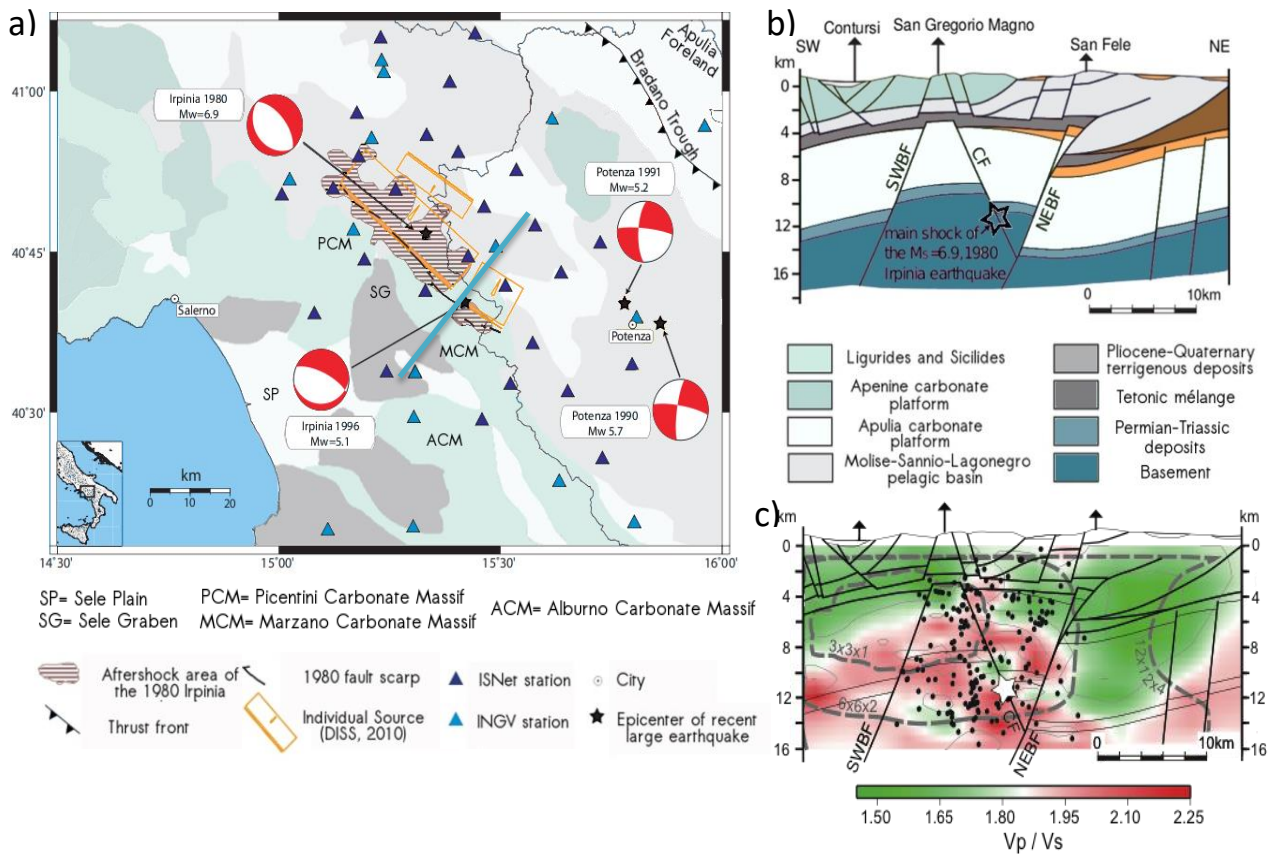


Figure 13. a) Geological sketch map of the Campania-Lucania region integrated with seismogenic source (DISS Working group 2010), location of seismic ISNet stations (blue triangles) and INGV stations (turquoise triangles), main historical earthquakes with their focal mechanisms and aftershock zones (modified after De Matteis et al. 2012). b) Cross-section, indicated with the turquoise line in a) (modified after Amoroso et al., 2014). Star shows hypocentre of the Ms 6.9, 1980 Irpinia earthquake; SWBF: SW Boundary Fault; CF: Central Fault; NEBF: NE Boundary Fault.

The anomalously large, local stress concentration may be the cause for the generation of small fractures in the zones where the fault dip changes (bend jogs) or where overlapping fault segments have their tips (offset jogs). These intensely damaged zones could be the source of the repeated earthquake activity, which could be due to the internal mechanical re-adjustments caused by from local stress release and/or to the fluid migration along the fault zone near the geometrical barrier (Stabile et al., 2012), particularly at compressional jogs where the fault slip induces the increase of pore fluid pressure.

Amoroso et al. (2014) adopted an iterative, linearized, tomographic approach in which the P and S arrival times are simultaneously inverted for the earthquakes location and velocity parameters (Latorre et al., 2004). The original dataset for the seismic tomography study consisted of more than one thousand events with local magnitude $0.1 \leq M_L \leq 3.2$, recorded by a total of 42 stations, which were operated by INGV and AMRA from August 2005 through April 2011. A cross-section cutting the 3D velocity model normally to the strike of the Apennine belt shows that, despite a smoother resolution, the tomographic P-wave model delineates the

main lithological discontinuities of the geological section in Fig. 13(b). The present-day micro-seismicity, plotted onto the same cross-section, appears to cluster within the basement and at the top of the Apulian Platform carbonates (Fig. 13b-c). Laterally, the micro-earthquakes are remarkably confined within a roughly 15 km wide block bounded by the SW and NE Boundary Faults (also including the Central Fault), along which the main shock of the Ms 6.9, 1980 earthquake nucleated (Fig. 13b). The horizontal slices through the Vp and Vs models show the occurrence of strong lateral variations of seismic velocity that occur orthogonally to the Apennine chain. A diffused high Vp/Vs ratio (Fig. 13c) occurs within the Apulian Platform carbonates located between the SW and NE Boundary Faults, the latter clearly representing a major barrier. In general, almost the entire fault-bounded block, where intense micro-seismicity occurs, is characterized by relatively high values (>1.8) of Vp/Vs. The observed high Vp/Vs indicate a densely porous/fractured rock volume that is largely water saturated (O'Connell and Budiansky, 1974; Winkler and Nur, 1979). Moreover, the estimated high Vp/Vs anomaly provides a Poisson ratio in the 0.3-0.4 range which also indicates a dominant water saturation of rocks in the investigated crustal volume (Dvorkin, 1999). The velocity models, therefore, highlight a significant fluid accumulation within a 15 km wide volume of highly fractured rock. The evidence for a highly fractured, partially fluid-saturated medium embedding the Irpinia fault zone is confirmed by Zollo et al. (2014), who studied the attenuation within the same rock volume. The background micro-seismicity is therefore attributed to pore pressure changes in the fluid-filled cracks surrounding major faults, which can trigger the episodic nucleation of moderate to large earthquakes.

1.1 Geological settings

The Campania-Lucania region (Fig. 13a) is located in the axial portion of Southern Apennines, an Adriatic-verging duplex system, orogenically transported over the flexured south-western margin of the Apulia foreland (Patacca et al. 1990). This duplex system consists of a complex architecture of carbonate horsts deriving from the Apulia Carbonate Platform (ACP), which is over thrustured with rootless nappes. The belt is located between the Tyrrhenian back-arc basin to the West and with the Bradano foredeep to the East.

The ACP consists of 7-8 km thick Mesocenozoic carbonate sequence, which overlies Permotriassic clastic deposits (Verrucano Fm., Roure et al. 1991). Plio-pleistocene terrigenous deposits stratigraphically cover the flexed ACP on the eastern margin of the Bradano Trough

(Casnadei 1998). Moving westward to the external zone of the belt, the ACP progressively dips below the rootless nappes and is in turn involved in the folds and thrusts of the thrust belt.

The orogenic stack overlying the ACP is formed by thrust sheets coming from the deformation of the stratigraphic successions, which are associated with the following main paleogeographic domains (Patacca et al. 1992):

- ❖ the Lagonegro Basin (LB, Middle Triassic-Miocene): shallow-water, shelf-margin and basinal facies successions located between the Apulia Carbonate Platform and the Western Carbonate Platforms;
- ❖ the Western Carbonate Platform succession (WCP; or Apenninic Carbonate Platform), overthrusts on the LB units. It consists of a succession of Mesozoic and Paleogene carbonate deposits;
- ❖ internal basin domains, which are related to the Sannio and Sicilide Complex.

Syntectonic terrigenous sequences do not uniformly cover the thrust sheets stack and represent the infill of the Upper Tortonian to the Lower Pleistocene satellite basins (Patacca & Scandone 2001).

The tectonics of this area is controlled by the collision between the Adriatic microplate and the Apenninic belt, derived by the convergence between the Euro-Asian and African plates. The eastward migration of the thrust- belt-foredeep-foreland system, derived from the west-dipping subduction process of the Adriatic microplate is related to the opening of the Tyrrhenian basin (Patacca et al. 1990). The front of the orogenic wedge reached the present-day location and stopped at the beginning of the middle Pleistocene (Patacca & Scandone 2004). Indeed, a geodynamic change occurred covering around 800 km, when a SW-NE extension became dominant over the core of the Apennines, as shown by geological and geomorphological analyses (Galadini, 1999; D'Agostino et al. 2001). This tectonic regime is still active, as demonstrated by breakout and seismicity data (Montone *et al.* 1999; Pantosti & Valensise 2001; De Matteis et al. 2012).

The Campania-Lucania Apenninic belt is one of the regions in Italy with the highest seismogenic potential, having experienced historical and recent destructive earthquakes. The most recent destructive earthquake was the 23 November 1980 M_s 6.9 Irpinia earthquake, generated by the rupture of at least three distinct normal fault segments (Bernard & Zollo 1989). Since the 1980 earthquake, the largest recorded event within its epicentral area (the 3 April 1996 M_L 4.9 earthquake) was also characterized by a normal-faulting mechanism (Fig. 13a; Cocco et al. 1999).

In the surroundings of the city of Potenza, about 60 km southeast of the 1980 Irpinia mainshock location, a strike-slip fault zone is located right where two moderate magnitude

seismic sequences occurred between 1990 and 1991 (Ekstrom 1994). The two $M_L \sim 5$ mainshocks were characterized by strike-slip faulting mechanisms, the preferred fault planes having an East–West orientation (Di Luccio et al. 2005).

1.2 Seismic network and data

Since 2005, the capability of detecting and locating small magnitude events in this area has been greatly improved (Stabile et al. 2013) with the deployment of a dense, wide dynamic range: the Irpinia Seismic Network (ISNet; Iannaccone et al. 2010). Presently, the area exhibits low magnitude seismicity ($M_L < 3.5$) primarily concentrated in very limited regions along the 1980 Irpinia and the 1990-1991 Potenza earthquake fault zones (De Matteis et al. 2012). These weakness zones produce repeated earthquakes and swarm-type micro-earthquakes sequences, which are concentrated in a few specific zones of the fault system (Stabile et al. 2012).

We analysed a seismic data-set consisting of 17,202 traces recorded by 42 ISNet and stations of Istituto Nazionale di Geofisica e Vulcanologia (INGV) network from 1,312 micro-earthquakes, with a moment magnitude ranging between 0.9 and 3.1, which occurred from August 2005 to April 2011 (Fig. 14, De Matteis et al. 2012).

We used the first P - and S -wave arrival times of earthquakes that have been recorded by at least four manually picked stations. A weighting factor inversely related to the uncertainty on arrival time picking has been assigned. A selection based on the location quality was preliminarily performed: 704 events with at least 5 P and 2 S picked arrival times, an azimuthal gaps greater than 180 degrees and a RMS of location greater than 0.5 s have been taken into account for this study. A total amount of 10,875 absolute arrival times have been collected and combined to construct the differential times (see section 3.3). The differential times obtained from this procedure constitute the Manually Refined Picking (MRP) dataset. We can improve the location precision by using the arrival times refined by waveform cross-correlation techniques. This technique was used to construct a cross-correlation re-fined picking dataset, which was used separately from the MRP dataset in order to validate the locations results obtained from the previous data-set.

In order to enhance and improve the accuracy of the S -wave picking we have applied a phase picking technique based on polarization filtering and on a waveform coherence analysis (Amoroso et al. 2012). In order to obtain highly accurate, arrival-time readings, the automatic

refined re-picking technique proposed by Rowe et al. (2002) has been used. The waveforms of all the analysed seismic events have been preliminary organized in common

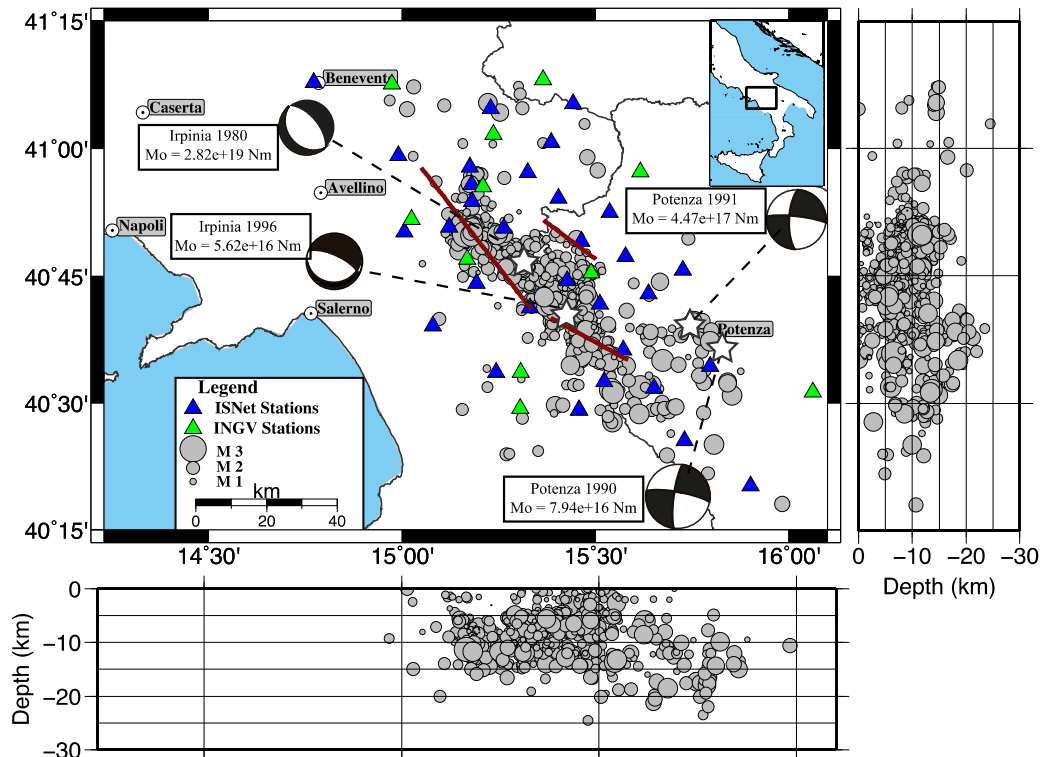


Figure 14. Epicentral distribution of the analysed seismic events (red dots) recorded by ISNet (blue triangles) and INGV stations (green triangles) in August 2005 through April 2011 (from Zollo et al., 2014).

receiver gathers. For each pair of traces recorded at the same station, the similarity was evaluated by using a cross-correlation function in a window bracketing a reference picking time. The cross-correlation values are used to identify clusters of highly similar events, and to estimate relative lags within the same cluster. The pick adjustment and associated uncertainty is therefore evaluated through an iterative conjugate gradient technique. The uncertainty on refined picking measurements is assigned as the standard deviation, after estimation via a Monte Carlo sampling technique (Tarantola, 2005). The quality check of this selected dataset provided an estimation of the uncertainty modal value of 2.6 microseconds for P waves and 3.5 microseconds for S waves, corresponding to an extremely high quality data-set. With this technique we have finally obtained 6,756 absolute arrival times, corresponding to 513 events, and we have combined them to obtain the differential times that compose the cross-correlation re-refined picking (CRP) data-set.

1.3 Station residuals variations

We will show an application example of the method discussed in the previous section, which will allow us to analyse the temporal variation of the location and the arrival time residuals.

The test area is the Campanian-Lucanian region in the South Apennines, embedding the fault system that generated the 1980, MS 6.9 earthquake in Irpinia. The seismic data-set consists of 17,202 traces recorded by a 42 ISNet and INGV station from 1,312 micro-earthquakes. The earthquakes have a moment magnitude ranging between 0.9 and 3.1 and occurred from August 2005 to April 2011 (Fig. 15). We used 3D P- and S-wave velocity models, which were optimized for the area under study (Amoroso O. et al 2014).

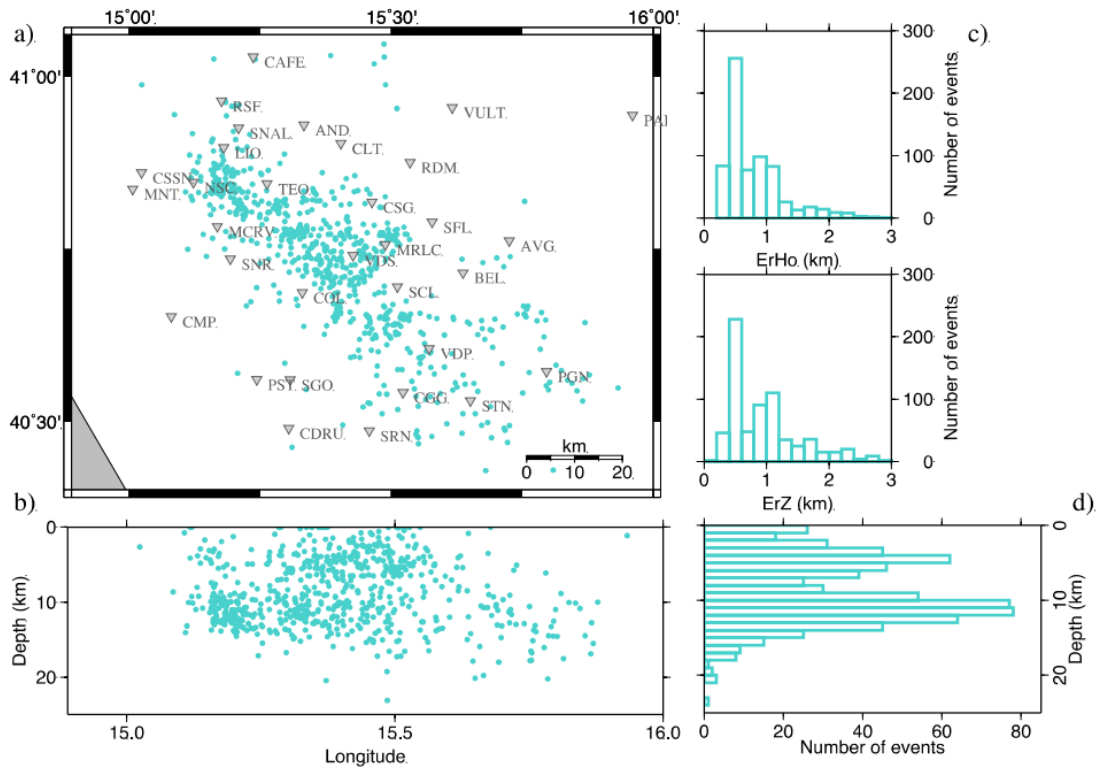


Figure 15. (a) Earthquake Non Linear Location of seismicity from 2005 August to 2011 April from catalogue data (turquoise dots). (b) East-West vertical section of the seismicity. (c) Comparison between vertical and horizontal localization errors. (d) Histogram of the events as function of depth.

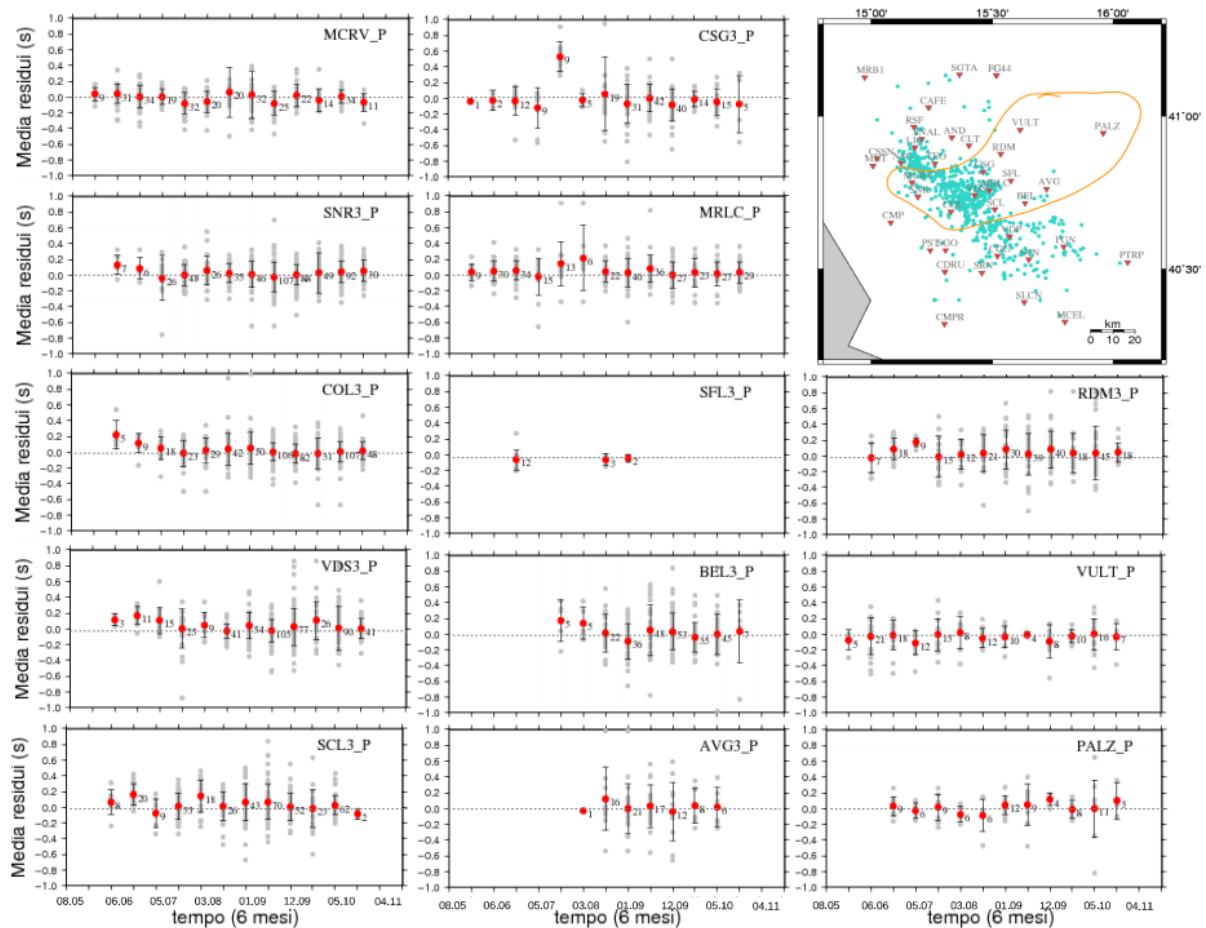


Figure 16. *P*-phase time residuals. Plot of the *P*-phase location residuals for the central stations of ISNet network. We show mean (red dots) and standard deviations (black error bar) of the location residuals for each station in each time interval of 6 month. In the upper right there is the map of the located events (turquoise dots) and the stations positions (red inverse triangle). The orange line delimits the stations of which are plotted the residuals

First we divided the events in time intervals (epochs) of six months, with an overlapping interval of a month. For each station and epoch we calculate the average arrival time residuals and their standard deviation for all the recorded events, separately for the *P* and *S* waves. Finally, we have the average station residuals versus epoch, for nearby stations to assess possible similarities (Fig. 16 and Fig. 17). This analysis is aimed at detecting and locating possible space-time changes occurring in the shallow crustal medium beneath the stations during the analysed period. Although the analysis is preliminary, it is worth to note the similarity of the mean-residual vs time series between adjacent stations (e.g. MCRV, CSG3, SNR3, MRLC) and the occurrence of changes in mean residuals at approximately the same epoch, such as the positive variation at the CSG3 and MRLC stations during epochs 5 and 6.

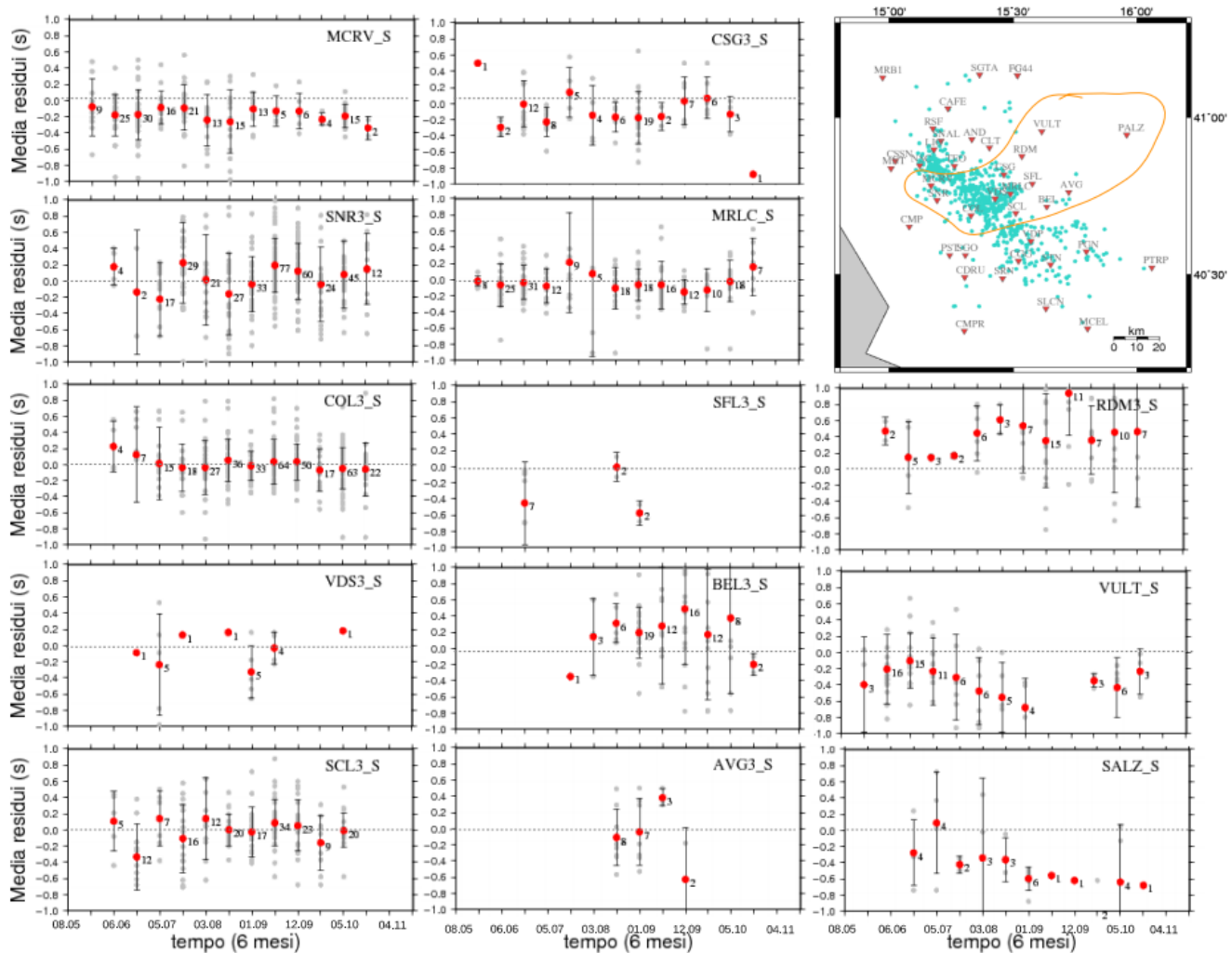


Figure 17. *S*-phase time residuals. Plot of the *S*-phase location residuals for the central stations of ISNet network. We show mean (red dots) and standard deviations (black error bar) of the location residuals for each station in each time interval of 6 month. In the upper right there is the map of the located events (turquoise dots) and the stations positions (red inverse triangle). The orange line delimits the stations of which are plotted the residuals.

1.4 Absolute and double-difference location of micro-earthquakes

An innovative double-difference location method has been applied to the seismicity (1,312 micro-earthquakes) recorded by the 42 ISNet and INGV stations from August 2005 to April 2011 along the Campania-Lucania Apennine chain (Southern Italy). The proposed methodology solves the double-difference equations (Waldhauser & Ellsworth 2000) by using the non-linear, global-search, probabilistic location approach developed by Lomax et al. (2000) instead of linearized approaches. Moreover, the methodology gives the advantage of relocating the seismicity by using the same 3D P- and S-wave velocity model (and by considering station elevations) adopted for the absolute location of events. This is a crucial condition for more reliable and comprehensive dd locations in complex media such as the area investigated in this study. Indeed, even though the double-difference technique allows

for the minimisation of errors due to un-modelled velocity structures, it has been shown (e.g., Michelini & Lomax 2004) that the use of an inappropriate 1D velocity model will, in most cases, lead to bias and error in the dd locations. Therefore, the combination of the proposed methodology with cross-correlation differential times allowed us to perform a robust, high-resolution study in order to explore new insights concerning the distribution and the geometry of the analysed micro-seismicity. Synthetic tests are also carried out in order to assess the performance of the methodology and the parameter resolution achievable from the available data. This analysis is included in the paper De Landro et al. (2015) published on *Geophysical Journal International*.

In the present analysis, we qualitatively compared the quality of the cross-correlation refined picking data with the manually revised ones and verified that the two data-sets provide similar accuracy in earthquake locations. Due to a higher number of events, whose location is obtained by manually revised times, we finally preferred to ground on this data-set for the interpretation of results and namely for the identification of the “discontinuity” in the seismicity spatial distribution. This factor provided new insights on the geometry of the active faults and on their relation to the geological structure and to the present tectonic stress regime.

For both data-sets we have used the same location procedure, based on the maximum inter-event distance, to properly compare the results of the earthquake locations. For this reason, and in order to use a more inclusive criterion of event selection than the minimum cross-correlation coefficient one, an absolute CRP data-set was chosen.

The software NLLoc and the tool Loc2ddct, which allows to calculate the differential times by fixing the maximum distance between an event couple, has been used to obtain the two inputs of the dd location code, the initial absolute location of events and the corresponding differential travel time.

In order to obtain more accurate and reliable locations by using the MRP data-set we have operated a subdivision in subsets of events located in overlapping rectangular sub-areas of the region under study. We consider rectangular boxes with a size of $10 \times 10 \times 30 \text{ km}^3$ and overlapping over an area of $10 \times 5 \text{ km}^2$. For each box a maximum of one hundred events has been considered.

Conversely, for the CRP data-set we have used a maximum inter-event distance of 5, with no need of a previous section sub-division. We used 3D P - and S -wave velocity models obtained with an iterative, linearized, tomographic approach in which the P and S arrival times are simultaneously inverted for the earthquake locations and velocity parameters (Amoroso et al., 2014a). The 3D P -wave velocity model is characterized by the presence of a strong lateral

velocity variation at 4-8 km depth, along the orthogonal direction to the Apennine chain, thus defining two domains characterized by relatively low (3.5-4.8 km/s) and high (5.2-6.5 km/s) P -wave velocities. The S -wave velocity model also shows changes along the SW-NE direction but they are smaller than the one observed for P -wave velocity.

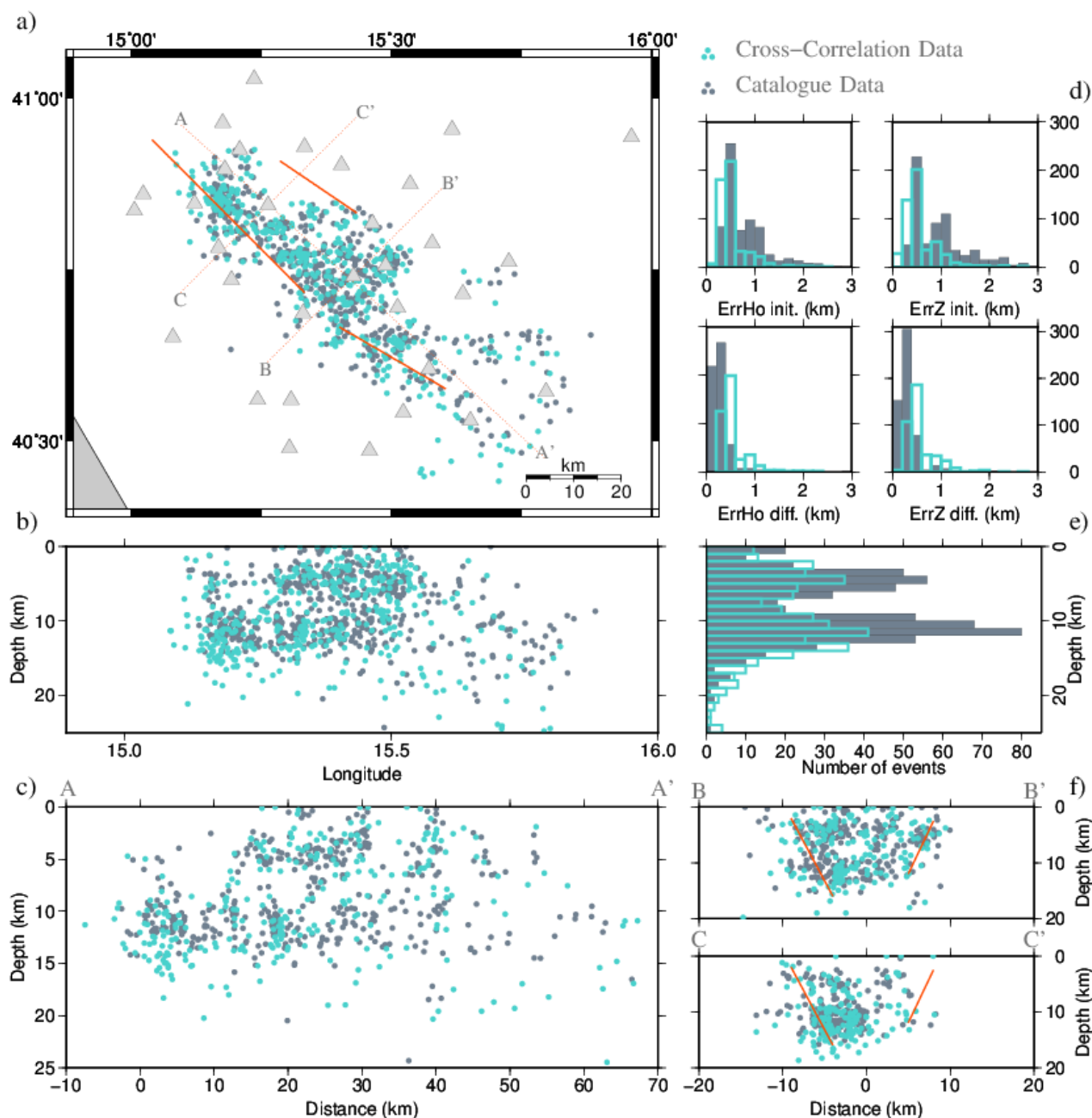


Figure 18. a) Double-difference earthquake location of seismicity from 2005 August to 2011 April, from MRP data (in grey) and from CRP data (in turquoise). Red lines are the surface projection of the three fault segments that ruptured during the 1980 Irpinia earthquake (Pantosti & Valensise 1990). b) East-West vertical section of the seismicity. c) Anti-Apenninic AA' vertical section of seismicity and histogram of events number moving in the NW-SE direction along the same profile. d) Comparison between horizontal (left) and vertical (right) errors of absolute location (light grey) and dd locations for the MRP data-set (top, dark grey) and CRP data-set (bottom, turquoise). e) Histogram of the events as function of depth. f) Earthquake cross-section along the profiles BB' and CC' indicated in the map in c). From De Landro et al. (2015)

The mean RMS of the final dd location is 0.13 s for the MRP data-set and 0.15 s for the RRP data-set. In Fig. 19 and Fig. 20 we show the comparison between the travel-times residuals, the RMS and location errors of the initial absolute locations and the final relative locations for the catalogue and the re-fined data-set. For the catalogue data-set, residual histograms of the final relative location are improved both in terms of travel-times residual distribution of a narrower RMS, which decreases on average by 0.05 s, and of location errors, which decrease on average by 0.5 km. For the re-fined data-set the residual histograms of final relative location are improved both in terms of travel-times residual distribution of a narrower RMS, which decreases on average of 0.1 s, and of location errors, which decrease on average by 0.5 km. The results showed in these figures allow to assess the improvement of the results by using the NLDiffLoc code instead of absolute location code.

The two dd epicentral distributions of the events, Fig 18.c-d, exhibit very similar characteristics, both in terms of distribution centroids and relative inter-event distances. In particular, according to the previous works (De Matteis et al. 2012; Matrullo et al. 2013; Amoroso et al. 2014), the background seismicity shows a diffuse distribution along the NW-SE direction of the Apennine chain for the Irpinia area, and in the EW direction for the Potenza area. The map view in Fig. 18c, together with the histogram of the events number in the NW-SE direction in the d panel, shows that there is one continuous broad zone of seismicity. However, a rapid decrease in the rate of events in the SE area is observed. These two zones to the NW and to the SE, characterized by different rates of seismicity, are spatially well correlated to the fault segments activated during the 1980 earthquake and separated by a zone of low seismicity. The zone to the NW is associated with the 1980 fault segment that first ruptured and has a higher density of events than the SE zone, which is associated with the second fault segment that ruptured 18 s after the first.

The depth of events ranges from a few km to about 20 km, Fig. 18d, with a higher density of events at around 5 and 12 km depth, respectively (Fig. 18g). The error histograms of absolute and relative locations are shown in Fig. 18f. The horizontal location error (Er_{Ho} , defined as the length of the largest projection of the three principal errors on a horizontal plane) and the depth error (Er_{zZ} , defined as the largest projection of the three principal errors on a vertical line) decrease significantly with the use of the dd technique. In particular, both dd location errors are smaller than 0.5 km for the most of the events.

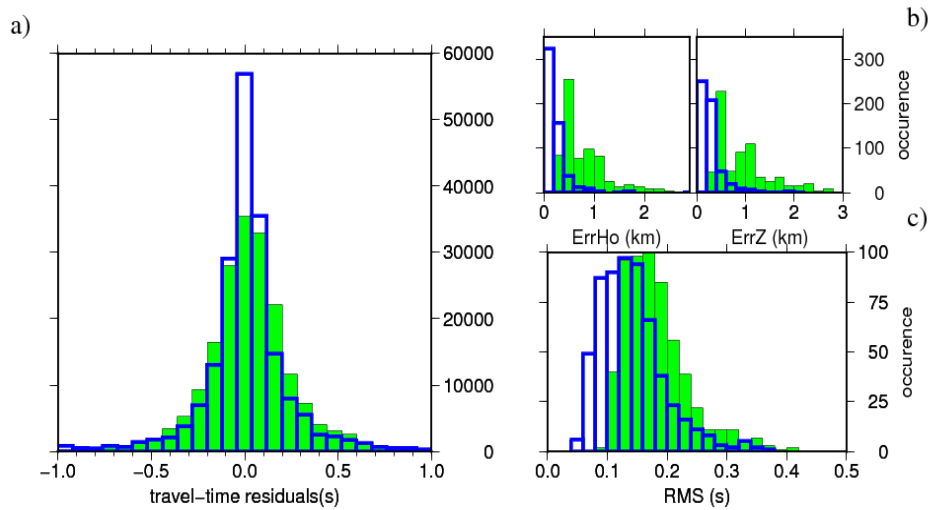


Figure 19. a) Comparison between the double-difference travel-time residuals of the initial absolute location (green) and the final relative location (blue) for the catalogue data-set. b) comparison between the horizontal (right) and vertical (left) location errors. c) comparison between RMS. From De Landro et al. (2015).

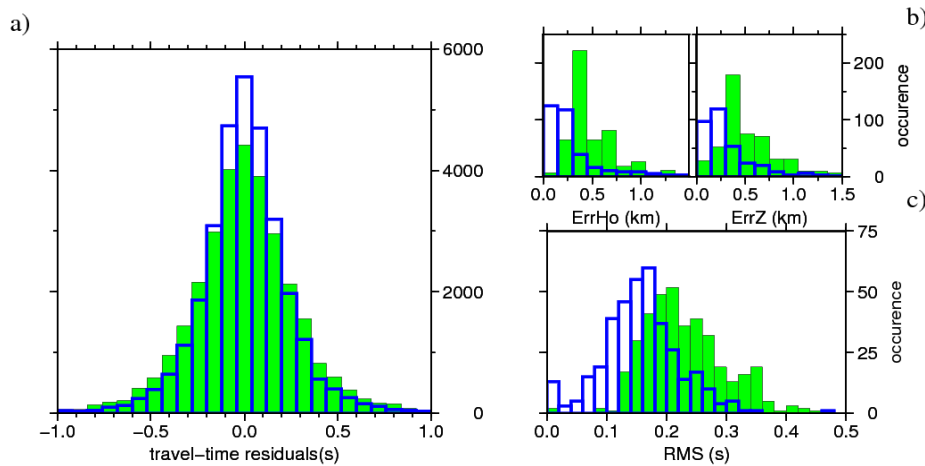


Figure 20. a) Comparison between the double-difference travel-time residuals of the initial absolute location (green) and the final relative location (blue) for the re-fined data-set. b) comparison between the horizontal (right) and vertical (left) location errors. c) comparison between RMS. From De Landro et al. (2015).

The cross-section in Fig. 18h indicates that the seismicity along the Apennine chain does not occur on a single, isolated fault but instead within a volume that is possibly delimited by the faults activated during the 1980 earthquake. This is consistent with the extensional tectonic stress regime characterizing the South Apennines region, where the seismicity rather occurs along multiple, sub-parallel and en-echelon normal faults associated to the present-day tectonic deformation that act along the Apenninic belt (De Matteis et al. 2012; Rigo et al. 1996).

The location errors in Fig. 18f show that the two data-sets provide similar accuracy in double-difference earthquake locations. Moreover, the two dd location distributions show the same features. Due to a higher number of events in the MRP data-set, we have chosen this one for the results analysis.

In order to underline the potentiality of a probabilistic approach, we will show in the Fig. 21 and fig.22 histograms and plots of the PDF for some events. The histograms show that for some events the value of maximum likelihood is unique and well insulated, while for other events, for which the PDF is more irregular, there can be several values of maximum likelihood. Hence comes the choice of using a probabilistic technique that allows the construction of the PDF, and then a more thorough exploration of the investigation area in these cases of irregular probability distributions.

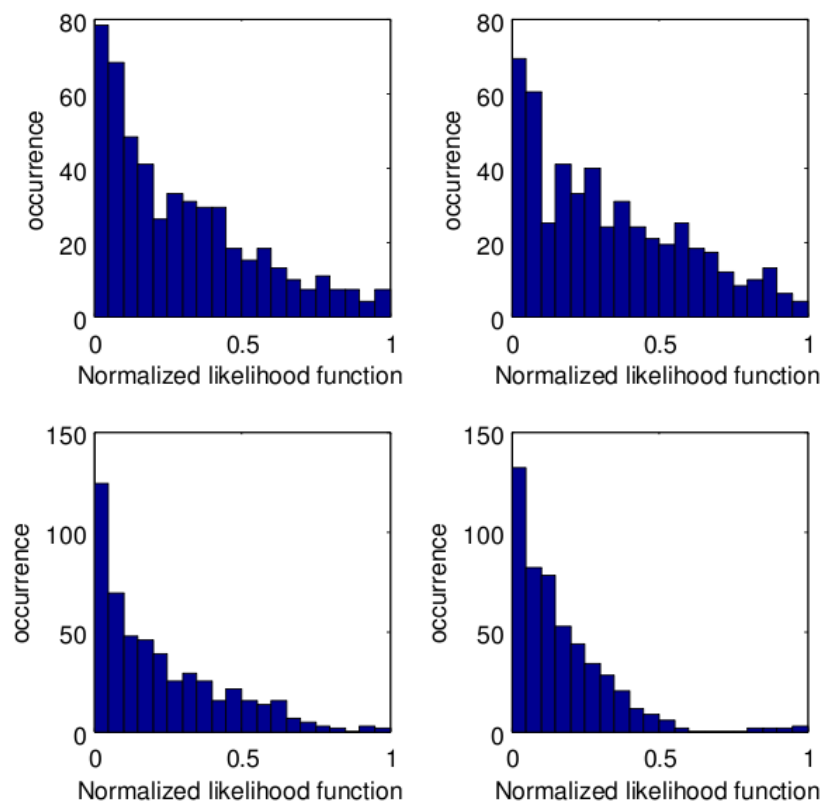


Figure 21. Histograms of normalized likelihood function for four different events of the real catalogue data-set localized with the 3D-velocity model. From De Landro et al 2015.

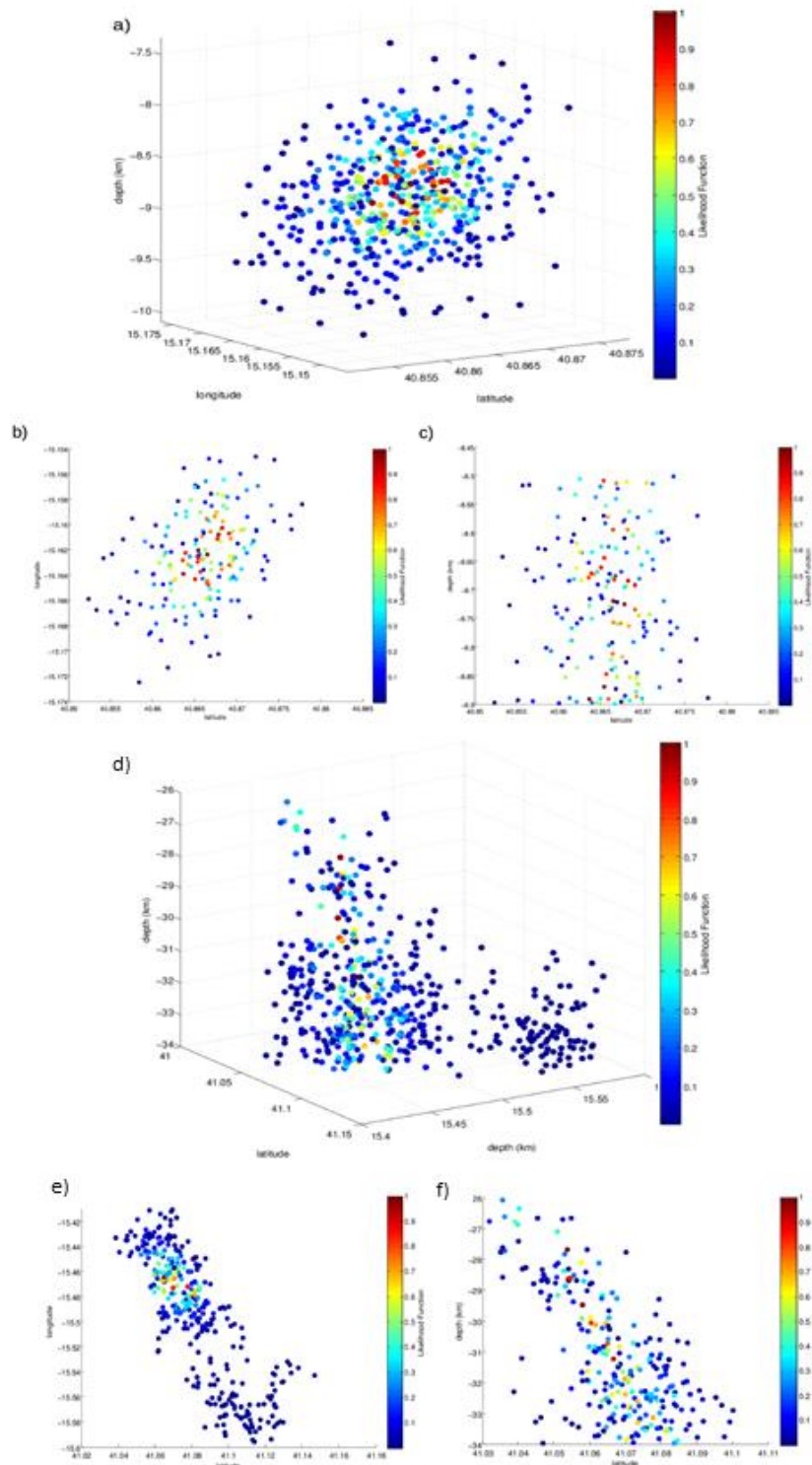


Figure 22. Plot of the normalized ellipsoidal likelihood function of two events, one of the catalogue data-set (a,b e c) and one of a re-fined data-set (d,e and f) located in the 3D velocity model. a-d) Normalized likelihood function in 3D. b-e) Likelihood function section in the latitude-longitude plane around the maximum likelihood depth. c-f) Likelihood function section in the latitude-depth plane around the maximum likelihood longitude. From De Landro et al 2015.

The most important result of this analysis is the evidence, from both the distribution of seismicity and the tomography, of the presence of a rheological "discontinuity" (Fig. 23). Indeed, in the south-eastern part of the Marzano massif, the alignment of the SW-NE epicentres and the abrupt limit of seismicity in the orthogonal direction to the Apennine chain are clearly visible. We hypothesize that this "barrier" can be due to the contact between units with a different rheological behaviour in response to the NE-SW stress regime acting in the chain: carbonate units (ACP) at NW and the most recent basinal facies (LB) at SE (e.g., Pescatore et al. 1999; Scrocca et al. 2005). It appears indeed that the seismicity distribution is controlled by the geometry of the ACP (Improta et al. 2003): the "barrier" in the seismicity highlighted by these data is actually located between a high and a low in the Apulian carbonates (Fig. 23a). This is more evident in correspondence of a low depth of ACP (Fig. 23a) where a seismic gap is observed down to 6 km at depth. The presence of surface deposits of the plio-Pleistocene is a consequence of the presence of a depression of the Apulian carbonates.

This is also confirmed by the 3D velocity model retrieved in the area which shows, by moving in the SW-NE direction, an in-depth of the Apulian Platform and a decrease in the rate of events in the area corresponding to the basinal deposits (Fig. 23b). Thus, the different rheology of contact geological formations leads to a substantial decrease in the rate of seismicity, moving in SW direction.

A schematic geological interpretation of the BB' section (Fig. 23b) is showed in Fig. 24. In order to construct this figure the distribution of relocated seismicity, the tomographic images and the topography of the Apulian Platform have been jointly used. The various geological formations are shown at different depths: the shallowest area of basinal deposits between 0 and 2 km; the Lagonegro unit area, where seismic waves have a velocity between 4.4 and 6.2 km/s; in contact with this unit, the Apulian platform, whose top is between 5 and 6 km in depth, in which wave velocity is ranging between 5.6 and 6.3 km/s; and finally the bedrock from 9-12 km down.

We suggest that this discontinuity is a transverse fault in the basement overlying the Apulian carbonates. This fault is oriented in such a way as not to be easily activated in the current stress field (the strike of this structure is approximately parallel to the axis of minimum compression, NE-SW), and could constitute a barrier to the propagation of seismic ruptures towards SE.

This hypothesis is in agreement with the previous work (Bernard & Zollo 1989; Cocco et al. 1999), according to which the cause of the delay time in the dislocation of the first two

segments of the 1980 earthquake was associated to the possible presence of a geometrical "barrier". Indeed, it is observed that the lower limit of the DISS fault (DISS Working Group 2010) relative to the first segment corresponds to the discontinuity of the seismicity (Fig. 18a).

During the 1980 Irpinia earthquake, the Monte Marzano segment ruptured first, and its nucleation occurred near its north-eastern edge with a normal fault mechanism on a plane dipping 60° towards NE. The rupture propagated bilaterally for 15 km towards NE and for a few km in SW direction.

The southern segment rupture started 18 s after the nucleation of the first event and 15 km SE of its hypocentre, on a low-angle normal fault (30°) dipping toward NE (Bernard & Zollo 1989). This discontinuity has therefore, formed a "barrier" that has resisted and slowed down the evolution of the rupture towards SE, forcing it to change its geometry. It then restarted with a delay of about 20 seconds along a low-angle deeper fault, where the fracture has probably found again the carbonate platform (Bernard & Zollo 1989).

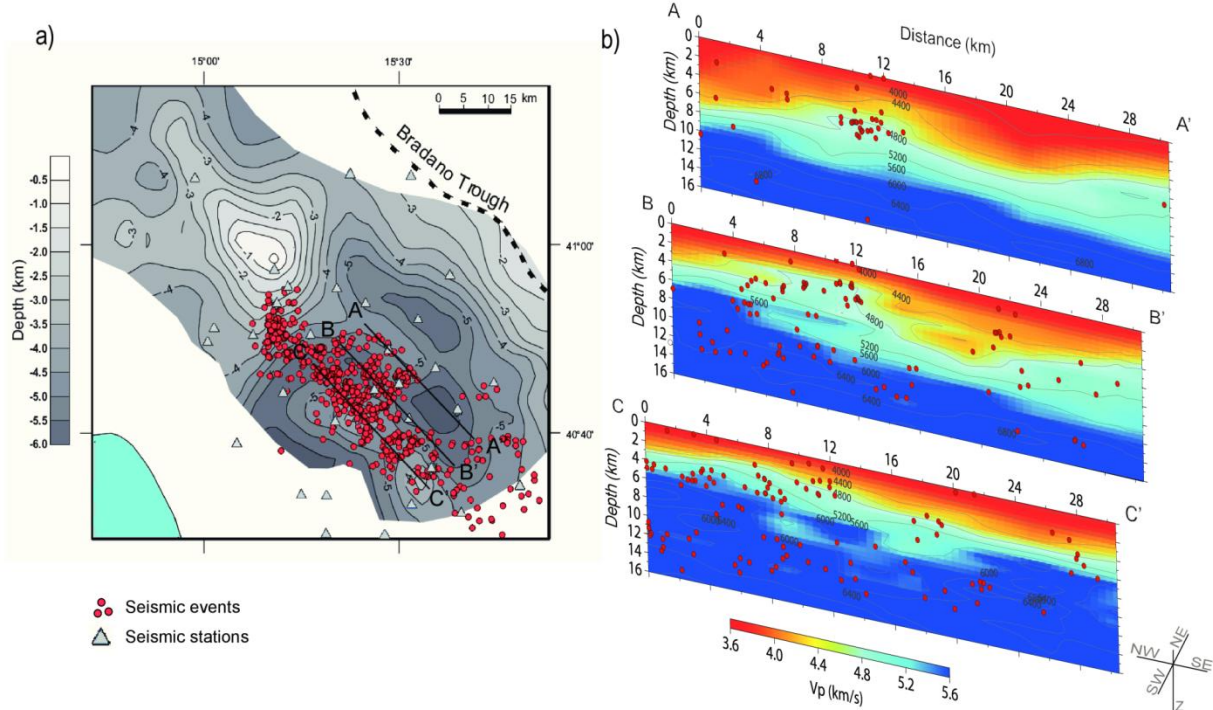


Figure 23. a) Comparison of the location of seismicity with the topography of the Apulian Carbonate Platform top (modified after Improta et al. 2003). b) Comparison of tomographic cross-sections reported in map a) and the earthquake occurred in this area. From De Landro et al 2015

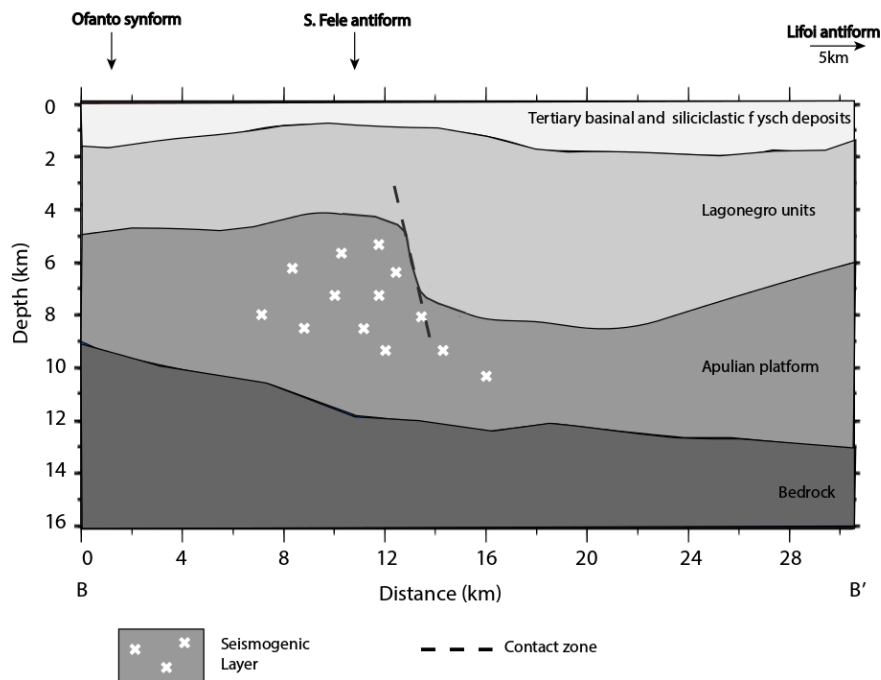


Figure 24. Schematic geological interpretation. The positions of the interfaces are deduced from both tomographic model and hypocentre-relocated events. The name of the lithologies and the position of main topographic indications are also indicated and supposed from Improta et al. (2003). The crosses indicate the rough position of the retrieved hypocentres. A dashed line is used to represent the hypothetical "barrier"/ fault scarp. From De Landro et al 2015.

1.5 Attenuation tomography

Here, we propose to use the estimates of tomographic velocity and attenuation values for a comprehensive seismic interpretation of the 1980 Irpinia earthquake fault zone. We performed an attenuation tomographic inversion, which provided 3-D images of the anelastic attenuation properties in terms of body wave quality factors (Q_P and Q_S). These quantitative images complement the already existing velocity images inferred from local earthquake tomography models (Amoroso et al., 2014). The following work was insert in the paper Amoroso et al. (2016a), under second review on *Geophysical Research Letters*.

1.5.1 Data processing

For the area under study, Zollo et al. (2014) analysed 717 events in the moment range $4 \cdot 10^9$ - $2 \cdot 10^{14}$ Nm recorded at ISNet (Irpinia Seismic Network) and INGV (Istituto Nazionale di Geofisica e Vulcanologia) network with the aim to determine the P and S quality factors with two different techniques. In the most general formulation of the anelastic attenuation model, the coefficient t^* is frequency-dependent through a frequency-dependent quality factor $Q(\omega)$ and, as a first order approximation, it can be written as (e.g. Morozov, 2008):

$$t_c^*(\omega) = \frac{T_c}{Q_o \omega^n} \quad (53)$$

where the symbol n is a positive real number and Q_o is the quality factor evaluated at the reference frequency of 1 Hz. For small magnitude earthquakes ($M_L < 1.0$), the quantity t^* is determined from the low-frequency spectral decay in a frequency band whose upper limit is given by the event corner frequency; for the larger events in the data-set, the value t^* is instead computed by using a multi-step, iterative inversion of spectral parameters. Based on the spectral fitting method, Zollo et al. (2014) verified that the attenuation model with $n=0$ in (2) had to be preferred relative to a frequency-dependent model both P and S waves. They estimated the crustal median values $Q_P = 200$ with confidence limit (110, 360) and $Q_S = 245$ with confidence limit (150, 375).

Here we use the measurements of t^* by Zollo et al. (2014) which consist of 4801 t^* measures for P waves and 1833 t^* measures for S waves, relative to 670 earthquakes with local magnitude ranging between 0.1 and 3.4. Fig. 25 shows the distribution of t^* -residuals (e.g. the difference between the observed and theoretical t^*) as a function of the hypocentral

distances. The theoretical t^* values have been computed using the estimated median crustal values.

1.5.2 Inversion strategy

The stations/events distribution in the seismic area under consideration allowed us to investigate a volume of $100 \times 100 \times 20 \text{ km}^3$ covered by a total of 42 ISNet and INGV stations. In order to perform the 3-D attenuation tomography, we used a modified version of the inversion code originally used by Amoroso et al. (2014) to perform the travel time inversion. We inverted the t^* data for Q following a *multiscale* strategy (Zollo et al., 2002) whereby several optimization runs are performed by progressively increasing the density of grid points describing the attenuation model (more details in AM, (Latorre et al., 2004)). We used three different grids having spacing equal to $12 \times 12 \times 4 \text{ km}^3$ (parametrization A), $6 \times 6 \times 2 \text{ km}^3$ (parametrization B) and $3 \times 3 \times 1 \text{ km}^3$ (parametrization C). Three different inversion runs have been performed, in each of them the rays were traced in the 3D velocity model while the Q -model obtained with the previous parameterization is chosen as the initial attenuation model. The attenuation models for P and S waves have been obtained by distinct, separate inversion of the corresponding t^* data-sets.

In order to obtain robust Q_P and Q_S starting models for the 3D inversions, we preliminary investigated the optimal 1-D attenuation model, starting with four different homogenous models $Q_P = Q_S$ both ranging between 200 and 1000. We performed a series of inversion, by parameterizing the medium with a very coarse grid in the horizontal direction respect to the vertical ($25 \times 25 \times 1 \text{ km}^3$). For each investigated model a 1D profile has been obtained by averaging the values of Q at the nodes located at the same depth. We therefore compared the obtained 1D models, and observed that between 0 and 14 km the Q vertical profiles look very similar independently on the initial Q value. This is the depth range where the highest resolution is expected from the depth distribution of earthquakes. Finally we choose the 1D Q -velocity model as the one obtained starting from the initial homogenous model with $Q_P = 200$ for the P attenuation model and $Q_S = 245$ for the S attenuation. These values are consistent with the median values determined from the same dataset by Zollo et al. (2014).

We selected the optimal damping parameter and smoothing coefficient, for each parameterization, running a series of inversions with a large range of values and plotting the data variance versus model variance trade-off curves (Eberhart-Phillips, 1986). The smoothing of the solution is achieved by constraining the Laplacian of the attenuation field to be zero (Benz et al., 1996).

To identify the model regions presenting high resolution and low smearing, we computed the derivative weight sum (DWS), which measures the ray density in the neighbourhood of every node (Hauksson and Shearer, 2006). The threshold value of DWS delimiting the well-resolved area was calibrated by comparing the diagonal elements of the resolution matrix and the spread function (Michelini and McEvelly, 1991). This comparison was made only for the parametrizations A and B, since the resolution matrix for parameterization C could not be computed due to the large model size.

1.5.3 3D P- and S-wave attenuation tomography

For Q_P and Q_S attenuation models, the initial and final t^* residuals distribution is displayed in Fig. 25. For final models, the root mean square value of residuals (RMS) shows a reduction of 34% for the Q_P inversion and 39% for the QS inversion relative to the initial reference models (see Fig. 25). According to the resolution analysis, the extent of the best-resolved volumes depends on the chosen parameterization, and generally decreases as the grid step decreases (see Fig. 27, 28 and 29). The well-resolved areas have been outlined using the results of the DWS. These values show that Q_P and Q_S are well resolved from 0 to 14.5 km depth for the A and B parameterizations, while the well-resolved area is less extended for parameterization C and ranges from 2.5 km to 10.5 km depth (Fig. 27c-f). For this reason hereinafter will be commented only the results for the A and B parameterizations.

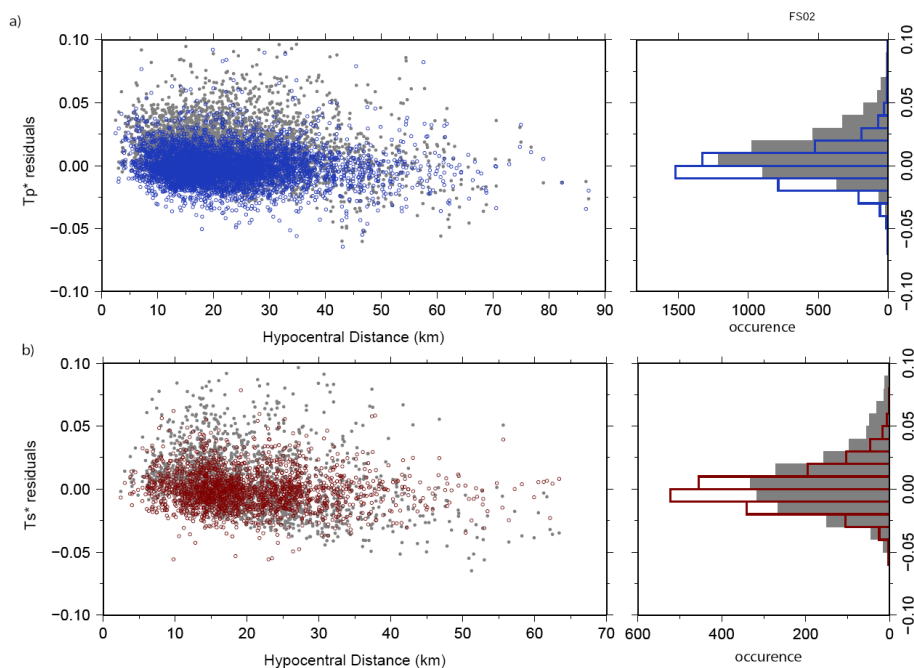


Figure 25. t^* residuals (difference between observed and computed t^*) as a function of the hypocentral distances and as a histogram for different attenuation models. (a) t_p^* residuals computed with respect to the starting model (grey dots and line) and 3 D final attenuation model (blue dots and line). (b) Same as (a), but for t_s^*

The 3D Q_P and Q_S models exhibit significant spatial variation (Fig. 26a-b-c). The Q_P model with parameterization A shows a slight increase of the values with depth, while with parameterization B the increase with depth is sharper, with Q_P reaching values ranging from 350 to 850 in the central part of the model, confined between the boundary faults (Fig. 26a) at depths between 8 and 12 km (Fig. 26c). This high- Q_P anomaly is spatially correlated with the fault structure associated with the 1980 Irpinia earthquake, in particular with the location and geometry of its first activated fault segment (Bernard and Zollo, 1989). The Q_S model also shows (Fig. 26b), with both parameterizations A and B, strong lateral variations along a SW-NE section with a major transition occurring in correspondence with the Ms 6.9, 1980 earthquake rupture and the north-eastern edge of the uplifted pre-Tertiary limestone. In its cross-section representation with parameterization B (Fig. 26d) the Q_S model clearly delineates the transition between the Apulian Carbonate platform and the basement at about 7 km depth with an increase of values from 400 to 1000. The attenuation factors Q_P and Q_S have a different pattern maybe due to their distinct physical nature, related to the different frequency content of the related waves.

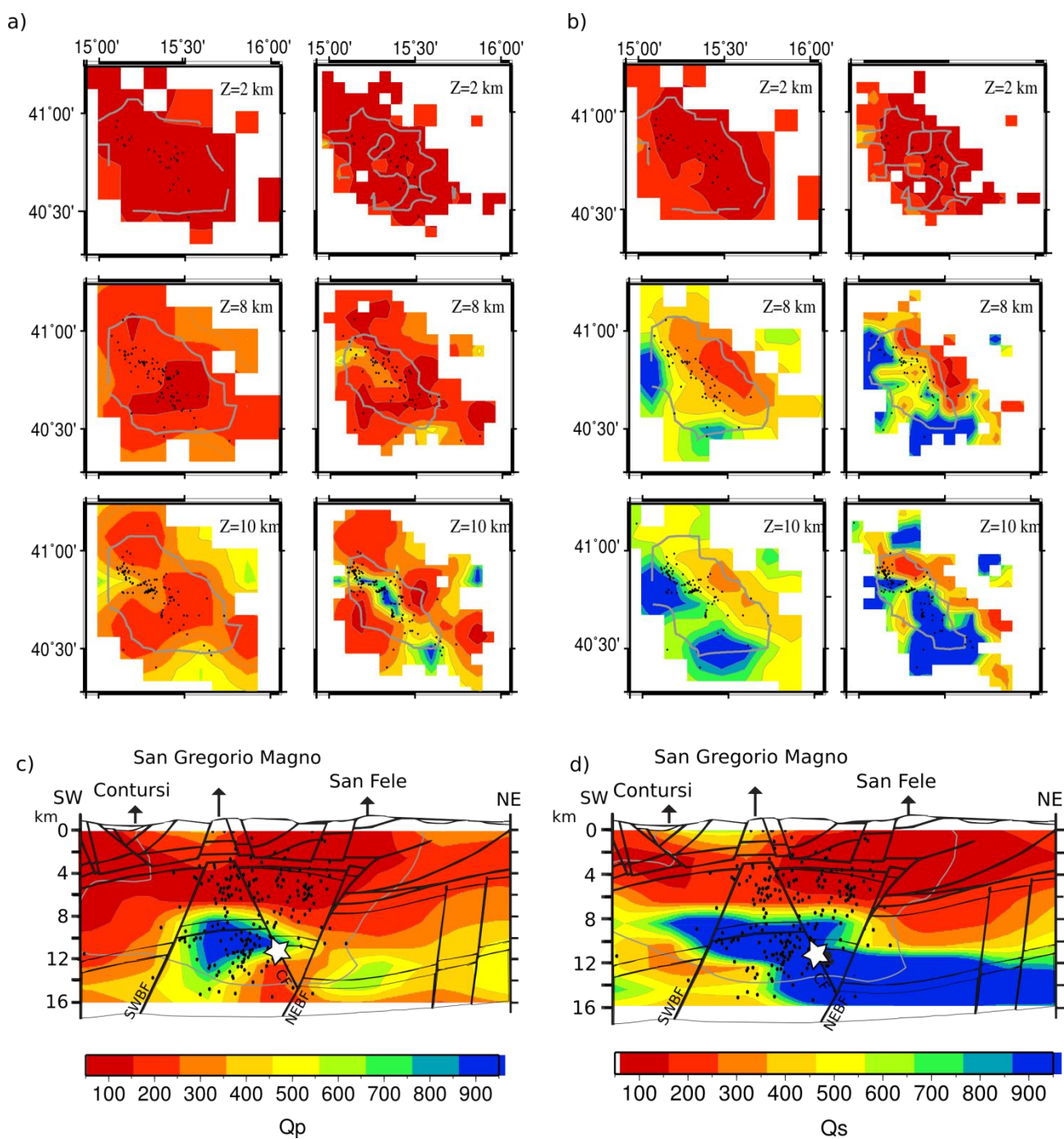


Figure 26. 3-D attenuation models. Horizontal slice through Q_p (a) and Q_s (b) attenuation models for parametrization A (left panels) and B (right panels), at 2, 8 and 10 km depths. Grey curves delimit the well-resolved regions of the model according to the resolution analysis. Black dots represent the earthquake located in a range of 1 km around each layer depth. Q_p (c) and Q_s (d) attenuation models, for parameterization B, and micro-earthquake locations projected onto the cross section located in Figure 1a (refer to Fig. 1b for the tectonic contacts and geological units). White curves delimit the well-resolved regions of the model according to the resolution analysis.

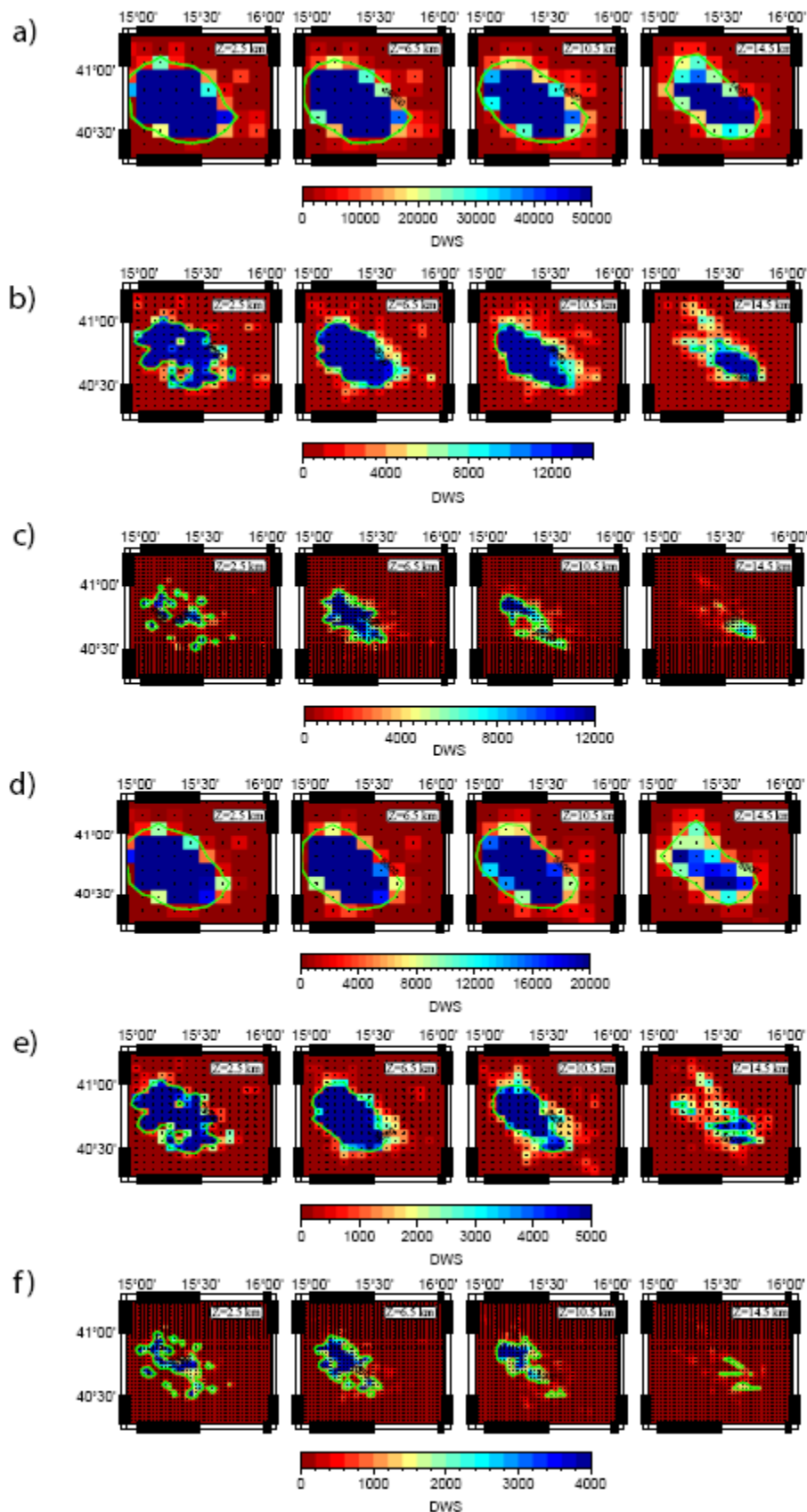


Figure 27. Plot of the Derivative Weight Sum (DWS). The DWS values in a, b, d and e show that the 3 D Q_P and Q_S models are well resolved from 2.5 to 14.5 km depth for the first and second parameterization ($12 \times 12 \times 4$ km³ and $6 \times 6 \times 2$ km³, respectively) while for the more refined parameterization ($3 \times 3 \times 1$ km³) figures c and f show that the well-resolved area is less extended and ranges from 2.5 km to 10.5 km depth.

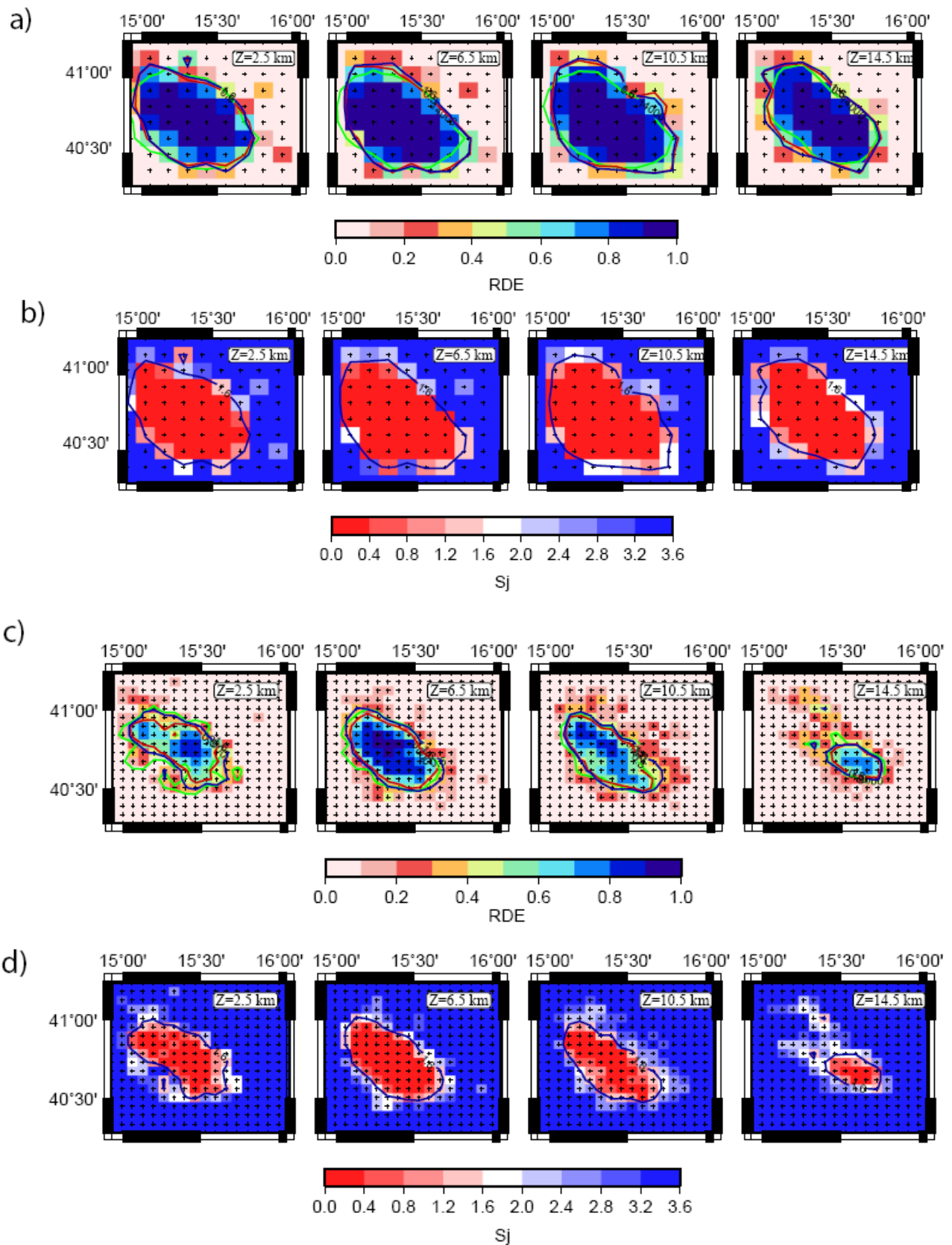


Figure 28. Resolution matrix for Q_p models. a) and b) Map view showing the RDE and Sj (Michelini and McEvilly, 1991) for parametrization $12 \times 12 \times 4$ km³. c) and d) same as a) and b) for parametrization $6 \times 6 \times 2$ km³.

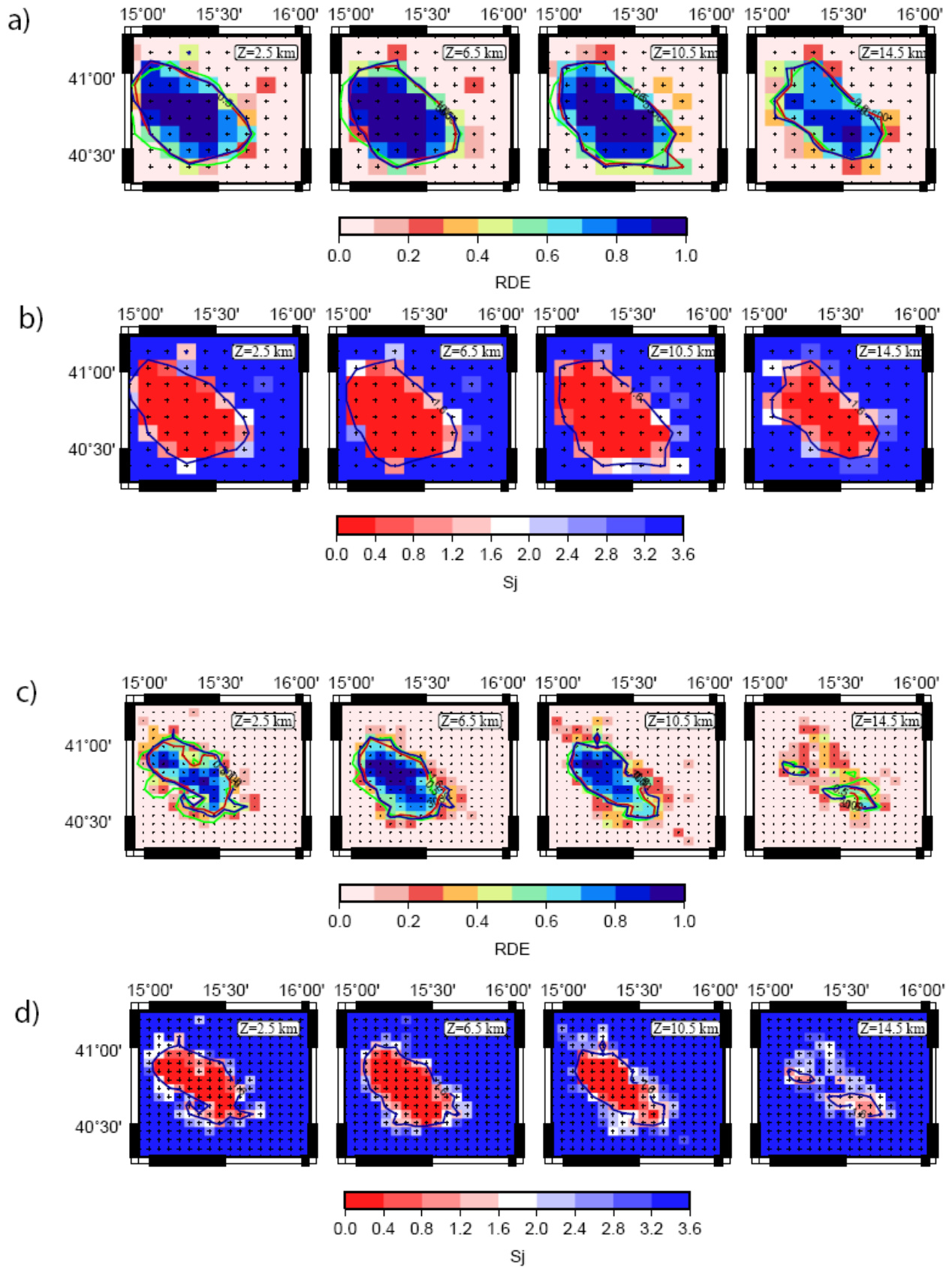


Figure 29. Resolution matrix for Q_s models. a) and b) Map view showing the RDE and Sj (Michelini and McEvelly, 1991) for parametrization $12 \times 12 \times 4$ km³. c) and d) same as a) and b) for parametrization $6 \times 6 \times 2$ km³.

1.5.4 Discussion

The results obtained from the tomographic inversion of the attenuation parameter, t^* , for the P and S waves, have allowed us to provide a highly detailed three-dimensional image of the attenuation quality factors for the whole studied area, in particular of the crustal volume embedding the Irpinia fault system zone.

From the methodological point of view, we implemented a new attenuation tomography method and verified that the use of a multiscale inversion strategy allows to optimize the search for the best fit attenuation factors Q_P and Q_S : this strategy improves the model parameter resolution images (Fig. 27, 28 and 29). The factor Q_P is related to the high-frequency component of the wave signals and, therefore, is sensitive to the small wavelength content and related spatial variations of the attenuation properties in the propagating medium.

In the investigated crustal portion, the attenuation tomography images show relatively high Q_P values in correspondence of the 1980 Irpinia earthquake fault zone, at depths ranging from 8 to 12 km, where the first rupture episode nucleated (Bernard and Zollo, 1989). On the other hand, Q_S : appears more sensitive to large wavelength scale variations, by showing a good correlation with the surface lithology and geological structures. In particular the Q_S : tomographic images between 6 and 12 km depth (Fig. 26a, 26b) display a main structural discontinuity along a SW-NE oriented section (i.e. normal to the strike of the Apennine belt) that roughly corresponds to the 1980 earthquake rupture and the north-eastern edge of the uplifted pre-Tertiary limestone. This feature coincides with the similar NW-SE trending lateral velocity discontinuity previously revealed by Amato et al. (1992) (recently confirmed by Amoroso et al. (2014), and Improta et al. (2014)) affecting the shallow upper crustal volume across the Irpinia earthquake fault zone. This discontinuity can be associated with the contrast between the thick cover of low-velocity, high attenuation Miocene basin sediments to the NE and the high-velocity, low-attenuation carbonate outcrops of the Apennine Platform to the SW (Ascione et al., 2013). At greater depths, this marked contrast is provided by the Apulian Platform carbonates being uplifted in the hanging-wall of a basement-involved reverse fault (extensionally reactivated as the NEBF during the late Quaternary) and juxtaposed to the Lagonegro basin strata and overlying Miocene units (Ascione et al., 2013).

1.6 Rock physics modelling

We now consider another inverse problem where the retrieved seismic velocities and attenuations (macro-parameters) are our input data-set. From these observables, we would like to recover the properties of the host rock volume characterized by a set of micro-parameters (porosity, consolidation parameter, permeating fluid type and percentage of fluid saturation), which describe the hydrological properties of the solid and bi-phasic fluid components. We do this by an exhaustive sampling of micro-parameters for a prediction of macro-parameters resulting from an up-scaling strategy. This procedure relies on the rock model developed by Pride (2005), based on the Biot's (1962) theory of poroelasticity (Dupuy et al., 2016) and Gassmann's relation (1951). A more detailed discussion of the methodology can be found in the chapter 1.3.1 of PART I. The following work was insert in the conference paper De Landro et al. 2016, presented at the *European Seismological Commission 35th General Assembly*, Vienna 2016.

1.6.1 Inversion strategy and comparison with attenuation images

We focused our rock physics modelling on the volume embedding the Irpinia fault system between 8 and 10 km depth, where the quality factor Q_p ranges between 350 and 850 (median value 690) (see Fig. 26c) and where most of seismicity occurs. By direct comparison between the up-scaled values of the theoretical macro-parameters values and those inferred from the velocity and attenuation tomography, we retrieve the micro-parameters for the area enclosed within the South West (SWBF) and North East (NEBF) boundary faults (Fig. 13b). For this, we needed to restrict the number of poroelastic parameters by assuming the lithology of the host rock, the range of variability for porosity and consolidation parameters, and the type of fluids to include in the modelling.

Cross-Appennine seismic profiles (Mostardini and Merlini, 2004) indicate that the investigated depth range is host to - for the most part- the lower Apulian platform and, for a smaller thickness, the clastic sediments and the basement. The three oil wells drilled in the considered area (Contursi, San Gregorio Magno, San Fele; see Fig. 13b) did not reach the lower part of the Apulia Carbonate Platform. However, two deep boreholes, drilled for oil exploration in the Apulia region, i.e., the Gargano-1 and Puglia-1 wells (available from the ViDEPI Project at <http://unmig.sviluppoeconomico.gov.it/videpi/pozzi/pozzi.asp>), indicate that the lower part of the Apulia Carbonate Platform is mainly formed of dolostones. Therefore, we used dolomite as the dominant mineral component for our rock physical modelling.

In the Puglia-1 well, porosity values ranging between 0.87% and 2.53% have been measured in the dolostones of the Burano Formation at 5 km depth. Another core taken at 6 km depth in alternating dolostones and anhydrites provided a porosity range of 0.70-1.37% (the data of the Puglia 1 well are available at http://unmig.sviluppoeconomico.gov.it/deposito/pozzi/profilo/pdf/puglia_001.pdf). Larger values of porosity have been reported for carbonate reservoirs (limestones and dolostones) in the same depth interval. The modal value of average porosity at a depth of 5.25-5.75 km in the huge dataset of Ehrenberg and Nadeau (2005) is 6.2%. For greater depths, the empirical relation of Schmoker and Halley (1982) can be used to predict a porosity of 3.5% for dolostone at a depth of 8 km. Most of the porosity values used for the previously cited studies are derived from core measurements or well log analyses. The total porosity at the scale considered for our rock physics modelling might be significantly higher due to the likely presence of a dense network of fractures (Amoroso et al., 2014). For this reason, the explored range of porosity was extended up to 5% in the inversion process.

According to Pride (2003), C_s values range from 2 to 20 in sandstones. de Ceia et al. (2015) estimated C_s for a set of microporous carbonate rocks and showed that its values fall, for the most part, within the range indicated for sandstone. Lee (2005) concluded that, in practice, C_s could be viewed as a free parameter to fit the data if both porosity and P- and S-wave velocities are known. Therefore, in the up-scaling procedure we explored the entire (2, 20) range for C_s , expecting that the comparison with the retrieved macro-parameters would allow the C_s micro-parameter values to be better constrained.

We hypothesize that the fluids permeating the rocks at the investigated depths are brine, CO_2 , and CH_4 based on recent measurements of gas emission at surface (Inversi et al., 2013; Chiodini et al., 2004; Ciotoli et al., 2014). We excluded the steam phase since brine can only exist in the liquid phase at temperature and pressure conditions within the considered depth range. Similarly, we did not consider oil as a plausible permeating fluid since only very minor impregnations have been found in the San Gregorio Magno well (as it results from the ViDEPI Project <http://unmig.sviluppoeconomico.gov.it/videpi/pozzi/pozzi.asp>).

Gassmann's relation requires that the shear modulus of the saturated rock be the same as that of the dry rock. However, Adam et al. (2006) showed that the shear modulus, which is linked to Q_s , decreases in water-saturated rock samples, so the assumption that it is independent of the fluid substitution may not be valid for carbonate rocks in the range of seismic frequencies. Instead, the bulk modulus, which is linked to Q_p , is well predicted by the Gassmann's relations

we adopted; therefore, we did not consider the Q_s parameter for the rock physics interpretation.

In summary, we assumed that the simulated rock has a dominant dolomite mineralogical composition, a porosity in the range (1%, 5%), and C_s in (2, 20), and we considered pores and fractures filled by a two-phase fluid (brine- CO_2 ; brine- CH_4 and CO_2 - CH_4). We then computed the values of the macro-parameters (V_p , V_s and Q_p) by varying the relative saturation percentage and compared them to the observed values.

In order to obtain information on micro-parameters of the rocks and most likely fluids mixing starting from the tomographic images, we compared the observed macro-parameters with those calculated using the up-scaling procedure previously described.

We adopted the criterion for which the optimal set of micro-parameters is the one for which the resulting macro-parameters curves fall within the range of the observed values. We also determined the range of retrieved macro-parameters through the analysis of the statistical distributions of velocity and attenuation in the considered volume. We selected the macro-parameter values (V_p , V_s , V_p/V_s and Q_p) falling within the volume bounded SW and NE by Boundary faults, as indicated in Fig. 2, and extending north for about 10 km. The limiting values for macro-parameters are those for which the cumulative frequency ranged between 15% and 85%.

By varying the fluid mixing and porosity, we explored the macro-parameter curves in respect of the observed values range and discarded the curves of predicted macro-parameters that did not fall within the observed ranges for any combination of the micro-parameters.

From table 2 we infer a porosity range of 3% to 5% and a consolidation parameter between 6% and 10% for the host rock. All the considered fluid combinations are likely at 8-10 km depth with a different combination of porosity, C_s , and the relative percentage of saturation (Fig. 30). The saturation range of different fluid combinations is described in Fig. 3d, which shows the relative fluid saturation varying with C_s values.

The inferred relative fluid saturation percentage varies with the porosity and C_s , and it does not allow us to discriminate whether one of the two fluids has a dominant saturation percentage in the explored rock volume. However, whereas for CO_2 - CH_4 the range of saturation is independent from C_s (grey line in Fig. 30d), for the other two fluid combinations (blue and green lines), with increasing C_s the saturation goes from values indicating the predominance of one fluid with respect to the other, to values indicating a more balanced mixing. Finally, the up-scaled V_p/V_s ratio falls always within the range of the retrieved value, slightly increasing with saturation, for all the porosity and C_s values. This ratio appears weakly sensitive to the type of fluid combination (Fig. 30a-d).

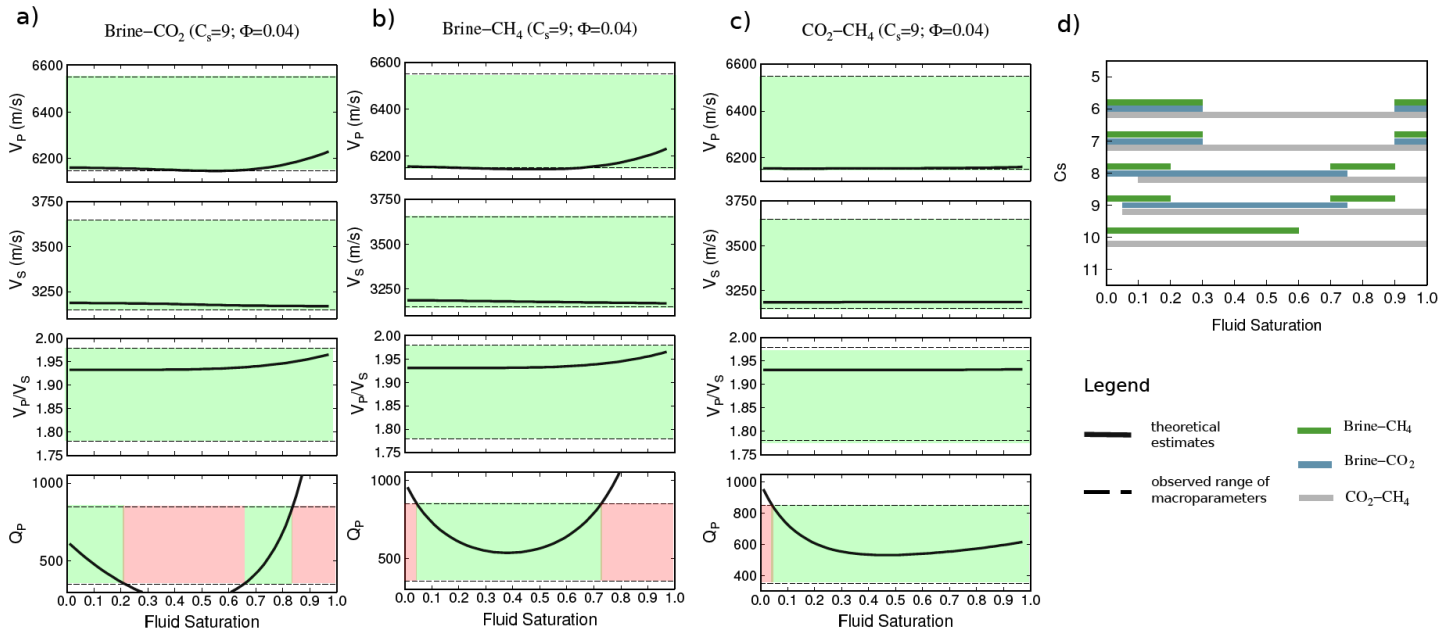


Figure 30. Up-scaling results. (a) (b) (c) Macro-parameters derived from up-scaling procedure as a function of relative fluid saturation (fluid couple reported in title, percentage of the first fluid phase respect to the second) for the three tested fluid couples and different combinations of ϕ and C_s . For each panel the black dashed lines delimit the range of the retrieved values from the tomographic images for each macro-parameter. The ranges are green when the up-scaled curves fall inside the retrieved range, while they are red otherwise. (d) Saturation ranges for which the up-scaled curves, relative to the three fluid couples, fall inside the retrieved range by varying C_s . Porosity is fixed to 0.04.

Cs	5				6				7				8				9				10				11							
	2	3	4	5	2	3	4	5	2	3	4	5	2	3	4	5	2	3	4	5	2	3	4	5	2	3	4	5				
$\Phi (x10^{-2})$	2	3	4	5	2	3	4	5	2	3	4	5	2	3	4	5	2	3	4	5	2	3	4	5	2	3	4	5	2	3	4	5
V_p	x	x	x	x	x	x	x	✓	x	✓	✓	✓	x	✓	✓	x	x	✓	✓	x	x	✓	✓	x	x	x	x	x				
V_s	x	✓	✓	✓	x	✓	✓	✓	x	✓	✓	✓	x	✓	✓	x	x	✓	✓	x	x	✓	✓	x	x	x	x	x				
V_p/V_s	✓	✓	✓	✓	✓	✓	✓	✓	✓	✓	✓	✓	✓	✓	✓	✓	✓	✓	✓	✓	✓	✓	✓	✓	✓	✓	✓	✓				
Q_p	-	-	-	-	-	-	-	✓	-	✓	✓	✓	-	✓	✓	-	-	✓	✓	-	-	✓	✓	-	-	-	-	-				

Table 2. Summary of the results obtained from the comparison between the up-scaled macro-parameters curves and the retrieved macro-parameters ranges. The checkmark indicates that all up-scaled macro-parameters curves fall in the retrieved range, otherwise a cross is present. The dash indicates that the value is not reported because the velocity curve falls outside the retrieved range.

1.7 Conclusion

The strong lateral SW-NE variation of Q_s coincides with the NW-SE trending lateral velocity discontinuity previously revealed by Amato et al. (1992) and recently confirmed by Amoroso et al. (2014) and Improta et al. (2014), affecting the shallow upper crustal volume across the Irpinia earthquake fault zone. This discontinuity can be associated with the contrast between the thick cover of low-velocity, high attenuation Miocene basin sediments to the NE and the high-velocity, low-attenuation carbonate outcrops of the Apennine Platform to the SW (Ascione et al., 2013). This result suggests that jointly mapping Q_s seismic velocities in 3D allows the geometrical features of large-scale geological structures and lithological transitions to be better constrained. On the other hand, due to its specific high-frequency content, Q_p detects the smaller wavelength spatial variation, e.g. the finer structure of the 1980 Irpinia earthquake in the considered analysis.

The retrieved values of V_p and V_s are needed to constrain the range of average, rock volume porosity, but their curves for different fluid combinations, keeping porosity and C_s fixed, have the same trend and all fall within the range of the retrieved values (Fig. 3a-c). This means that V_p , V_s and their ratio alone cannot discriminate between the type and different combinations of fluid phases within the uncertainties of the observed macro-parameters and modelling. On the other hand, the attenuation macro-parameter Q_p provides a stronger constraint on rock physical micro-parameters, allowing us to reject the fluid mixings that exhibit up-scaled theoretical values well outside the uncertainty bounds.

The host rock was modelled with the dolomite as single mineral component. The consistency of the results with independent observations (well logs, measures of gas at the Earth's surface) leads us to conclude that the approximation of a single mineral rock composition is reliable for our purposes.

The determined porosity range of 3 to 5 % at a depth of 8-10 km is larger than that measured from borehole rock samples (1-2%). This can be justified by assuming a significantly contribution of a densely fractured system to the porosity at the meso-scale as proposed by De Matteis et al. (2012) and Amoroso et al. (2014).

de Ceia et al. (2015) retrieved a relation between the consolidation parameter, C_s , and effective pressure through indirect measurements on carbonate rock samples. They found that C_s decreased as the effective pressure increased. By using this relation and considering a standard gradient for the overburden pressure, we found that at 8-10 km depth our C_s values correspond to a pore pressure of up to about 150 MPa. These inferred pore pressure values

are significantly high and support the hypothesis of seismic fracture generation driven by pore pressure changes in the fault zone.

As for the possible fluid mixes, both brine-gas and gas-gas (with gases being CO₂ and CH₄) are compatible with observed micro-parameters, thus supporting the hypothetical presence of gasses CO₂ or CH₄ at the explored depth range. We suggest that these gasses, when observed at the surface, may be trapped just below and/or in the lower part of the Apulian Platform, within dolostones sealed by anhydrite levels (Trippetta et al., 2013), fed by fluid-rich mantle melts intruded into the crust (e.g. Improta et al., 2014).

The presence of liquid and gas fluid phases in a fault volume and the inferred high pore pressure values have important consequences on seismicity generation. In fact, the presence of fluid inside the fault gauge may enhance seismicity due to lubrication mechanisms, and by an increase of pore pressure in the medium embedding the faults. In the Irpinia fault zone, the modelling of micro-earthquake spectra has provided a rather low average seismic radiation efficiency (Zollo et al., 2014), thus implying that the rupture lubrication mechanisms are not favoured. Therefore, we suggest that the dominant mechanism triggering the micro-seismicity at the Irpinia fault zone is the pore pressure increment induced by fluid diffusion in the host rock medium (Dvorkin et al., 2000; Shapiro et al., 2003; Vanorio et al., 2005). When rocks are close to a critical state of failure, a perturbation of the pore pressure, modifying the effective normal stress, can lead to the occurrence of a seismic fracture (Nur and Booker, 1972). In particular, at the considered depths, gasses more than liquids may significantly increase the pore pressure up to a level for which it equals the lithostatic pressure (Hantschel and Kauerauf, 2009). The results of the up-scaling procedure, especially in terms of C_s , allow us to interpret the investigated volume at 8-10 km depth as highly fractured and liquid-gas saturated, where the high pore pressure is directly responsible for the seismicity triggering mechanism and where, in fact, most of seismicity occurs.

Chapter 2 : *THE GEYSERS geothermal field*

2. Introduction and state of the art

Geothermal systems have the potential to provide a significant contribution to the world energy demand. These are naturally or artificially fractured hydrothermal systems providing accessible sources to extract the heat stored in subsurface rocks, which may be directly used for heating purposes or to generate electricity. The total resources and their availability tend to be restricted to certain areas, and the development of the field only proceeds where the conditions are ideal for cost-efficient extraction. Such hydrothermal systems are sometimes difficult to locate and also run a high risk of not being commercially feasible, if their geological, physical and chemical characteristics are not favourable. In that case the underground heat source requires enhancement (e.g., Nielson et al., 2001). The reason for developing the Enhanced Geothermal Systems (EGS, Fig. 31) is two-fold. It aims: (1) to bring uneconomic hydrothermal systems into production by improving their underground conditions (hydraulic fracturing, reservoir stimulation); and (2) to engineer an underground condition that creates a new fracture-network system, where injected fluids are heated by circulation through hot fractured rock at depth. The hot fluid or steam is then brought to the surface, in order to deliver the captured heat for power conversion and other uses. The second approach significantly expands the available heat resources and reduces the uncertainty of exploitation costs.

However, fluid injection, steam extraction, and reservoir stimulation in EGS lead to induced seismicity. In particular, the mechanisms triggering seismicity are the increase of pore-pressure induced by fluid diffusion, the thermal cracks due to the difference in temperature between hot rock and injected water, and the chemical alteration of the fault surface. Although, on the one hand, only in rare cases the induced events may be large enough to pose a hazard to the population or to the installed facilities, on the other hand the micro-seismicity provides valuable information on the extent and properties of the reservoir (e.g., Eberhart-Phillips and Oppenheimer, 1984; Stark, 2003). Therefore, micro-seismic monitoring is important both for the mitigation of the unwanted effects of industrial operations and for the continuous assessment of the reservoir conditions.

The controversial issue of induced seismicity in EGS has attracted seismological research. Although induced seismicity has in fact few adverse physical effects on operations or on surrounding communities, public concern over the amount and magnitude of the seismicity associated with current and future EGS operations still remains.

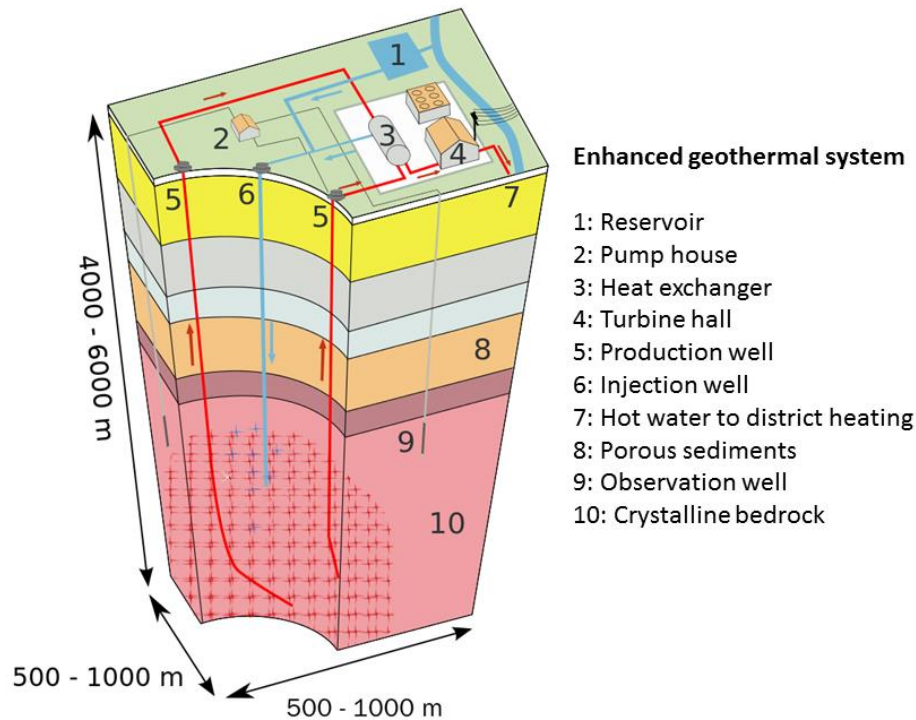


Figure 31. Sketch of an enhanced geothermal system. The injection (6) and production (5) wells go down across the reservoir stratigraphy to the crystalline bedrock. In this layer the mainly mechanisms that trigger seismicity are the pore-pressure increase induced by fluid diffusion and the thermal cracks due to temperature difference, between hot rock and injected water.

In order to better understand induced seismicity and the reservoirs in which it occurs, we applied a set of different seismological analyses to a high-quality seismic data-set collected at The Geysers geothermal field, located about 120 km north of San Francisco, California. The Geysers geothermal area is the largest enhanced geothermal system (EGS) in the world.

The Geysers is a vapor-dominated field, which presents the top of the main steam reservoir at about 1-3 km below the surface. The field has been actively exploited since the 1960's and is now the most productive geothermal field in the world (Bertani, 2012). With the increasing field development, seismicity also increased in the area (e.g., Majer et al., 2007, Majer and Peterson, 2007). As reported, for example, by Stark (2003), the dominant mechanism of the generation of induced seismicity at The Geysers EGS is the temperature contrast between the injected water and the hotter rock-fracture surfaces. In fact, most of the heat is thought to be

stored in the rock matrix and not in liquid pore-water in the reservoir. The water flows out of the pores and flashes to steam in the bore holes during extraction.

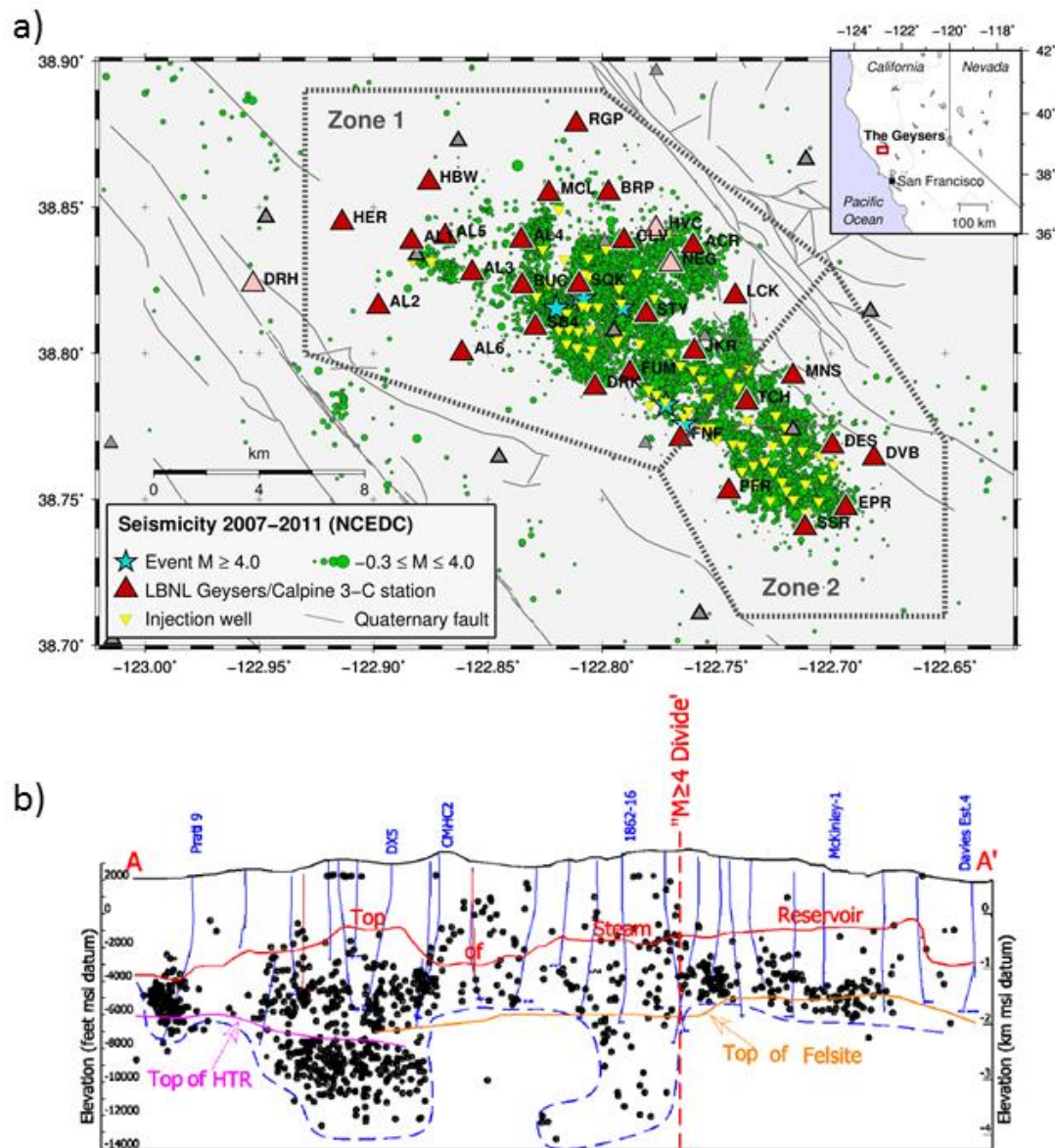


Figure 32. a) Distribution of induced seismicity recorded at The Geysers. Black triangles indicate the seismic stations of the Lawrence Berkeley National Laboratory (LBNL) Geysers/Calpine seismic network used in this study, and grey triangles are additional stations from the Northern California Seismic Network (NCSN) in the region. (from Convertito et al., 2012). b) Main geothermal and geological features of the reservoir. The red solid line indicates the top of the steam reservoir, the orange line the top of the felsite, and the pink line corresponds to the top of the high temperature reservoir (HTR), as reported by Beall and Wright (2010) (from Beall and Wright 2010).

The Geysers area can be divided into two distinct seismicity source zones which are outlined by the dashed lines shown in Fig. 31a and here named ZONE1 and ZONE2. The separation arguments are supported by Stark (2003), Beall and Wright (2010). Some differences in the seismicity distribution were also noted by Eberhart-Phillips and Oppenheimer (1984). All the authors observed that the south-eastern part of the Geysers reservoir is seismically less active

than the north-western where seismicity extends to greater depth. The differences were basically ascribed to a depth variation in the high-temperature (260–360° C) vapor-dominated reservoir. Specifically, Beall and Wright (2010) identified a net “*M*>4 *dividing zone*” which separates the whole area into two seismically different zones. In fact, the north-western area (ZONE1) contains all the earthquakes having magnitude larger than 4.0, whereas the south-eastern one (ZONE2) is characterized by lower magnitude events. Further supporting arguments were more recently brought by Convertito et al. (2012) who also distinguished two different zones in the Geysers area from the analysis of the b-values of the Gutenberg-Richter relationship based on the Utsu (1992) test.

McNitt et al. (1989) compiled the results of several hundred lithologic logs for The Geysers region to develop a model of the stratigraphy. They concluded that the steam reservoir is contained in a highly indurated and fractured graywacke that is capped with a more ductile, unfractured argillaceous graywacke. The graywacke sequence has been intruded at its base by silicic magmas to form a felsite batholith whose axis trends northwest and is roughly coincident with the steam field (Thompson and Gunderson, 1992). The elevations of the top of the steam reservoir before production and of the top of the felsite intrusive body have recently been made public by a consortium of Geysers operators (Field Operators, 1992).

The Fig. 31b shows the main geothermal and geological features characterizing the reservoir as reported by Beall and Wright (2010). In particular, in ZONE1 the normal steam dominated reservoir (at temperature ~240°C) is underlined by a high temperature steam dominated reservoir (HTR) at 260-360 °C . The top of the steam reservoir is located at about 1 km depth. The top of felsite, a granitic intrusion, underlines much of the steam reservoir and is shallower in ZONE2 compared to ZONE1. Coincidence of the “*M*>4 *dividing zone*” boundary for reservoir characteristics as disparate as earthquake magnitude distribution and earthquake depth may indicate that this dividing zone represents the south-eastern boundary of the HTR (Beall and Wright, 2010).

In the geysers geothermal region induced seismicity since 1965 (roughly the date of significant production at The Geysers) is given in Fig. 33, which reveals that the seismicity below magnitude 3.0 has increased significantly over the years. The steam production and seismicity trends clearly diverge after additional source of water were used for injection, starting in 1980's. The level of seismicity (magnitude $M > 1.5$) has shown positive correlation with steam production. Also, the “injection” chart is scaled such that the injection and seismicity values, at the time of the injection peak in 1998, plot more or less together. Majer et

al. (2007) have noticed that the injection and seismicity plots are very similar for every year thereafter, as well as being quite similar for all the years previous to 1998. This findings clearly indicates a remarkably strong correlation of seismicity with injection. These data seem to confirm that shallow and deep induced micro earthquakes occurring after the 1980 are correlated to local injection rates, after a certain time lag. (Stark, 1992; Stark, 2003). For example, Stark (1992) showed that plumes of micro-earthquakes are clustered around many injection wells, and the seismic activity around each of these wells correlates with its injection rate.

Seismic Monitoring Advisory Committee Meeting

Yearly Field-wide Steam Production, Water Injection and Seismicity
Starting 1960; Projected Through End 2014 *

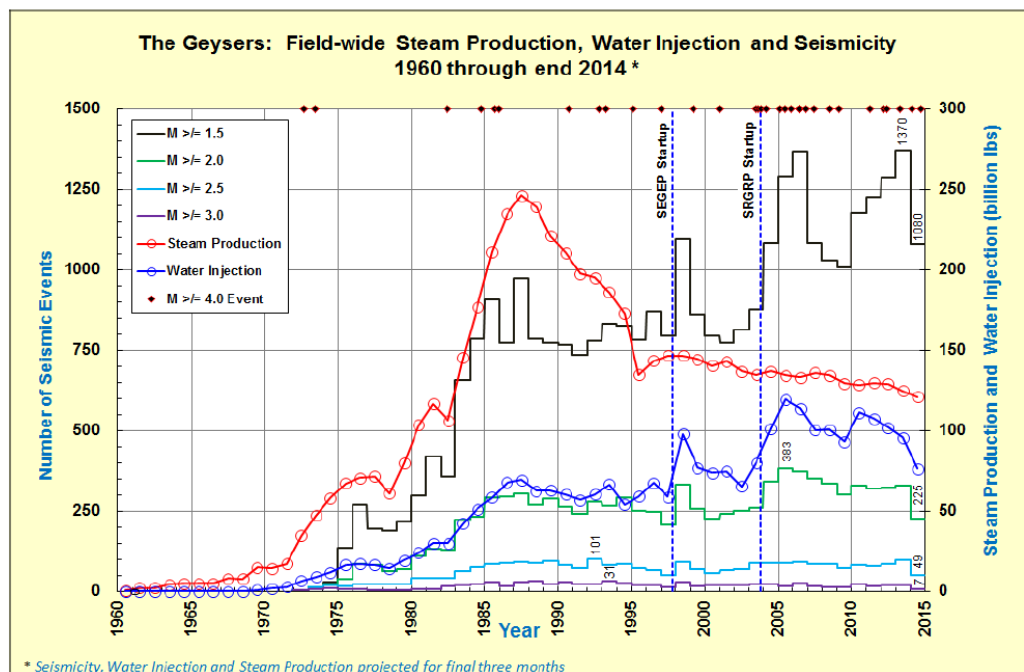


Figure 33. Correlation between induced seismicity and injection rates. The Geysers annual steam production (red line) plotted with the earthquake activity, and water injection (blue line). Also shown are the $M > 4$ events (red dots at top of chart). The entire seismic events catalogue analysis (Fig. 33) shows the correlation between volume of injected water and rate of seismicity occurrence with low magnitude ($M > 1.5$). The correlations between steam extraction and seismicity with higher magnitude are not so evident. (from Seismic Monitoring Advisory Committee).

Several studies have performed a three-dimensional block inversion for P-wave and S-wave velocity structure for The Geysers (Majer and McEvilly, 1979; Gupta, *et al.*, 1982; Eberhart-Phillips and Oppenheimer, 1984; Eberhart-Phillips, 1986; and O'Connell and Johnson, 1991; Zucca *et al.*, 2011). Kirkpatrick *et al.* (1997) conducted three-dimensional V_p and V_s inversions for the same portion of The Geysers area as the one studied here. The interpretation is complicated by the transition from metagreywacke-dominated to felsite-dominated matrix as depth increases. However, they found that high V_p values correlated with high V_s , while low V_p correlated with low V_s in the metagreywacke. Effective medium

theories would suggest that low V_p and V_s indicate highly fractured regions, while high V_p and V_s may indicate un-fractured regions. At greater depths Kirkpatrick et al. found positive correlation between high V_p/V_s and high V_p , which are thought to coincide with the felsite.

In a most recent work, Zucca et al., (2011) obtained a 3D P-wave velocity model that goes down to 1.5 km depth by inverting the compressional-wave arrival times of about 300 earthquakes. The authors found that the velocity structure correlates with known mapped geological units. The reservoir appears to exhibit low velocity compared to the surrounding country rock. The dry steam reservoir, which is known from the steam well drilling, is mostly correlated with low velocity. The correlation is best for those areas where the steam pressure has been reduced by production.

Gritto et al., (2014) analysed temporal changes in the V_p/V_s ratio and average seismic P- and S-wave velocities (V_p and V_s , respectively) throughout the entire reservoir from 2004 to 2011, with a data-base of about 100.000 events. The V_p/V_s ratio was calculated by applying the Wadati technique (Wadati, 1928; par.) and the average V_p and V_s values were calculated as the inverse slope of travel-time curves vs. ray length. The authors found that the temporal variations in the V_p/V_s ratio reveal a high correlation to the total volume of injected water throughout the entire reservoir.

Finally, Gunasekera et al. (2003) performed a four-dimensional seismic tomography by considering five different months between 1991 and 1998. For each epoch, tomographic inversions were performed for the three-dimensional V_p and V_p/V_s structure of the reservoir. The results show an extensive low- V_p/V_s anomaly occupying the reservoir, which grew in strength from a minimum of 9% to a maximum of 13.4% during the 7-year study period. This is attributed to the depletion of pore liquid water in the reservoir and its replacement with steam. Variations in the V_p and V_s fields indicate that water depletion is the dominant process in the central part of the exploited reservoir, and pressure reduction and mineral drying are the dominant processes in the northwest and southeast parts of the reservoir.

All the discussed works show how the continuous monitoring of V_p , V_s , and V_p/V_s is an effective geothermal depletion-monitoring tool for the reservoir, and how it can provide information about the reservoir conditions.

2.1 Seismic network and data

Different temporary and long-term seismic networks have been deployed in The Geysers geothermal field during the last five decades to monitor the seismic activity. At present, local

seismicity is monitored by the dense Lawrence Berkeley National Laboratory Geysers/Calpine (BG) surface seismic network and by some nearby stations of the Northern California Seismic Network (NCSN). The BG network consists of 32 three-component stations, 29 of which were used for the present study (red triangles in Fig. 32a). The BG stations are distributed over an area of about $20 \times 10 \text{ km}^2$, which covers the entire geothermal field. Each station was equipped with I/O Sensor SM-6 geophones with a natural frequency of 14 Hz. In the fall of 2009 these instruments were replaced by Oyo GS-11D 4.5 Hz sensors. For the present studies we compiled a waveform database of 15476 events recorded at the BG stations between 2007/07/24 and 2011/10/30, and associated with earthquakes in the catalogue of the Northern California Earthquake Data Center (NCEDC). We only selected the events with at least 20 high-quality P-wave picks, thus reaching a total of 1320 events.

2.2 3D P and S velocity models

Although different 3D tomographic models for the area already exist, our aim is to obtain P- and S-wave velocity tomographic models with an un-precedent spatial resolution (1 km in horizontal and 0.5 km in depth) and down to 5 km depth.

The obtained velocity models are inserted in the paper Amoroso et al. (2017), submitted in the special Issue "Modern methods of Applied Geophysics to the understanding of volcanic structures and dynamics" of the Journal of Applied Geophysics and in a poster at the AGIS workshop on induced seismicity (Davos, 2015).

The 3D P- and S-wave velocity model is obtained from the tomographic inversion (see par. 1.1.1) of the first P- and S-wave arrival times. The selected stations and the distribution of events allowed us to investigate a volume of $36 \times 25 \times 5 \text{ km}^3$. The velocity model is parametrized by a trilinear interpolation on a tri-dimensional grid with a node spacing of $1 \times 1 \times 0.5 \text{ km}^3$. The inversion starts from the 1D velocity model, optimized for the area, which is also used for the initial earthquake locations (Emolo et al., 2012). The misfit function, defined as the sum of the squared time delays (RMS), is analysed *a posteriori* to check the convergence, which is reached after 8 iterations (Fig. 34) and where the final RMS value is equal to 0.1 s, with an RMS reduction of 50%.

The damping value has been selected on the basis of an empirical approach: we performed several one-step inversions with different damping values for each data-set.

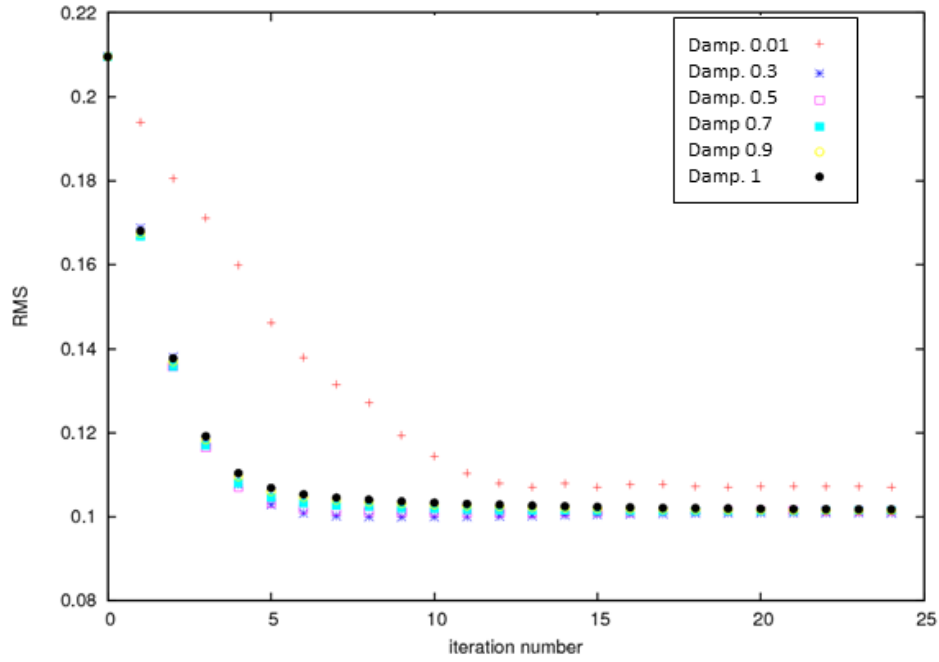


Figure 34. RMS curves in function of iteration number. The different symbols represent the curves corresponding to inversion with different damping values, as indicated in the legend.

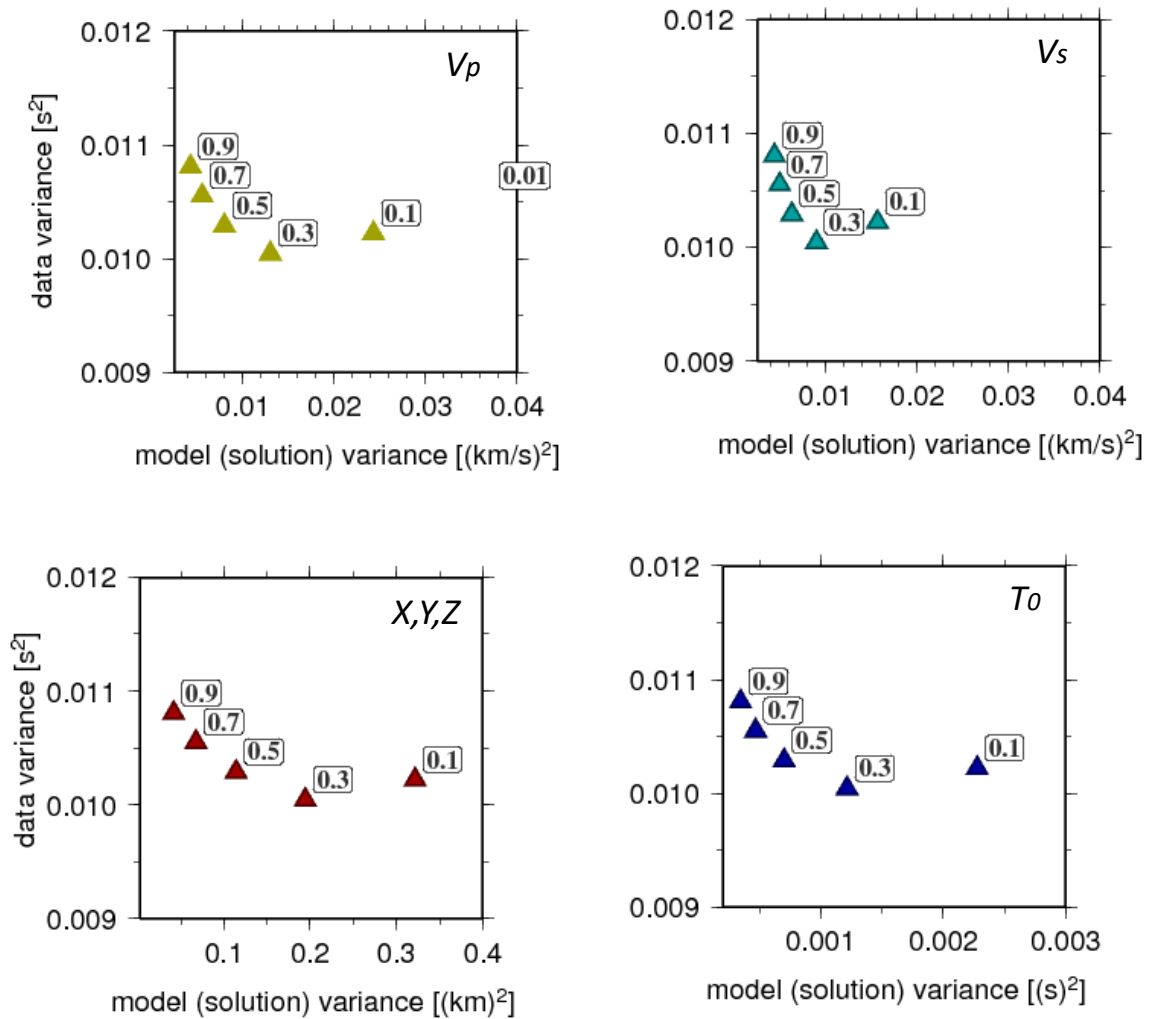


Figure 35. Trade-off curve for selecting optimal value for real data-set. The data variance and solution variance are computed after one iteration for indicated damping values.

Then, the reduction in the variance of data is compared to the variance of the solution. The selected value is 0.3, i.e. the one which greatly reduced the variance of data with a moderate increase in the solution variance (Fig. 35). In order to determine the optimal combination of hyper-parameters, we performed a sensitivity test, i.e. synthetic tests using the real earthquake-station configuration and the same parameters as the ones chosen for the tomographic inversions. Synthetic P and S velocity models are the ones obtained at the third iteration, i.e. simple 3D models that only contain the predominant characteristics of 3D final models. Theoretical travel times are computed in these models and used as observed times. The 1D initial P- and S-wave models are considered as initial models and the earthquakes are relocated to obtain an initial hypocentre location.

We performed several inversions for several combinations of hyper-parameters, and, by observing the evolution of the difference between the obtained final model and the true model in function of the number of iterations, we chose the combination of parameters for which the trend of this curve is simultaneously convergent for all the four classes. In Fig. 36 the curves represents the variance in function of the iteration number for five different combinations of hyper-parameters, C_p , C_s , C_{p0} and C_{T0} . The selected values, represented by the red line, are $C_p=1$, $C_s=1$, $C_{p0}=1$ and $C_{T0}=1$.

In Fig. 37a and b we show the results of the tomographic inversion performed with the previously explained choice of parameters. The resolved area is evaluated by using the DWS (see par. 1.1.1.2). In particular, in Fig. 37 and 38, the solid white contour lines identify the model regions where the derivative weight sum (DWS) is greater than 5000.

The tomographic P-wave model, represented in Fig. 37a, shows an increase in velocity with depth ranging from 3.6 to 6.3 km/s. Moreover, down to 2 km, there is a small area in the North-West characterized by velocity values which are smaller than the ones in the surroundings. The P-wave velocity values are in agreement with the geological composition of the reservoir. In fact, Berge and Wagoner (2001), who considered laboratory measurements on rock samples and approximated the reservoir as being homogeneous in mineral composition, expected low velocities near the surface, which increased with depth up to the values observed in the lab on intact samples, that is, 5.5 - 5.7 km/s.

The tomographic S-wave model, represented in Fig. 37 b, can be divided into two zones characterized by different velocity trends down to 3 km depth. In particular, the zone located in the North-West shows lower velocity values than those of the South-East zone. At greater depths this trend is not visible, but the resolution significantly decreases.

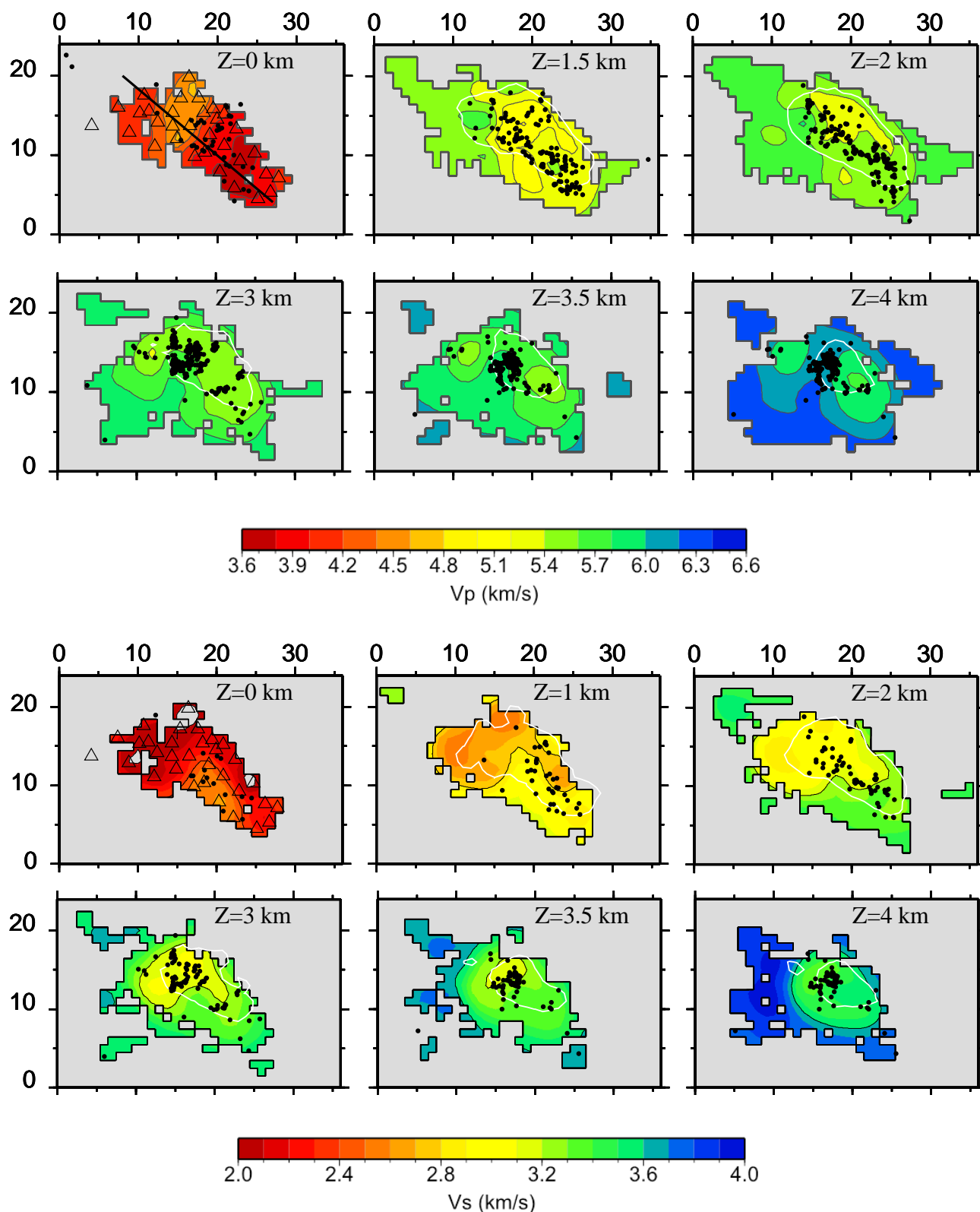


Figure 34. P and S-wave velocity models. Top, map view of P-wave velocity model at 0, 1.5, 2, 3, 3.5 and 4 km depth from 3D travel time tomography. The seismic stations are shown at 0 km depth layers as open triangles, whereas black dots in all panels represent the earthquake location. Regions not covered by ray-paths are in grey. The solid white contour lines identify the model regions where derivative weight sum (DWS) is greater than 5000. The images indicate the presence of a strong lateral variation of seismic velocity along the NW-SE direction. Bottom, map view of S-wave velocity model at 0, 1, 2, 3, 3.5 and 4 km depth. Again, the images indicate the presence of a strong lateral variation of seismic velocity along the NW-SE direction.

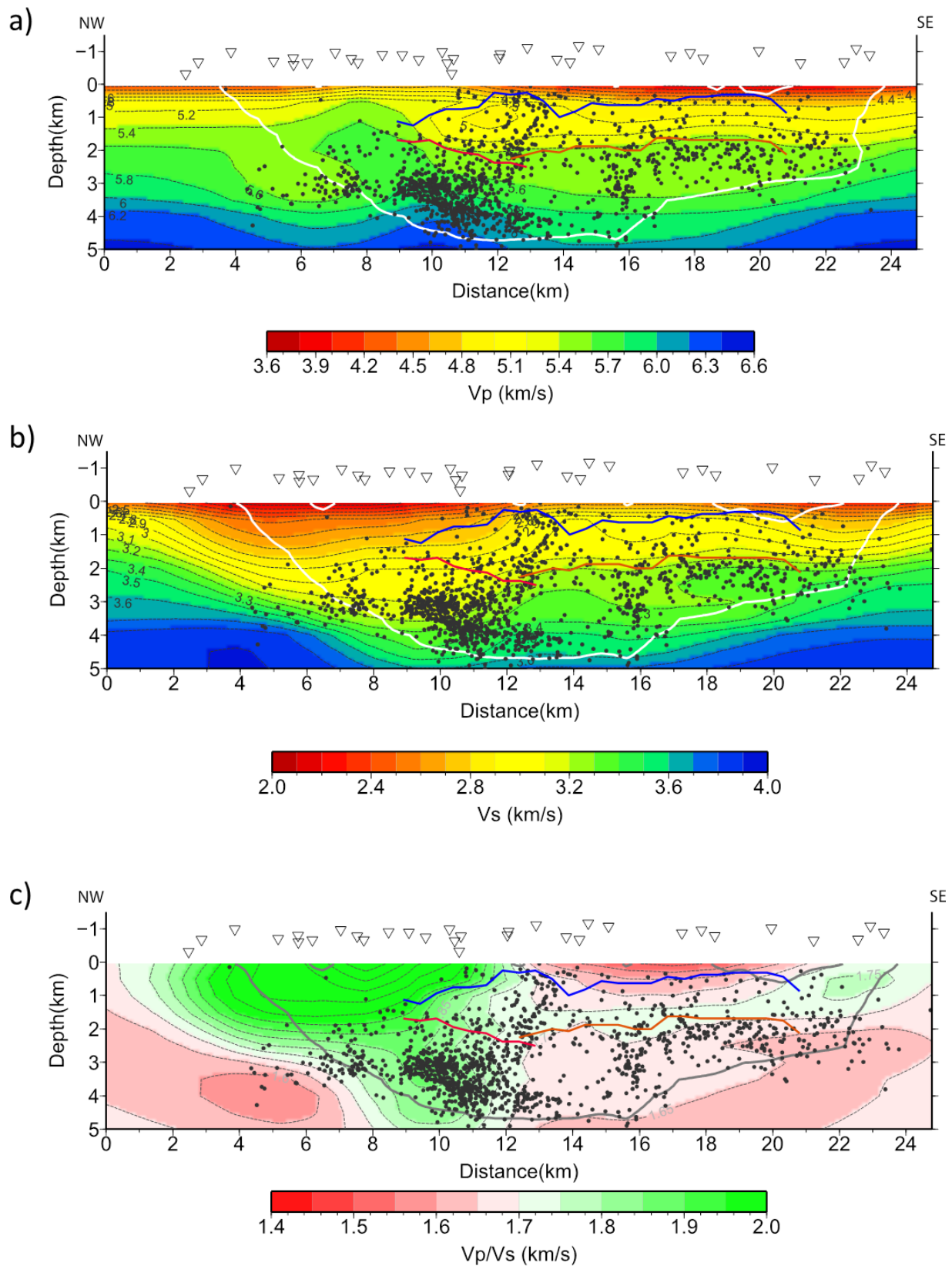


Figure 35. Cross-section of P and S-wave velocity models and V_p/V_s ratio. The models are projected onto the NW-SE cross-section indicate with the black line in the first panel of figure 19. The blue solid line indicates the top of the steam reservoir, the orange line the top of felsite and the red line corresponds to the top of the high temperature reservoir as reported by Beall and Wright (2010). a) Vertical cross-section along NW-SE direction of P-wave velocity model. b) Vertical cross-section along NW-SE direction of S-wave velocity model. c) V_p/V_s ratio images deduced from the sections shown in the figures c and d.

The cross-section view in Fig. 38 shows that both models seem to delineate the main geological features of the field, as for the precedent works (Kirkpatrick et al., 1997; Zucca et al., 2011). In particular, the iso-velocity curves of 5.4 km/s for V_p and 3.2-3.4 km/s for V_s correspond to the top of the felsite. Most of the seismicity in ZONE1 is clustered between 2.5 and 4.5 km depth, whereas the seismicity in ZONE2 is shallower. The V_p/V_s ratio reveals strong deviations from the expected value of 1.73 throughout the reservoir. A high V_p/V_s anomaly is present in ZONE1 and can be correlated to the high V_p in the same area (Kirkpatrick et al., 1997). Moreover, in this area the most of the seismicity occurs, and the temperature is the highest in the field. Thus, although relatively high V_p/V_s values are generally associated with fluid-filled fractured rocks, at The Geysers these can be also related to the temperature.

2.3 V_p/V_s ratio temporal variation

The temporal variations in the seismic properties of the hosting medium can be observed by means of the variations of the V_p/V_s ratio evaluated at the single stations and through time-lapse tomography (4D). For the purpose of the analysis the whole catalogue, from August 2007 to April 2011, was divided into consecutive epoch periods of 6 months, with an overlapping of 2 months.

A technique for the large-scale identification of the medium's properties was applied, since it can provide complementary information with respect to the tomographic analysis. The method allows to evaluate the temporal variation of the V_p/V_s ratio, which can be related to the directional properties of the fluid diffusion process, by using the arrival times of the P and S phases as seismological observables (Wadati, 1933). After separately taking into account the events belonging to the two zones and the catalogue subdivision defined above, the V_p/V_s ratio was evaluated for each event at each station. For each epoch, an interpolated colour map of the mean values of the ratio at each station is presented in Fig. 37, in order to show the V_p/V_s ratio spatial variation. The V_p/V_s values are calculated by considering the receiver configuration (par. 2.1.2), therefore the values are attributed to the area under the stations. The continuous maps are obtained by interpolating the values that have been found for each station.

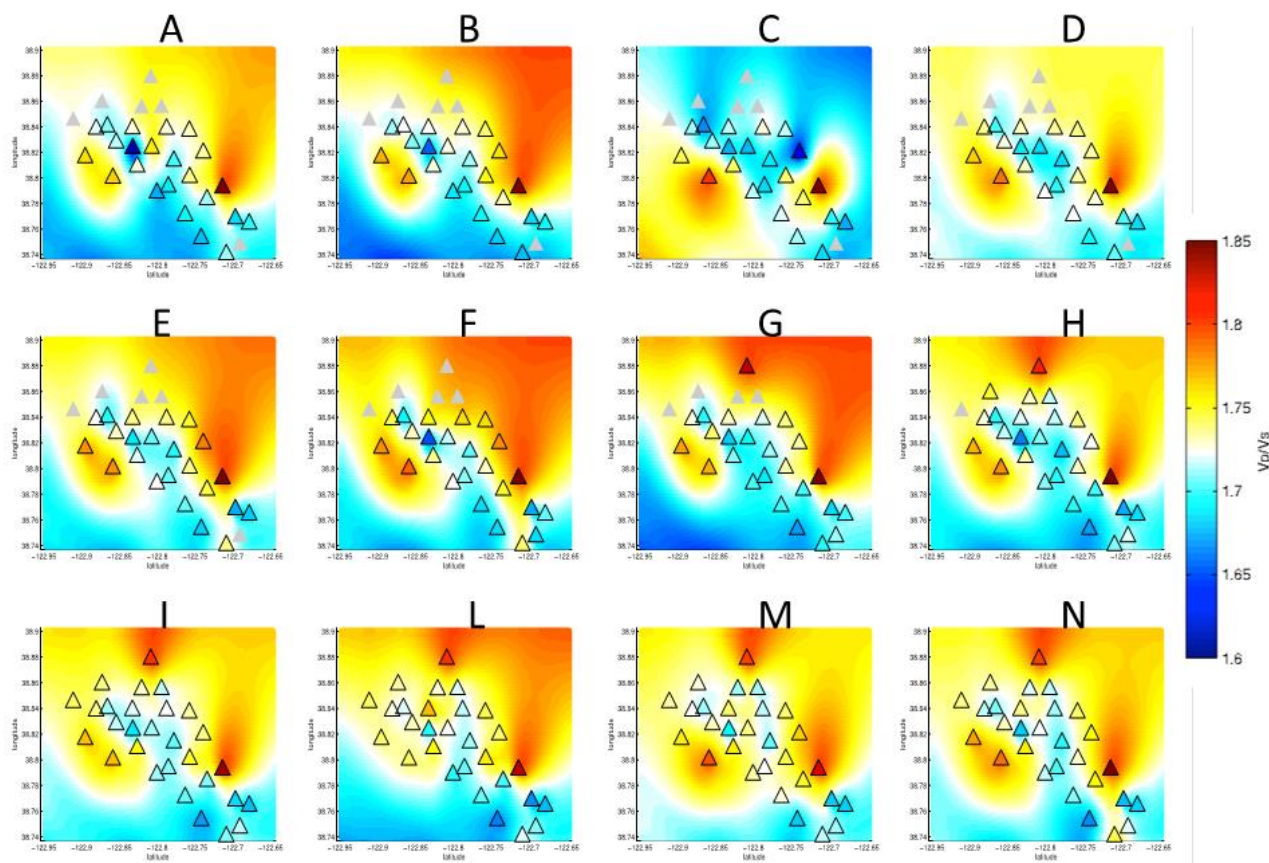


Figure 36. Plane view of V_p/V_s ratio spatial and temporal variation. The V_p/V_s values are calculated by considering the receiver configuration (par. 2.1.2), therefore the values are attributed to the area under the stations. The continuous maps are obtained by interpolating the values that have been found for each station. The stations represented in grey are the ones for which the recordings are not enough for the calculation of V_p/V_s ratio.

The V_p/V_s ratio ranges from 1.65 to 1.85, in agreement with the work of Gunasekera et al. (2004). The assumption of this technique is that the V_p/V_s ratio is constant along the ray path, so that the value found at the stations may be considered as the combination of the anomalies contributions at different depths. The plots in Fig. 38 (bottom) represent the 1D V_p/V_s ratio trends for some stations of the network that show similar patterns. We divided the area into four parts, then we plotted the ratio trend for the stations of the same area on the same panel (Fig. 38, top panel). These plots also indicate a high variability of the V_p/V_s ratio in the different time intervals. For some stations it varies from values lower than 1.7 to 1.8. The former value can be attributed to the depletion of pore liquid water and to its replacement with steam, while the latter is associated with the presence of liquid water. The Geysers area, where the changes in pore-pressure, in the pore fluid phase, and in the water content of minerals are caused by steam removal, can produce the observed variability in the V_p/V_s ratio.

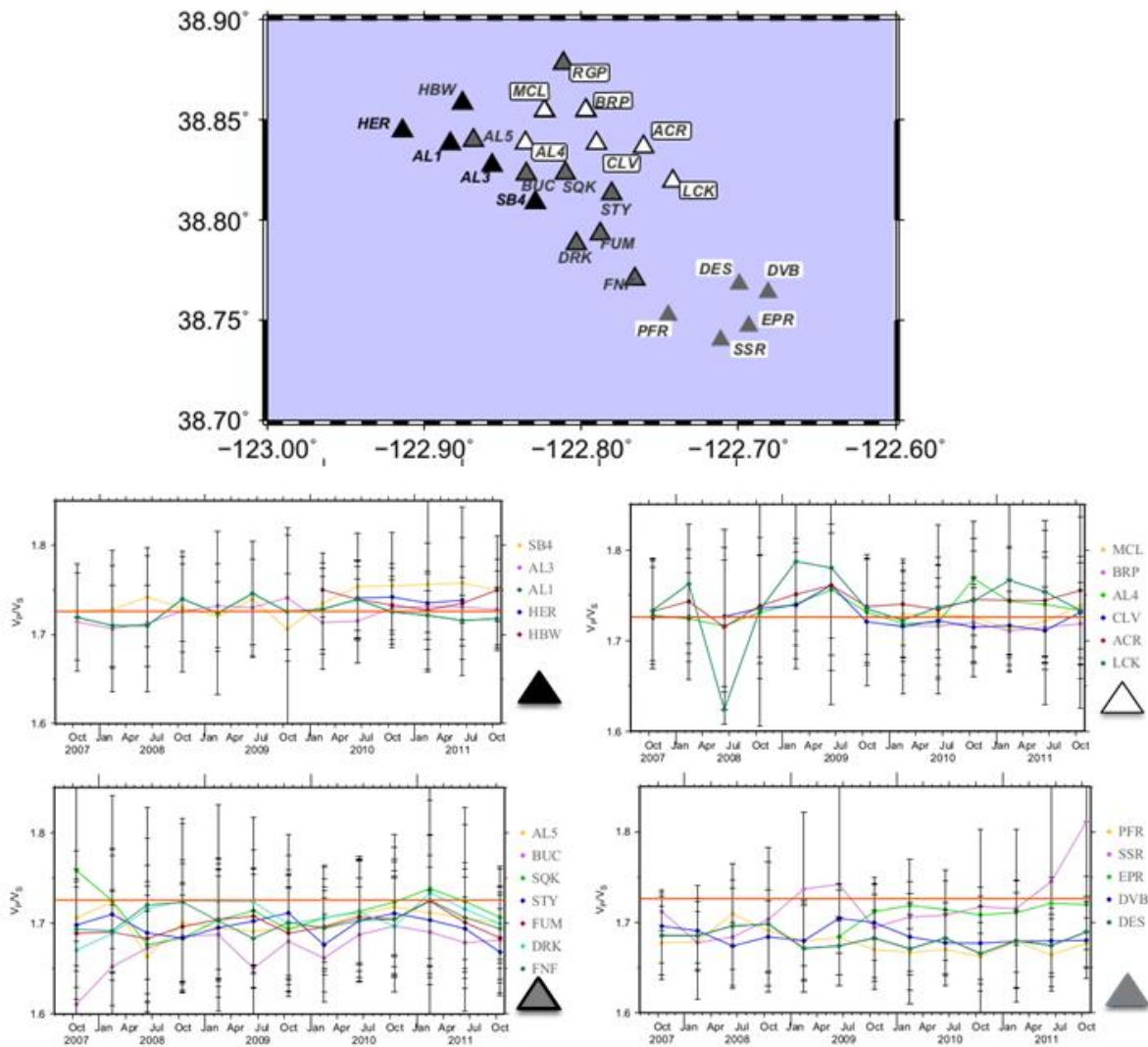


Figure 37. V_p/V_s ratio vs time epoch. The four panels show the V_p/V_s ratio in function of time epoch for different stations, grouped according similar trend. The orange line represents the average V_p/V_s ratio of 1.73.

2.4 Time-lapse tomography

As previously mentioned, the 4D tomography consists in applying the 3D tomography to consecutive epochs. Here we present a preliminary analysis for the 4D tomography in which we considered a fixed length of the time windows. For the purpose of the analysis the whole catalogue, from August 2007 to April 2011, was divided into consecutive epoch periods of 6 months, with an overlapping of 2 months. The idea is to use the information retrieved from this preliminary analysis to build up a complete 4D tomography procedure, as described in par. 2.2 of PART I.

In this analysis, the 3D P- and S-wave velocity models, which were inferred by considering the whole data-set shown in the previous paragraph, was used as the starting model in the inversions for each epoch. The model parametrization is the same as for the initial model. We evaluated the results in terms of V_p and V_s and their percentage variation with respect to the initial model (Fig. 39). For each model the DWS is computed in order to determine the well resolved regions.

Factors that affect V_p , V_s , and V_p/V_s at The Geysers include lithology, temperature, pore-pressure and pore fluid phase. Among these factors, the temperature of the reservoir has remained fairly constant in recent years (M. Stark, personal communication, 2000) despite the exploitation. Thus, the changes in pore pressure, pore fluid phase, and in the water content of minerals caused by steam removal are probably responsible for the changes observed in the anomaly.

Thus, the observed changes in velocity might be correlated to the field operations, such as fluid injection or steam production, which are not constant during each year, but show seasonal variations (e.g. Convertito et al., 2012). The inferred temporal variation in the velocity pattern (V_p , V_s , and V_p/V_s ratio) suggests a non- isotropic fluid diffusion in the whole geothermal field.

The 4D tomographic images in Fig. 39 show a variation that does not exceed 10% for all the epochs, accordingly with precedent works (Gunasekera et al., 2003). The presence of some anomalies seems to be rather periodical. This is the case, for example, of the + 5% anomaly in the epochs from A and B and of the -3% anomaly in the epochs D, F, I and L. The observed temporal variations in V_p and V_s indicate that the effect of water injection is more pronounced for V_s than for V_p . The observed V_s variation is consistent with the results of Boitnott and Bonner (1994), who found that the V_s variation can be related to the variation of shear modulus, from dry to saturated, of core samples extracted at The Geysers.

The anomaly of the high V_p/V_s ratio seems to vary its magnitude and location in the different epochs. According to Gunasekera et al., (2003) the variation in the V_p/V_s ratio anomaly can be attributed to the depletion of pore liquid water in the reservoir and to its replacement with steam. Moreover, variations in the V_p and V_s fields, which we also observe in our tomographic images, indicate that water depletion is the dominant process in the central part of the exploited reservoir, and pressure reduction and mineral drying are the dominant processes in the northwest and southeast parts of the reservoir.

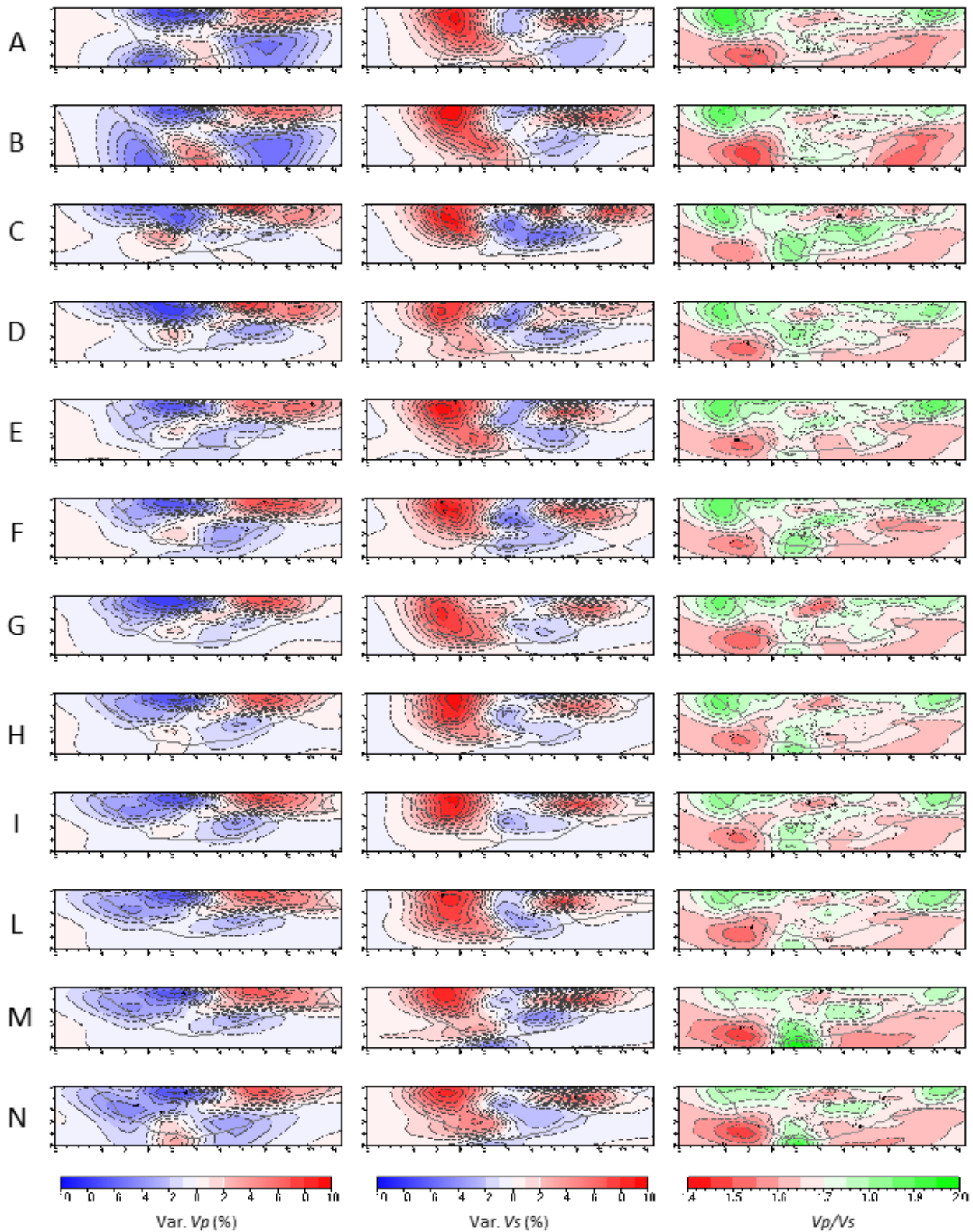


Figure 38. 4D seismic tomography. Each panel shows the tomographic model, for each time epoch, projected onto the NW-SE cross-section, indicated by the black line in the first panel of Fig. 35. The first column represents the variation of the V_p model with respect to the mean V_p model (calculated on the entire period); the second column represents the variation of the V_s model with respect to the mean V_s model (calculated on the entire period); finally, the third column represents the V_p/V_s ratio model.

2.5 Results and conclusion

The seismic rate at The Geysers is as much as 45 times higher than that of the surrounding area, and over 140ML, 1.2 earthquakes occur every month. Most of this activity is thought to be induced by geothermal exploitation, which includes both the removal of steam and fluid injection (Eberhart-Phillips and Oppenheimer, 1984; Stark, 1990; Stark and Davies, 1996). Thus, it is of great importance to monitor the conditions of the reservoir, in order to mitigate the risk associated with induced seismicity.

High-resolution seismic tomography can be used to image the elastic and anelastic properties of the reservoir. In turn, the physical properties can be related to the fluid presence and migration inside the reservoir. Our results clearly show that it is possible to obtain highly accurate information on the elastic properties of the geothermal reservoir, if a high-density station network is available, such as the Lawrence Berkeley National Laboratory Geysers/Calpine network. The main results of our tomographic application are the good correlation between the V_p , V_s trend and the geothermal/geological characteristic of the reservoir and the high V_p/V_s ratio anomaly in correspondence of the high-temperature reservoir, where the most of the seismicity occurs.

Time-lapse seismic tomography can be used as a medium to monitor geothermal reservoirs on a longer term. Factors that affect V_p , V_s , and V_p/V_s at The Geysers include lithology, temperature, pore-pressure and pore fluid phase. Thus, the changes in pore-pressure, pore fluid phase, and in the water content of minerals that are caused by steam removal are probably responsible for the changes observed in the velocity values.

Besides, the V_p/V_s ratio variations are more suitable for the short-term monitoring of geothermal reservoirs. Moreover, the presented results, in accordance with precedent works (Gunasekera et al., 2003; Gritto et al. 2014), show that the V_p/V_s ratio is positively correlated to the temporal changes in the reservoir's saturation. Such a V_p/V_s ratio can be used to estimate and possibly predict saturation changes in small areas of the reservoir, such as around injection wells or throughout the whole reservoir, by using tomographic techniques.

As further developments, the obtained results justify the application of a complete 4D tomographic procedure (as explained in par. 2.2). Once the well resolved and coherent 3D velocity images have been obtained for each epoch, the next step will be to interpret the changes in the obtained values and anomalies on the basis of reservoir operation. This means integrating the seismic images with further information on the reservoir's condition, such as location, timing and rate of fluid injection, information on rock physics coming from modelling or laboratory measurements, etc.

Chapter 3 : *The SOLFATARA volcano*

3. Introduction

Solfatara is a tuff cone, which was formed between 3.8 and 4.1 ka ago (De Vivo et al., 2001), located 1.5 km NE of the town of Pozzuoli and about 10 km west of the city of Naples in Southern Italy. The sub-rectilinear NE and SW rims are cut by two normal faults that strike NW-SE, along which deep geothermal fluids can ascend. Outside the crater, two NW-SE striking faults cut the eastern part of the tuff cone (Bianco et al., 2004).

Solfatara is one of the many volcanoes located within Campi Flegrei caldera (Fig. 40). This is a nested, resurgent caldera resulting from two large collapses related to the Campanian Ignimbrite (39 ka) and the Neapolitan Yellow Tuff (14 ka) eruptions (Orsi et al. 1996). Campi Flegrei volcanic system is still active, since the last eruption occurred in 1538 A.D. at Monte Nuovo. Zollo et al. (2008) identified a deep, sill-like, mid-crustal magmatic body supplying heat to this volcanic system at a depth of 7-8 km. They have also identified another shallower interface at 2.5 km depth associated with a discontinuity between the older caldera deposits and a fluid-saturated metamorphic rock layer. The caldera has been characterized by periodic episodes of extended, low-rate ground subsidence and uplift, a phenomenon called bradyseism, accompanied by intense seismic and geochemical activity (e.g., De Natale et al. 1991). During the past century, three main episodes of bradyseism occurred in the area: 1950-1952, 1969-1972, 1982-1984 (Del Gaudio et al. 2010). During the subsidence following the 1984 crisis, a series of small uplift episodes and seismic swarms occurred at the Solfatara. Saccorotti et al. (2007) suggest that these earthquakes are likely to be associated with the vibration of a buried cavity filled with a water-vapour mixture at poor gas-volume fractions. The role of fluids in bradyseism has been recognized by many authors (e.g., Gaeta et al. 1998, Battaglia et al. 2006, Cusano et al. 2008).

The Solfatara crater is characterized by intense diffuse degassing, and fumarolic emissions (e.g. Cusano et al., 2008; Chiodini et al., 2005; Chiodini et al., 2009). Chiodini et al. (2001) showed that Solfatara releases about 1500 t/day of volcanic-hydrothermal CO₂ as a result of diffuse degassing through soil, during which about 3350 t/day of steam condense. This hydrothermal water mixes up with the meteoric one. The energy released by degassing at Solfatara is much higher than the energy released within the caldera during the current

period, through other processes as thermal conduction, earthquakes, and ground deformation. Moreover, the impressive magnitude of diffuse degassing process confirmed the relevance of fluid and heat transport at Solfatara (Chiodini et al., 2001) and prompted further research to improve the understanding of the hydrothermal system feeding the surface phenomenon.

Although the magmatic source is rather deep, the changes in its outgassing rate greatly affect the shallow hydrothermal system processes, which can therefore be used as a constraint for the fluid migration processes occurring at depth (Petrillo et al. 2013, Coco et al. 2015). This justifies the growing interest of the last years in delineating the physical properties of the shallow hydrothermal system of Solfatara as one of the means to assess the level of potential danger characterizing this crater of the Campi Flegrei volcanic complex.

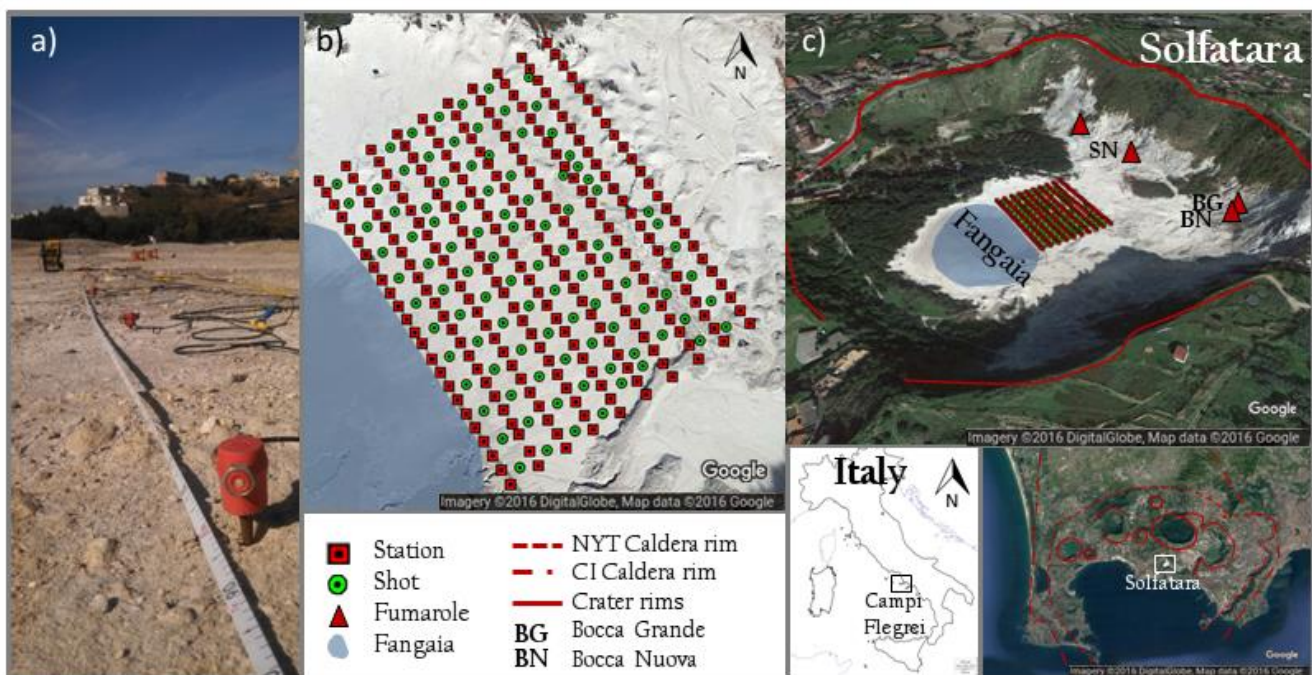


Figure 39. Solfatara with station-shot configuration. a) A photo of RICEN experiment, with an example of seismic sensors. b) Station-shot configuration. c) The Solfatara crater, with evidence of crater rims, fumarole, Fangaia and the station-shot configuration. The maps in figure 1b-c has been obtained with Google Maps 9.38.1 2016 (Map data: Google, DigitalGlobe): Solfatara, Pozzuoli, Metropolitan City of Naples, Italy retrieved from <https://www.google.com/maps/@40.8174278,14.1393587,1292a,20y,41.32t/data=!3m1!1e3>

3.1 RICEN experiments and catalogue construction

In the framework of the experiment RICEN, Repeated Induced Earthquake and Noise (EU Project MEDSUV), an active seismic experiment was carried out between September of 2013 and November of 2014 in order to provide time-varying high-resolution images of the

structure of Solfatara (Serra et al., 2016). A grid of 240 receivers, placed at distance of 5 m on 10 lines which were 10 m distant from each other, was deployed in the Solfatara crater (Fig. 40b). A vibroseis energized the soil at the centre of almost all grid cells (green dots in Fig. 40b). A large and highly informative data-set was then built. The data used in this work were acquired during the first campaign, which was carried out on September of 2013.

3.2 State of the art

Bruno et al. (2007) imaged the shallow and intermediate subsurface of Solfatara through the integration of high-resolution geophysical and hydrogeological investigations, including 2D P-wave velocity and Electrical Resistivity Tomography (ERT) profiles. Their results show that the Solfatara subsurface structure can be roughly divided into two zones: a dry, outcropping layer and a underlying saturated zone, in which faults and fractures act as preferential escape conduits for the hydrothermal fluids (Bruno et al., 2007; Isaia et al., 2015).

Byrdina et al. (2015) used the results from the ERT survey, the mappings of diffuse CO₂ flux, the ground temperature and self-potential (SP) to understand the mechanisms and paths of shallow fluid circulation. They interpreted the resistivity changes at depth, associated with surface gas flux anomalies, as a double-plume structure: a liquid-dominated conductive plume below the Fangaia mud-pool and a gas-dominated plume below the Bocca Grande fumarole (Fig. 40c).

Isaia et al. (2015) integrated the electrical resistivity tomography investigations with the volcano-tectonic information to better constrain the subsurface structure by outlining a complex hydrothermal system. In particular they assume that the upper zone of Solfatara, about the first 100 m depth, comprises desegregated rocks and collapse breccias, post-eruptive sediments, while the lower sector, up to about 3-4 km, is where the gas-saturated conduit is connected to a magmatic source.

Referring to Campi Flegrei caldera, de Lorenzo et al. (2001) and De Siena et al. (2010) carried out two studies on the anelastic properties of the northern part of Campi Flegrei caldera, including the Solfatara crater. Both studies retrieved an heterogeneous distribution of low-Q_p and high-Q_p anomalies in the investigated area, thus confirming the strong geological complexity of the subsoil. Moving closer to Solfatara the two works reveal different features: De Siena et al. (2010) found a high Q_p and low Q_s body. Their correlation with the low V_p/V_s ratio and the low V_p was interpreted as due to the effect of a small reservoir of gas. de

Lorenzo et al. (2001), on the other hand, found low Q_p values at shallow depths, well correlated with high V_p/V_s value (Aster and Meyer, 1988): this correlation was interpreted as produced by densely fractured, porous and fluid-filled rocks. A similar interpretation was also provided also by Tramelli et al. (2006) who found a high-scattering zone in the area of the Solfatara crater. A recent attenuation tomography (Serlenga et al., 2016) mainly focused on the shallowest subsurface of Campi Flegrei offshore caldera. The retrieved anelastic images are not spatially correlated with Solfatara; however, these describe the very shallow volcanic system as an environment which is greatly affected by the heterogeneous distribution and the different saturation conditions of fluids permeating sediments and rocks of caldera.

By using a subset of the data-bank obtained through the RICEN experiment, Serra et al. (2016) found the spatial variation of surface waves phase and group velocities. By Inverting the related dispersion curves they obtained a one-dimensional S-wave model for different sub-grids. Together, the different 1-D S-wave models provided a three-dimensional description of the S-wave model in the area down to about 15 m depth. In the upper 4 m, they associated the changes of the S-wave velocity to the temperature gradient, while at greater depths, the seismic images were correlated with the resistivity maps, obtained from the measurement that was carried out during the RICEN experiment. The measurement evidenced the presence of a the water layer close to the Fangaia area and an abrupt variation in NE direction.

3.3 Velocity tomography

The goal of the present study is to obtain an ultra-high-resolution (metric) 3D velocity image of the shallow (up to 35 m) hydrothermal structure of the central part of Solfatara crater by using a technique of delay-time tomography, which uses the P-wave first arrival times. Due to the extremely dense acquisition lay-out, the 3D tomographic survey allows to achieve an unprecedented spatial detail on the shallow velocity structure which can help understand the complex hydrothermal degassing and condensation processes into the porous rocks media. In this way, the interpretation obtained by stratigraphic analysis and resistivity profiles (Bruno et al., 2007, Isaia et al., 2015) can be complemented. For our purposes, the results of temperature and CO₂ flux measurements and resistivity survey carried out in the frame of the RICEN experiment will be used to further constrain our interpretation. In fact, several studies over the last few years showed how the multi-parametric analysis, of combined geophysical and/or geochemical data-sets, has been helpful to investigate the complex dynamics of volcanoes systems at different scale (Harris et al., 2005; Caliro et al., 2005; Bruno et al. 2007; Aiuppa et al., 2010).

3.3.1 Data processing and inversion strategy

The RICEN experiment consisted in three successive geophysical surveys carried out at the Solfatara volcano respectively in September 2013, May and November 2014 each one lasting one week. During each experiment, the recording both of active seismic data and of the continuous ambient noise was performed. A dataset with more than 75,000 seismograms has been collected in total during the active seismic part of the three experiments. Active seismic data were obtained using a Vibroseis Truck soil energizator which operated at the frequency range 5-125 Hz. Seismic waveforms were recorded by 4.5 Hz vertical component geophones (GS-11D, Fig. 40a).

In this study, we analyse the data collected during the first experiment. In particular, an area of 90 x 115 m² was sampled by a regular grid of 240 vertical sensors which were deployed at the crater surface (40b-c). The seismic network geometry was set up according to a two-dimensional (2D) grid with 10 lines of 24 sensors, with a 5 m spacing between the stations (i.e. in-line distance). The distance between two adjacent lines (i.e. cross-line distance) was 10 m. About 100 shot-points were energized on a staggered grid relatively to the receivers grid. For the vibrational sources, both the in-line and cross-line inter-distances were 10 m. For each shot position, three consecutive energizations were performed and waveforms at each site were stacked in order to increase the signal-to-noise ratio.

It is well known that the volcanic area is a very complex one where effects of scattering and attenuation could in general contaminate the first arrival picking. In order to check the requirements for the prospected precise picking analysis, we verified *a posteriori* that the signal-to-noise ratio was relatively high at the first arrival onset, and we evaluated waveform/picking coherence vs. offset along the seismic section. Moreover, through an analysis of particle motion direction, we validated the use of the vertical components though the complexity of medium and very short distance between source and receiver.

The P-wave first arrivals have been first detected through a Neural Network implemented into the ProMAX SeisSpace software (Caudill, 1989; Fahlman & Lebiere, 1990; Rumelhart & McClelland; 1986 and Wasserman; 1989) that performs an automatic neural network algorithm trained on a limited, manually picked dataset of source-receiver couples. In that way about 19,000 picked P-wave travel times have been obtained. Thereafter, the picking dataset has been manually validated on the basis of a visual inspection of seismic signals. Data affected by a high pick uncertainty (> 0.05 s), based on a very low signal-to-noise ratio

(<2), have been discarded. An example of one seismic section in the common-shot gather can be found in Fig. 41a. Moreover, for each shot, the travel times referring to the eight closest receivers have been excluded. In those cases, indeed, it was too difficult to correctly measure the P-wave travel time, due to the short pre-event time window available for picking. All data have been considered with the same weight, since only the best quality pickings have been considered for the tomographic analysis. The final selected dataset contained 17,418 P wave travel times relative to 94 sources and 240 receivers.

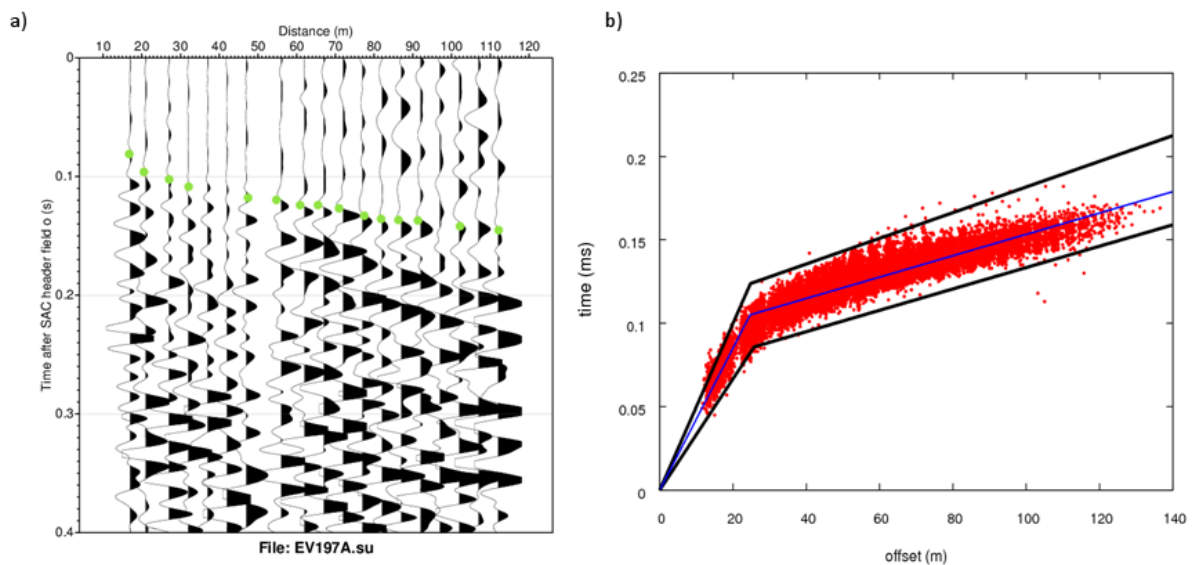


Figure 40. Data and travel-time-vs-distance plot. a) Example of seismic section in common shot gather. The processed traces concern the shot 194 recorded at stations 25 to 48. The green dots represent picks of first arrival P phases obtained with PROMAX and manually revised. b) Plot of travel-time-vs-distance (red dots). The black lines are the limit imposed for the construction of 1D initial velocity models. Blue line is the 1D initial model selected for the inversion.

In order to determine the 3-D P-wave velocity model, the selected travel-time dataset was inverted by applying an iterative, linearized, tomographic approach and by adopting a multiscale procedure (Zollo et al, 2002).

Due to the source-receiver configuration we have investigated a volume of $160 \times 160 \times 45 \text{ m}^3$, the top being at 100 m a.s.l. The three-dimensional hosting medium has been discretized with a grid of regularly spaced nodes. The inversion strategy was based on a *multiscale* approach (Zollo et al, 2002). Several inversion runs were performed by progressively increasing the density of grid points (e.g. increasing the model complexity) describing the velocity field, and at each iteration, the starting model is the one estimated in the previous run. The proposed procedure is equivalent in principle to moving from a low to high wavenumber description of the velocity field. The *multiscale* strategy does not depend on the scale of the application, because the basic assumption is that large wavelength anomalies in the velocity structure have a dominant amplitude compared with the smaller ones, which we believe is reasonable at all scales of investigation within earth media. This strategy has been already used in

seismic tomography (Zollo et al. 2002) and in migration techniques where it is known as “multi-scale” approach.

The final parameterization of the medium in the *multiscale* procedure is chosen by applying the corrected Akaike Criterion (AICc; Cavanaugh, 1997), which is based on a statistical comparison (AIC,) (Akaike, 1974) between models characterized by a different number of model parameters. By introducing the minimum AICc criterion, the problem of selecting the optimal model parameterization is solved by avoiding a subjective decision. The minimum AICc value, representing the best compromise between data misfit reduction and model simplicity, is obtained with the $10 \times 10 \times 5 \text{ m}^3$ grid spacing, which is the final parameterization in the *multiscale* procedure.

At first for the *multiscale* approach a coarser parameterization was used with a node-spacing of $16 \times 16 \times 7.5 \text{ m}^3$.

In order to take into account the possible dependence of the final tomographic solution on the starting velocity model we adopted the following strategy: (1) first, we estimated a reference 1D velocity model; (2) starting from this we generated a set of 200 1D initial models; (3) a 3D inversion is performed for each initial model.

The estimation of the 1D reference velocity model is obtained by a modelling procedure which minimized the RMS of the travel time residuals. This 1D reference model had 2-layers. As for the 200 1D initial models, they have been constructed as 2-layer models with the depth of the interface fixed to that of the reference 1D velocity model (10 m). The variability range of the velocities in the 2 layers was established by constraining the respective theoretical travel-time curve to lay within the limits defined by the scattering of measured data in a travel-time-vs-distance graph (see Fig. 41b and Fig. 42). Each 1D velocity model is used as a starting model for the data inversion. Then, by computing the average of the 200 final three-dimensional velocity models and the normalized standard deviation for each model parameter (σ/V_p), we observe that deviations from the average model on retrieved velocity values are less than 15%, except for some grid nodes (see Fig. 43).

The starting velocity model minimizing the final misfit of the residuals is chosen as the initial velocity model for the inversion with the coarser parameterization ($16 \times 16 \times 7.5 \text{ m}^3$) (see Fig. 42b). The three-dimensional P wave velocity model retrieved at the sixth iteration is used as starting model for a further data inversion in the final grid (spacing $10 \times 10 \times 5 \text{ m}^3$).

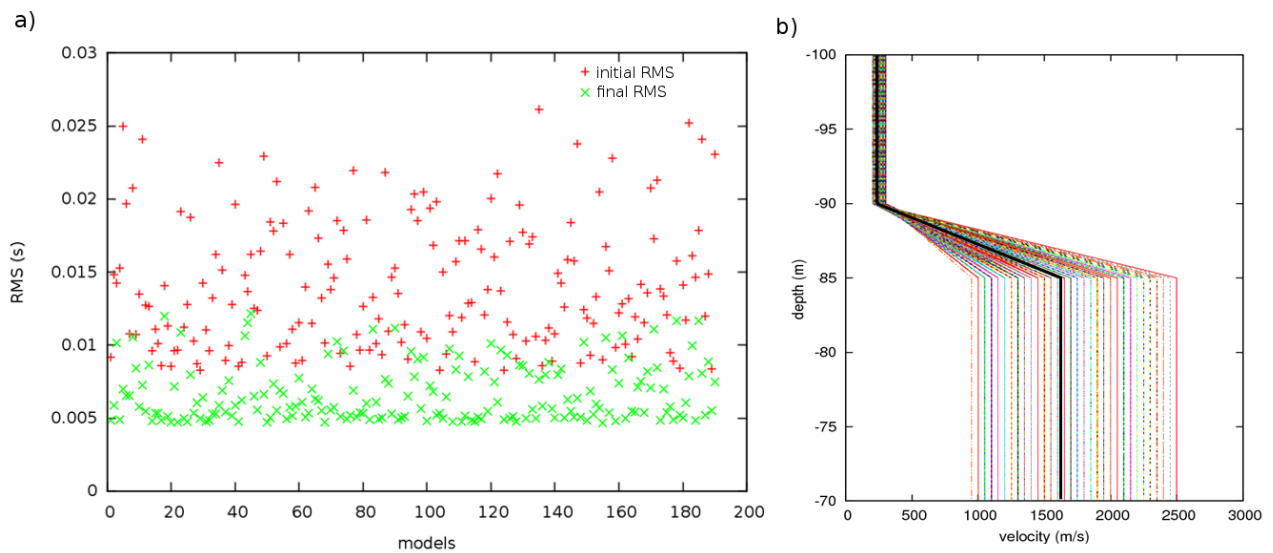


Figure 41. a) Distribution of final (green) and initial (red) RMS of the inversion with the 200 2-layer velocity models. b) Plot of the 200 2-layer velocity models. The solid black line represents the model with the least final RMS.

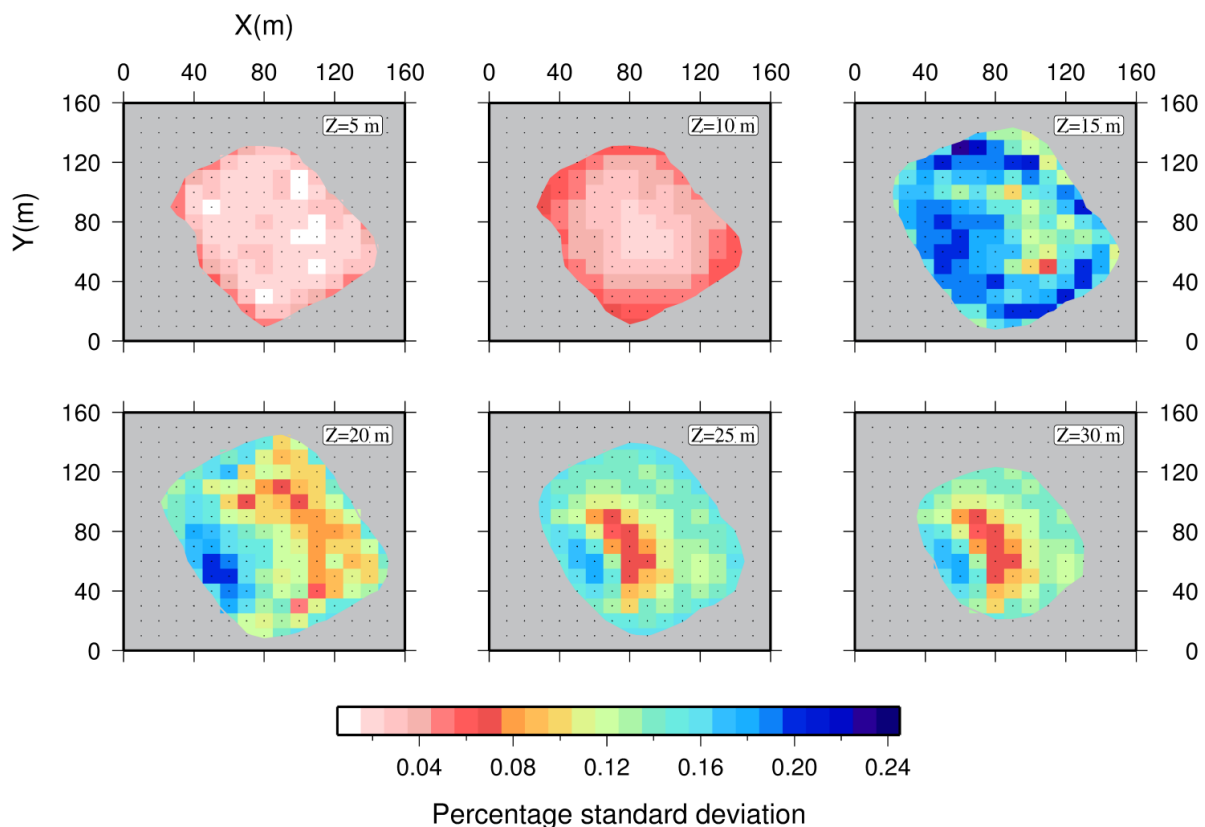


Figure 42. Map representation of the normalized standard deviation for each model parameter (σ/V_p) of the 3D velocity models obtained by the inversion with different 1D 2-layer initial velocity models. The slices are at a depth of 5 m, 10 m, 15 m, 20 m, 25 m and 30 m. The grey regions in each slice represent areas not well resolved.

For the calibration of the damping factor we followed an empirical approach: using real dataset, we performed several inversions for different values of damping. The data variance

and solution variance are computed after 6 iterations for indicated damping values. The chosen damping value is the one in which a small variance in the data corresponds to a small variance of the model. The L-curve representing the data variance in function of model variance are plotted in Fig. 44b, for the $16 \times 16 \times 6.5 \text{ m}^3$ parameterization and Fig. 44c, for the $10 \times 10 \times 5 \text{ m}^3$ parameterization. In both cases, the chosen damping value is 0.5.

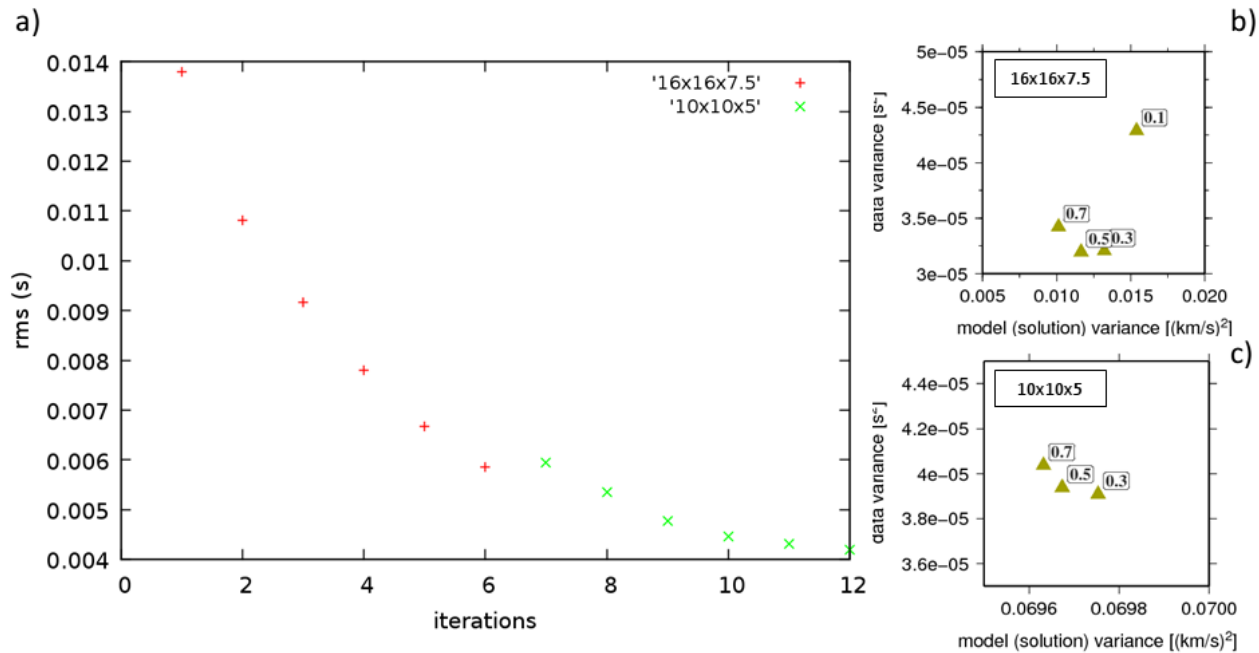


Figure 43. a) RMS curve as a function of number of iterations for the two parameterization of multiscale procedure. b-c) Trade-off curves for selecting optimal damping value for real data-sets. The figures in b) and c) represent the L-curve for the inversions for VP, respectively, in the coarse grid ($16 \times 16 \times 7.5 \text{ m}^3$) and in the finer ($10 \times 10 \times 5 \text{ m}^3$).

3.3.2 3D P and S velocity models

In Fig. 45 we show the map view at several depths of 3D velocity models obtained with the parameterization $16 \times 16 \times 7.5 \text{ m}^3$. The grey regions represent areas not covered by the rays. The black contour represents the area well the area for which the tree resolution parameters (RDE, S_j and DWS) are included in a threshold value. The model shows already the strong lateral variation of velocity values, from 20 m depth, which is then improved in the model obtained with the finer parameterization; although, overall, the velocity values are lower than the one of obtained with the parameterization $10 \times 10 \times 5 \text{ m}^3$.

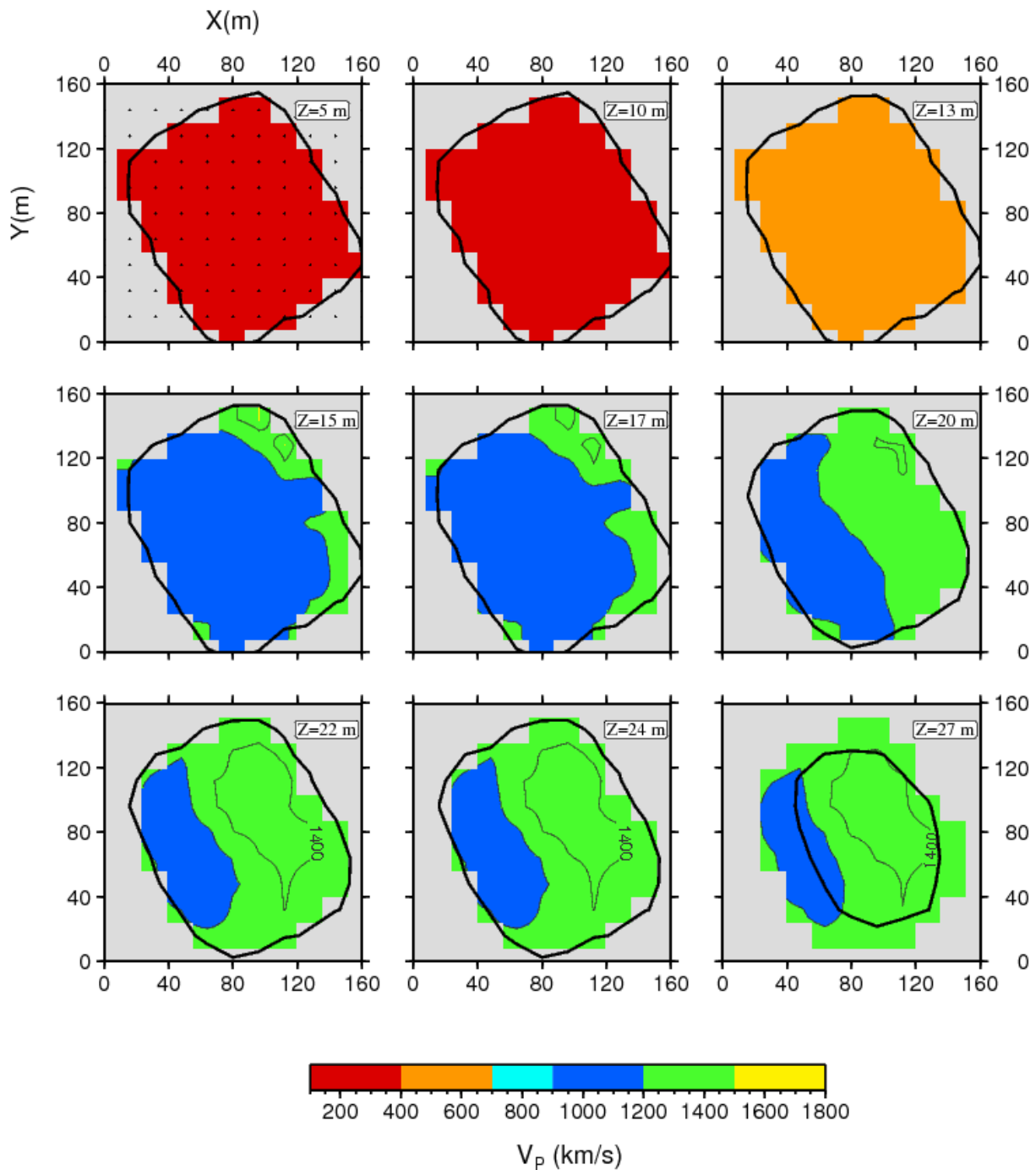


Figure 44. Map view at several depths of 3D velocity models obtained with the parametrization $16 \times 16 \times 7.5 \text{ m}^3$. The grey regions represent areas not covered by the rays. The black contour represents the area well the area for which the tree resolution parameters (RDE, S_j and DWS) are included in a threshold value

In Fig. 46 we show the 3D P-wave velocity model obtained with the finest parameterization ($10 \times 10 \times 5 \text{ m}^3$). Considering all the *multiscale* steps, we achieved a reduction of the root mean square of t residuals (rms) of about 70%, with a final RMS of 4 ms (see Fig. 47).

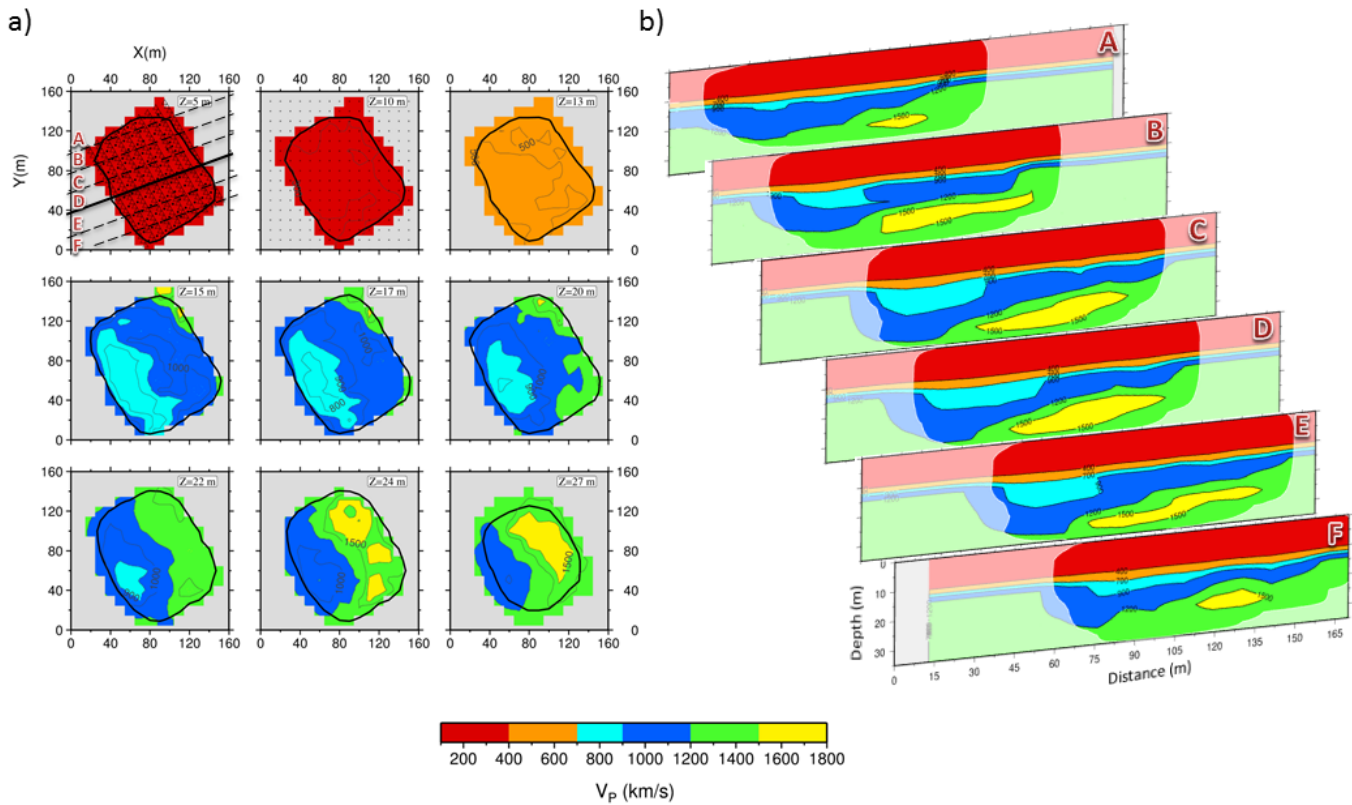


Figure 45. P-wave velocity model. a) Horizontal slice of P-wave velocity model at different depths. The grey regions in each slice represent areas not covered by rays. b) P-wave velocity model projected onto the SW-NE cross-sections located in Fig. 3a. The blurred regions in each slice represent areas not covered by rays.

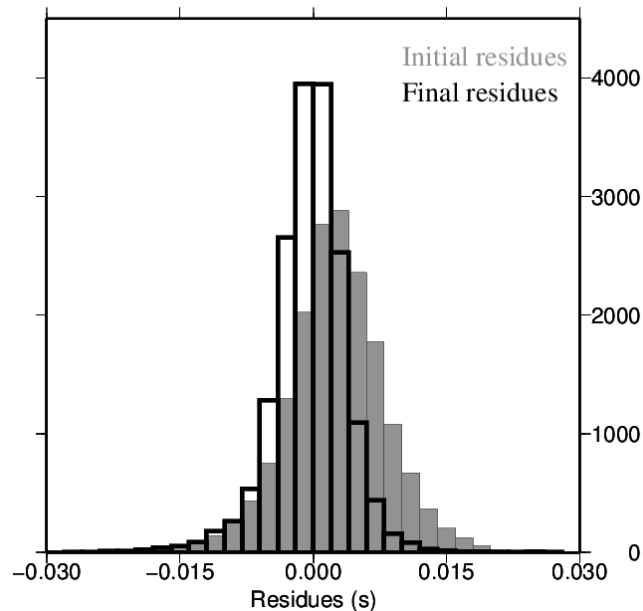


Figure 46. Distribution of inversion residuals for the finer parameterization 10x10x5. The grey histogram represents the initial residuals, the black one represents the final residuals. The final residuals histogram shows a tight distribution centered at zero.

The plane view of the model (Fig. 46a) shows a depth increasing P-wave velocity structure within the shallower 13-14 m depth, with velocity values ranging from 200 to 700 m/s. Between 13 and 15 m depth an abrupt increase of velocity is observed, from 500 m/s to 1000 m/s. Moreover, around these depths, the model shows a significant lateral variation. In particular, from 15 m to 22 m depth, in the Western part of the model, a low velocity anomaly trending NW-SE is imaged. Its P-wave velocity is about 800 m/s and its areal extension decreases with depth. From 22 m to 30 m depth, an NW-SE interface separates two distinct zones characterized by different compressional velocity values. The Western depth section has a velocity ranging between about 900 m/s and 1200 m/s, and the Eastern one has higher velocity values of about 1200-1500 m/s. Finally, a well confined, lens-shaped, high P-wave velocity zone is imaged in the deepest part of the model, with velocity values higher than 1500 m/s.

The SW-NE cross-sections, shown in Fig. 46b, allow to better delineate the shape and areal extension of the features which were already identified in the plane view representation. First of all, the intermediate layer, with velocity ranging between 1000 and 1100 m/s, progressively deepens toward SW. Moreover, it quickly rises again at the interface with the mud pools (Fig. 46b). Then, the low velocity anomaly, included in the previous layer, is more extended in the central part of the model (see section B-C-D in Fig. 46b), and reduces towards the northern and southern edges of the grid (see section A-E-F in Fig. 46b). Finally, the same behaviour is observed for the deep high velocity anomaly, which becomes thinner and thinner at the edges of the grid and completely disappears in the "F" section in Fig. 46b.

3.3.3 Resolution analysis

In order to assess the reliability of the final solution, we numerically computed the resolution matrix from which we extracted the RDE (Resolution of Diagonal Elements) and the spread function (Sj, Michelini and McEvelly, 1991).

The full resolution matrix is calculated starting from the tomographic matrix using the relation 11 of Rawlinson and Spakman (2016). The full resolution matrix is represented in terms of its resolution diagonal elements RDE and the spread function Sj related to off-diagonal elements. In particular, the Sj is defined as equation (12) and the DWS as equation (13).

The resolution parameters, i.e. RDE, Sj and DWS, are calculated for each parameterization, since they depends on it. In Fig. 48 are shown the RDE (a), the Sj (b) and the DWS (c) for the finest parameterization 10x10x5 m³, and in Fig. 49 the same parameters for the coarser

parameterization $16 \times 16 \times 7.5 \text{ m}^3$. In Fig. 45 and 46 the black contour delimitates the resolved area, i.e. the area for which the tree resolution parameters (RDE, S_j and DWS) are included in a threshold value. The threshold values of S_j and DWS are chosen in order to obtain a similar contour, binding the RDE to be higher than 0.9.

The results of resolution analysis allowed us to assess that the resolved area is about $100 \times 120 \times 35 \text{ m}^3$ (see Fig. 48-49).

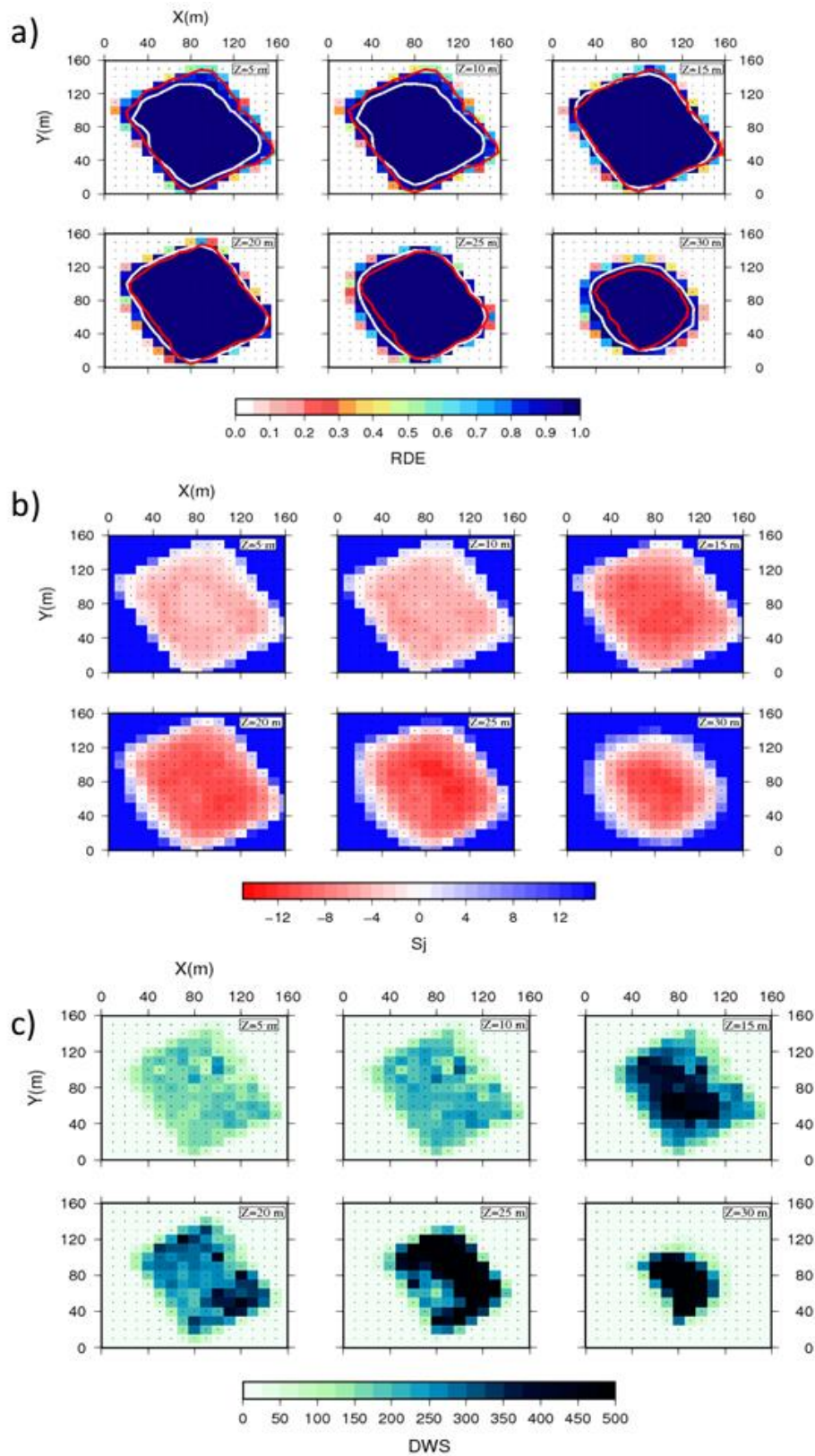


Figure 47. Resolution parameters matrix for 3D velocity model obtained with the parameterization $10 \times 10 \times 5$. The full resolution matrix is represented in term of resolution diagonal element RDE (a) and spread function S_j (b) at four different depth. In panel a) the red and white contour represents the threshold values of S_j (red) and DWS (white) chosen in order to obtain a similar contour, binding the RDE to be higher than 0.9. The c) panel represents the DWS at different depths.

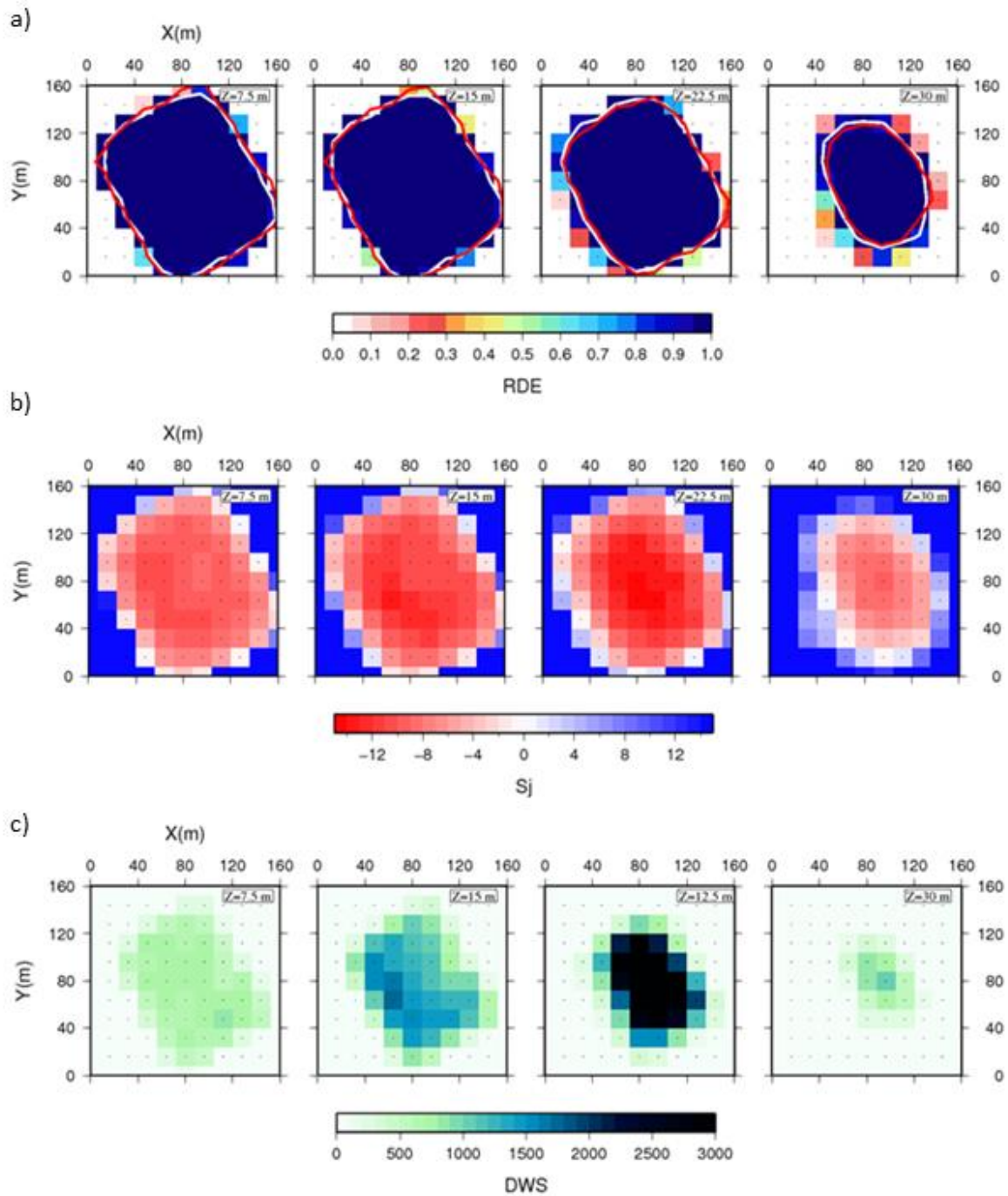


Figure 48. Resolution parameters matrix for 3D velocity model obtained with the parameterization $16 \times 16 \times 7.5$. The full resolution matrix is represented in term of resolution diagonal element RDE (a) and spread function S_j (b) at four different depths. In panel a) the red and white contour represents the threshold values of S_j (red) and DWS (white) chosen in order to obtain a similar contour, binding the RDE to be higher than 0.9. The c) panel represents the DWS at four depths.

3.3.4 Multi-parametric analysis

In this work we obtained a new 3D, high-resolution image of P-wave velocity of the Solfatara crater through an inversion strategy based on a *multiscale* approach. We suggest that the retrieved subsoil velocity images can be explained in terms of the interaction between structural patterns and degassing dynamics within shallow hydrothermal circulation cells (Bruno et al., 2007). According to the geochemical analysis of the Solfatara fumarolic gases performed by Caliro et al. (2007), this degassed flux is composed by deep magmatic CO₂-rich fluids mixed with hydrothermal liquids of meteoric origin.

The Solfatara shallow stratigraphy consists of eruption deposits, *tephra*, which are hydrothermally altered and mainly composed of alternating fine to coarse ash deposits with limited distribution, scoria layers, and lavas (Isaia et al., 2015). In detail, the first 10-15 m are composed by recent, unconsolidated deposits; beneath this layer, the deeper 20-30 m thick deposits have a dominant composition of Astroni tephra, i.e. sandwave, ash surge and fallout deposits with variable degrees of consolidation (Isaia et al., 2015). The retrieved velocity values, $V_p < 1800$ m/s, are consistent with the ones found in other volcanic areas for the tephra deposits (Sisson and Dibble, 1981; Mora et al., 2006). In particular, in the first 10-15 m the P-wave velocity values range from 200 m/s to 700 m/s, these values correspond to aerated tephra (Mora et al., 2006). On the other hand, the higher velocity values in the deeper zone (V_p up to 1800 m/s) can be related to the tephra deposit, which are more consolidated and possibly saturated (Sisson and Dibble, 1981; Mora et al., 2006).

Taking into account that the presence of fluids and their circulation may greatly affect the rock volume and therefore, the average compressional wave velocity (Toksöz et al., 1976), we expect that the tomographic images can constrain the possible location and phase of permeating fluids. For this purpose, we compared our seismic tomography with 2D cross sections of resistivity (ρ) and with temperature and CO₂ flux measurements. Serra et al. (2016) show how the integration of velocity images with resistivity tomography provides a more complete interpretation of the complex Solfatara system. A high-resolution electrical resistivity tomography was performed with sixteen 115-m-long NW-SE profiles and twenty four 75-m-long NE-SW profiles. The surveys were carried out in March and May 2014 during the RICEN experiment. We used a Wenner-Schlumberger configuration with a 5 m spacing between electrodes. In addition to these short profiles, we used the 1 km-long profile performed by Byrdina et al., 2014 (labelled Pr2 in their paper) in order to increase the resolution at depth. Resistivity data were filtered by removing values with a standard deviation exceeding 5 % or when the injected current was lower than 20 mA. The 3-D

resistivity inversion was performed with 3028 filtered apparent resistivity measurements using RES3DINV software (Loke and Dahlin, 2002) which adopts a smoothness-constrained least-squares algorithm (Loke and Barker, 1996). The resistivity tomogram shown on Fig. 50a has a 7.5 % RMS error after 5 iterations. The sensitivity map is given by the diagonal elements of $J^T J$ matrix and is shown in Fig. 51. Each element in the mesh contains the sum of the squared sensitivities of the data, obtained after the 5th iteration. Here, the sensitivity spatial distribution is related to the measurement configuration. Around electrodes, the sensitivity is closed to 1, which indicates a perfect accuracy. As the density of D-C measurement decreases at depth, the resolution and the sensitivity value both decline. However, the ERT cross section still shows a very good resolution up to 25-30 m depth (green and light blue in the Fig. 51) whereas at the bottom corner a lower resolution is observed. Therefore, looking at this sensitivity map, it appears that the interpretation of the electrical cross-section is valid.

The electrical conductivity can be written as the sum of the surface conductivity, which is prominent in the case of clay-rich minerals produced by hydrothermal alteration, and bulk conductivity, which in our case mainly depends on hydrothermal fluid saturation and temperature (Revil and Florsch, 2010). The CO₂ flux has been measured using the Accumulation Chamber Method (for details, see 57), whereas the soil temperature was recorded at 30 cm depth by using a type K thermocouple. Both measurements have been carried out at each electrode location during the electrical resistivity tomography survey. The studied area includes the second largest diffuse degassing spot at Solfatara after the fumarolic area, with CO₂ flux values ranging from 700 to 10000 g.m⁻².day⁻¹. This high CO₂ flux anomaly is accompanied by a significant thermal anomaly, with soil temperature up to 80°C at 30 cm depth, due to the latent heat transfer that occurs during steam condensation at the surface.

The resistivity values of the SW-NE cross-section range between 1.5 and 20 Ωm, thus indicating a globally conductive subsurface for Solfatara (Fig. 50a), in agreement with the previous results (Bruno et al., 2007; Byrdina et al. 2014). The model clearly highlights a sharp horizontal contrast between a resistive structure (20Ωm) beneath the eastern part of the cross section and a conductive body (< 5 Ωm) on the western part, towards the liquid-saturated Fangaia mud pool.

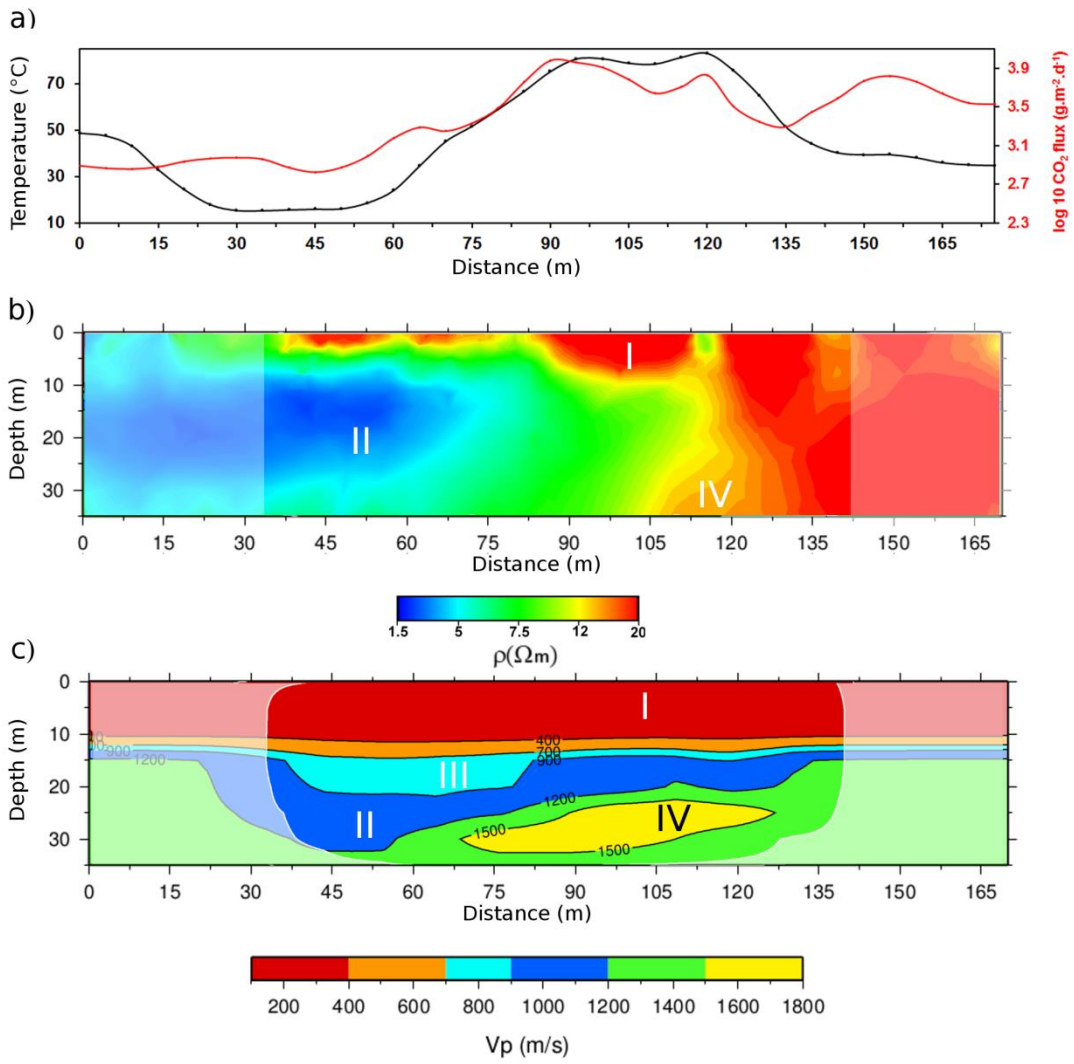


Figure 49. Comparison between temperature (black line) and CO₂ flux (red line) in a), resistivity cross section in b) and P-wave velocity model projected onto the cross-section D in Fig. 3a in c).

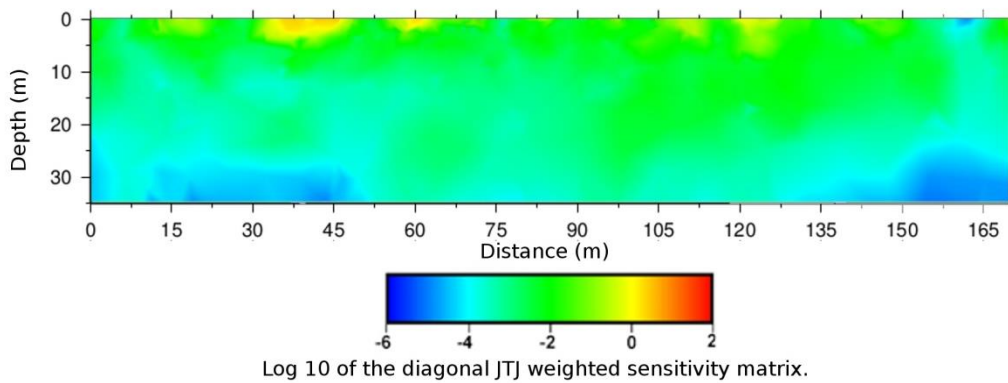


Figure 50. ERT sensitivity. The diagonal JTJ matrix shows the sensitivity of the bulk electrical conductivity values with respect to the data. This cross section shows a very good resolution up to 25-30 m depth (green and light blue in the figure) whereas at the bottom corner a lower resolution is observed.

With reference to Fig. 50c, the superficial layer “I”, with a P-wave velocity lower than 700 m/s, can be related to the shallow resistive zone “I” in Fig. 50b, with resistivity $\rho > 12 \Omega\text{m}$, located at the top of the resistivity section. The same resistive upper layer was obtained by Byrdina et al. (2014), and can be interpreted as unsaturated recent deposits (Bruno et al., 2007; Isaia et al., 2014). This layer is affected by a high CO_2 degassing (Fig. 50a), higher than $1000 \text{ g}\cdot\text{m}^{-2}\cdot\text{d}^{-1}$, and by an elevated surface temperature ($> 40 \text{ }^\circ\text{C}$, Fig. 50a). A passive seismic survey performed by Letort et al (2012) identified this area as the source of the ambient seismic noise generated by hydrothermal processes. The 3D velocity sections (Fig. 46b) allow to delineate this layer, which extends through the entire central area of the crater.

The second layer “II” shows P-velocity values ranging from 900 m/s to 1200 m/s and is about 10-m thick. It progressively deepens toward the SW part of the crater, becoming shallower at the interface with the mud pool (Fig. 50c). This structure corresponds to the eastern part of Fangaia, an area saturated with mineralized liquids (Byrdina et al., 2014). Here, the resistivity image shows a body saturated with conductive liquid “II” at 10-30 m (Fig. 50b), with $\rho < 5 \Omega \text{ m}$, getting deeper in the Fangaia direction like the velocity layer “II”. The slope of the liquid-saturated body is explained by a pronounced influence of local topography (Byrdina et al., 2014).

On these grounds, we suggest that steam condensation is produced on the eastern part (“IV” and above) in a gas dominated structure that is characterized by both high diffuse degassing and high surface temperature. This steam produces hot condensate water which is channelled within the “II” layer and finally reaches the Fangaia mud pool in the western part.

This fluid directionality is also inferred from the Self-Potential mapping by Byrdina et al. (2014). Indeed, in their paper Self Potential anomalies decrease from -40 mV in the eastern part to -100 mV in the Fangaia area. In a volcanic area the streaming potential is the main source of current. It is associated with the drag of the excess of charge in the pore water of fluids. Consequently, above the isoelectric point of pH (which is the case in the Fangaia survey, with a soil pH above 5), an advective flow can be inferred from a decrease of the streaming potential.

In Fig. 4c the low velocity anomaly “III”, with values between 700 and 900 m/s, is characterized by the same conductive properties already described for the body “II” in Fig. 4a. There, we expect to find a region saturated with the liquid flow of the Fangaia area. However, inasmuch this body has velocity values lower than the “II” layer, we suggest, in agreement

with the lithology (Isaia et al., 2015), that it is composed by less consolidated tephra sediments than the layer “II”. Therefore the velocity variation between the “III” and the “II” zone may identify a gentle discontinuity in the degree of consolidation of rocks.

The shape of this anomaly, which has the maximum extension in the central area and decreases going towards the NW and SE directions (Fig. 46b), could be due to the accumulation of deposit materials in a low of the most compact layer “II” .

The previous results are in agreement with what was found in Serra et al. (2016). The retrieved 3D S-wave velocity model, obtained from a combination of 1D velocity model in array sub-grid and resolved up to 15 m, showed two main domains: the S-W one, closest to the Fangaia, is slower than the N-E one. This feature is common to all the depths. The authors, in order to interpret the low S-wave velocity domain at SW, qualitatively hypothesized a manifestation of an unconsolidated layer at shallow depths and one of a water aquifer at greater depths. The P-wave velocity model obtained in this work not only has a much higher resolution, but also covers an area that is about twice the one of the S-wave velocity model obtained by Serra et al. (2016). These features allowed us to be in agreement with the previously found results. but above all to considerably increase the knowledge and characterization of the deeper anomalies of the Solfatara complex hydrothermal system. In particular, the water aquifer, mentioned by Serra et al. (2016), is imaged and better characterized through the interpretation of layer “II”, located at 15-20 m depth.

Finally, we will try to interpret the high velocity anomaly “IV” in Fig. 4c. It is located between 25 and 30 m depths and it constitutes a novelty with respect to the S-wave velocity model by Serra et al. (2016) since no resolution was achieved in this cited work. This high velocity anomaly is characterized by values that range between 1500 and 1800 m/s, and partially overlaps a zone with resistivity values higher than 12 Ω m. This high-resistivity/high-velocity body appears at the beginning of the degassing structure (Stufe di Nerone, SN in Fig. 1) on the eastern border of Solfatara crater, where major NW-SE directed fractures (Isaia et al., 2015) enhance the up-flow of the water steam and the CO₂ flux. This interpretation is consistent with the high CO₂ flux and ground temperature measured in the same area (Byrdina et al., 2014).

From the resistivity images (Fig. 50b) it can be clearly seen that the conduit of the rising gas plume on the NE direction is located where the “II” layer saturated with condensed water is thinner (Fig 50c). Therefore, the anomaly found in our velocity images can represent an area of gas accumulation, trapped by the liquid saturated “II” layer, located immediately above and not completely resolved by the resistivity images due to its location below a conductive area.

The velocity tomographic model obtained for the Solfatara allows to image with a high resolution the shallow area of the crater and to understand the processes taking place inside. These processes are part of a complex dynamics triggered by the interaction between structural patterns and degassing within shallow hydrothermal circulation cells. Then, at the shallow investigated depths, we can see the effect of deep processes affecting the caldera, and our investigated area can be interpreted as the surface evidence of deeper processes.

3.3.5 Conclusion

The importance of this work lies in these principal aspects:

1. The Solfatara crater represents one of the main pressure release areas of the entire Campi Flegrei volcanic system, considering the impressive magnitude of the diffuse degassing process. From this arises the growing interest for the knowledge of this area, especially with the aim of assessing the level of potential danger characterizing this crater of the Campi Flegrei volcanic complex;
2. the 3D tomographic survey allows to achieve an unprecedented spatial detail on the shallow velocity structure of the central part of the Solfatara crater. The 3d high-resolution tomographic images allow to better understand, in terms of velocity anomalies and fluid type, the complex hydrothermal processes into the shallow part (30-35 m) of the volcano;
3. the procedure used in this work represents a new multi-parametric approach that can be used in a volcanic environment; showing how the interpretation of velocity tomographic images can be complemented with the one obtained by stratigraphic analysis and resistivity profiles, and, most of all, how this joint interpretation leads to a more robust and reliable interpretation of complex hydrothermal system;
4. the complex interactions (deep fluids, hydrothermal system, geological structures) between deep and shallow sources and structures allows to use the shallow hydrothermal system processes as a constrain for the fluid migration processes occurring at depth.

Conclusion

The aim of this research project was to investigate the influence of physical parameters in dynamic processes during the preparatory phase of earthquakes (both natural and human-made), by tracking the seismicity, the propagation medium features and their temporal variation. Starting out with the idea that seismic waves contain information about rock composition and fluid content of the crossed medium, we used the seismic observable associated with them to reconstruct the **space** and **time changes** of **physical properties** (*velocity, attenuation, rock parameters*) in the investigated **complex geological media**: a *tectonic, volcanic and geothermal environments*.

The first part of this Thesis encloses the detailed description of the different *methodologies* analysed and developed in our research project. Because of that, this part can be seen as a *comprehensive and detailed compendium* of methods aimed to characterize the propagation medium in terms of its composition, geological structure and rheological behaviour.

For the purpose of image the **spatial variation** of the host environment physical properties and the effects of pore-fluid on them, seismic tomography has been introduced. We first showed how an iterative, linearized, tomographic approach in which the P and S arrival times are simultaneously inverted for the earthquakes location and velocity parameters (Latorre et al., 2004) can be used to retrieve accurate 3D velocity images of investigated areas and the related resolution. Then, we explained the procedure adopted to modify the velocity code in order to obtain the 3-D attenuation quality factor Q images using as data the t^* parameter. Finally, motivated by the aim of characterize the medium in terms of rock parameters, like porosity or saturation, we developed a rock physics modelling procedure based on Biot's theory (1956) that allows to estimate micro-scale properties through the direct comparison between observed and up-scaled velocity and attenuation parameters.

With regard to the **temporal changes** of physical properties within rock volumes, the *4D seismic tomography*, i.e. a 3D seismic tomography repeated in different time windows, can be introduced. We showed that a key requirement in 4D tomography is to ensure the same resolution of the 3D tomographic images in each analysed time epochs (Lumley et al. 1995; Lumley, 2001; Vesnaver et al., 2003). Moreover, when a permanent seismic acquisition network is available, the only equalization process concerns the different position of passive seismicity sources. For this purpose we developed a new equalization procedure in passive seismic for the 4D tomography. The detailed description of procedure operation proofs that the novelty lies not only in its ability to optimize the choice of time-windows in the case of

massive data-sets, but also in a complete handling of the issue associated to the seismic tomography, which includes the choice of inversion parameters, the choice of the optimal model parameterization (*multi-scale method*), the analysis of the model resolution, etc.

Beside the time-lapse tomography, we considered also “fast” methods that allows to track temporal changed of physical observables (in our case station location residuals and V_p/V_s ratio) in a shorter time than comprehensive method, that requires a long time-spam to record and elaborate consistent data-set. This choice was prompted by the results of several works showing the necessity of a better and fast monitoring of temporal variation of the elastic properties in order to mitigate the seismic hazard in highly vulnerable area (Chiarabba et al. 2009; Lucente et al 2010; Valoroso et al. 2011; Gritto et al., 2014).

Finally, in the last chapter of the PART I, regarding the methodologies, we presented a new probabilistic double-difference earthquake location method. Through several synthetic test performed by varying the source configuration, the velocity model and the data errors, we showed that the use of both differential-times as data, a probabilistic approach and a 3D velocity model, makes the resulting location high accurate. Therefore we provided a very useful tool to track with high accuracy **spatial and temporal changes of the seismicity pattern**, which, in turn, can be used to analyse the presence and diffusion of a pore-pressure perturbation in a fluid saturated medium (Nur and Booker, 1972; Hainzl, 2004; Antonioli et al., 2005;Hainzl and Ogata, 2005).

In the PART II of this Thesis we showed the results of the previous methodologies application to three complex areas: the Irpinia fault zones, The Geysers geothermal area and the Solfatara volcano. As we discussed, the relevance of these three areas lies not only in their different rheological and structural nature, but also in their different dimensional scale. For these different features we consider the areas as "seismological laboratories", to which we applied different methodologies according to the characteristics, the available data-sets, the associated problems and the state of art of each area. This enables us to validate the methodologies and to analyse their performance for different scenarios.

The first analysed area, was the **Irpinia fault zone** (Southern Italy), a crustal volume in southern Italy, embedding the still active fault system that generated the 1980 M 6.9 earthquake. Since different authors (De Matteis et al. 2012; Matrullo et al. 2013; Ascione et al., 2013; Amoroso et al. 2014) have showed that the low magnitude ($M_L < 3.5$) background seismicity does not occur on a single major fault, but rather in a volume delimited by the master faults of Irpinia earthquake, the first raised issue was the possibility to clusterize the

seismicity along the main faults using an accurate location method. Secondly, the 3D P- and S-wave velocity models optimized for the area (Amoroso et al. 2014), have highlighted a significant fluid accumulation in highly fractured rocks, where most of micro-seismicity occurs. The consequent interest was whether it was possible to deepen our knowledge of the complex area with attenuation images and to better characterize the ‘earthquake reservoir’ in terms of porosity, saturation or fluid type. These analysis have as final aim the possibility to make some *quantitative* consideration about the seismicity-triggering mechanism.

The first issue has been addressed by carrying out a high-resolution, earthquake location analysis of the Irpinia micro-seismicity by using the double-difference location method jointly to an accurate differential time data set. The refined seismicity locations show that the events occur in a volume delimited by the faults activated during the 1980 MS 6.9 Irpinia earthquake, accordingly with precedent works. The main result of our application is that we found an abrupt interruption of the seismicity across an SW–NE oriented structural discontinuity. This, interpreted as a geometrical barrier, could have played a key role during the 1980 Irpinia event, and possibly controlled the delayed times of activation of the first two rupture segments. In order to satisfy the second interest, we retrieved the 3-D attenuation structure of the normal fault system, in terms of quality factors Q_P and Q_S . The retrieved Q_S showed a good correlation with the geometrical features of large-scale geological structures. While Q_P showed a good correlation with the finer structure of the 1980 Irpinia earthquake.

Then, to infer quantitative information about rock physics parameters, we considered the rock physic up-scaling procedure previously described. By using a realistic rock-physics model, we constrained the porosity in the ranges 3-5%, high for the area, and consolidation in the range 6-10, correspondent to a pore-pressure up to about 150 MPa (de Ceia et al., 2015), with the presence of a fracture system, likely high saturated by brine-CO₂/CH₄ or CO₂-CH₄ mixtures, where the high pore pressure is directly responsible for the seismicity triggering mechanism and where, in fact, most of seismicity occurs.

Moving on to another area, we considered **The Geysers geothermal area** (California) which is the greatest Enhanced Geothermal System (EGS) in the world. The dominant interests for this area was to track spatial and temporal variations, on both short and long term, of the reservoir physics parameter. We were aware, in fact, that fluid injection, steam extraction and reservoir stimulation in EGS lead to induced seismicity (Eberhart-Phillips and Oppenheimer, 1984; Stark, 1990; Stark and Davies, 1996), whose monitoring is important for both the mitigation of the side effects of industrial operations, and the continuous assessment of the reservoir’s conditions. For this aim, the applied methodologies at The Geysers high quality data-set (acquired by a permanent seismic network) was the high-resolution seismic velocity

tomography, the V_p/V_s ratio temporal variations as a “fast” monitoring tool, and a preliminary analysis for the 4D tomography. The main results of our tomographic application are the good correlation between the V_p , V_s trend and the geothermal/geological characteristic of the reservoir and the high V_p/V_s ratio anomaly in correspondence of the high-temperature reservoir, where the most of the seismicity occurs. Concerning the “fast” monitoring tool, the presented results, in accordance with precedent works (Gunasekera et al., 2003; Gritto et al. 2014), showed that the V_p/V_s ratio is positively correlated to the temporal changes in the reservoir’s saturation. Thus, this observable can be used to estimate and possibly predict the large scale saturation changes in some areas of the reservoir, such as around injection wells, or throughout the whole reservoir. Finally, the obtained result of preliminary 4D tomography justified the planning of a complete 4D tomographic procedure. Once the well resolved and coherent 3D velocity images have been obtained for each epoch, the next step will be to interpret the changes in the obtained values and anomalies on the basis of reservoir operation, i.e. location, timing and rate of fluid injection, information on rock physics coming from modelling or laboratory measurements, etc.

Finally, we considered the volcanic area of the **Solfatara crater**, one of the main pressure release areas of the entire Campi Flegrei volcanic system, considering the impressive magnitude of the diffuse degassing process (Chiodini et al., 2001). From this arises the interest of assessing the level of potential danger characterizing this crater. In this frame, a repeated active seismic experiment was carried out between September 2013 and November 2014. From the data-set acquired during the first campaign, we obtained an ultra-high-resolution 3D reference velocity image of the shallow hydrothermal structure of the Solfatara crater’s central part (up to 35 m depth), by applying seismic tomography. Despite the very small scale of the investigated area (about 100 m), the multi-scale procedure enabled us to apply the tomographic method. In fact, this strategy does not depend on the scale of the application, provided that data have controlled uncertainty and sufficient resolution to retrieve unbiased model parameters. Then, aiming to improve the understanding of the hydrothermal system that feeds the surface phenomenon, we applied a multi-parametric approach by comparing our seismic tomography with 2D cross-sections of resistivity (ρ) and with temperature and CO₂ flux measurements. The results showed how this joint interpretation leads to a more robust knowledge of complex hydrothermal system.

The application of different methodologies to the three complex areas, chosen on the basis of open questions and of the state of art related to each one of them, allowed us to add an

important piece of information to the knowledge of the subsoil's structural characteristics and of its behaviour in relation to the presence and motion of pore fluids. These factors, obtained by tracking the seismicity, the propagation medium's features and their temporal variation, was correlated to the dynamic of the entire considered system, particularly in connection with the processes taking place during the enucleation phase of earthquakes. Thus, the obtained results showed how the described methodologies can be used in seismogenic and volcanic areas, to improve the knowledge of medium properties in order to mitigate the risk associated to destructive events; and in geothermal areas, to monitor the induced seismicity through the tracking of medium properties temporal variation.

Therefore, this thesis represents a useful tool for this kind of analyses, by providing a compendium of different methodologies applicable to complex areas characterized by a different physical nature and a different dimensional scale. Moreover, in the second part of this thesis, the applications to the different three complex areas allow to evaluate the performances and weaknesses of the methodologies, in order to choose the most suitable one in the case of interest.

References

- Adam, L., Batzle, M. and Brevik, I., 2006. Gassmann's fluid substitution and shear modulus variability in carbonates at laboratory seismic and ultrasonic frequencies. *Geophysics*, 71(6), pp.F173-F183.
- Aggarwal, Y.P., Sykes, L.R., Armbruster, J. and Sbar, M.L., 1973. Premonitory changes in seismic velocities and prediction of earthquakes. *Nature*, 241, pp.101-104.
- Aiuppa, A., Cannata, A., Cannavò, F., Di Grazia, G., Ferrari, F., Giudice, G., Gurrieri, S., Liuzzo, M., Mattia, M., Montalto, P. and Patanè, D., 2010. Patterns in the recent 2007–2008 activity of Mount Etna volcano investigated by integrated geophysical and geochemical observations. *Geochemistry, Geophysics, Geosystems*, 11(9). Akaike, H., 1974. A new look at the statistical model identification. *IEEE transactions on automatic control*, 19(6), pp.716-723.
- Aki, K. and Lee, W.H.K., 1976. Array using first p arrival times from local earthquakes. *Journal of Geophysical research*.
- Allen, R.V., 1978. Automatic earthquake recognition and timing from single traces. *Bulletin of the Seismological Society of America*, 68(5), pp.1521-1532.
- Al-Shukri, H.J. and Mitchell, B.J., 1990. Three-dimensional attenuation structure in and around the New Madrid seismic zone. *Bulletin of the Seismological Society of America*, 80(3), pp.615-632.
- Altan, B.S. and Aifantis, E.C., 1997. On some aspects in the special theory of gradient elasticity. *Journal of the Mechanical Behavior of Materials(UK)*, 8(3), pp.231-282.
- Amato, A. and Selvaggi, G., 1993. Aftershock location and P-velocity structure in the epicentral region of the 1980 Irpinia earthquake. *Annals of Geophysics*, 36(1).
- Amato, A., Alessandrini, B., Cimini, G., Frepoli, A. and Selvaggi, G., 1993. Active and remnant subducted slabs beneath Italy: evidence from seismic tomography. *Annali di geofisica*, 36(2).
- Amoroso, O., Maercklin, N. and Zollo, A., 2012. S-Wave Identification by Polarization Filtering and Waveform Coherence Analyses. *Bulletin of the Seismological Society of America*, 102(2), pp.854-861.
- Amoroso, O., Ascione, A., Mazzoli, S., Virieux, J. and Zollo, A., 2014. Seismic imaging of a fluid storage in the actively extending Apennine mountain belt, southern Italy. *Geophysical Research Letters*, 41(11), pp.3802-3809.
- Amoroso, O., G. De Landro, G. Russo and A. Zollo. 2015. 4D imaging of elastic/anelastic medium properties: application to the Geysers geothermal area. *Conference Paper AGIS Schatzalp Workshop on Induced Seismicity, Davos Schatzalp, Switzerland*.
- Amoroso, O., Russo, G., De Landro, G., Zollo, A., Garambois, S., Mazzoli, S., Parente, M. and J. Virieux. 2016a. From Velocity and Attenuation Tomographies to Rock Physical Modelling: Inferences on fluid-driven earthquake processes at the Irpinia fault system in Southern Italy. Under review on *Geophysical Research Letters*.
- Amoroso, O., Festa, G., Bruno, P. P., D'Auria, L., De Landro, G., Di Fiore, V., Gammaldi, S., Maraio, S., Pilz, M., Roux, P., Russo, G., Serlenga, V., Serra, M., Woith, H., Zollo, A. 2016b. Advanced tomographic method for volcanic structures. Submitted on the special Issue "Modern methods of Applied Geophysics

to the understanding of volcanic structures and dynamics" of the *Journal of Applied Geophysics*.

Antonoli, A., Piccinini, D., Chiaraluce, L. and Cocco, M., 2005. Fluid flow and seismicity pattern: Evidence from the 1997 Umbria-Marche (central Italy) seismic sequence. *Geophysical Research Letters*, 32(10).

Ascione, A., Mazzoli, S., Petrosino, P. and Valente, E., 2013. A decoupled kinematic model for active normal faults: Insights from the 1980, MS= 6.9 Irpinia earthquake, southern Italy. *Geological Society of America Bulletin*, 125(7-8), pp.1239-1259.

Aster, R.C. and Meyer, R.P., 1988. Three-dimensional velocity structure and hypocenter distribution in the Campi Flegrei caldera, Italy. *Tectonophysics*, 149(3-4), pp.195-218.

Auriault, J.L., Borne, L. and Chambon, R., 1985. Dynamics of porous saturated media, checking of the generalized law of Darcy. *The Journal of the Acoustical Society of America*, 77(5), pp.1641-1650.

Bannister, S., Fry, B., Reyners, M., Ristau, J. and Zhang, H., 2011. Fine-scale relocation of aftershocks of the 22 February Mw 6.2 Christchurch earthquake using double-difference tomography. *Seismological Research Letters*, 82(6), pp.839-845.

Battaglia, M., Troise, C., Obrizzo, F., Pingue, F. and De Natale, G., 2006. Evidence for fluid migration as the source of deformation at Campi Flegrei caldera (Italy). *Geophysical Research Letters*, 33(1).

Beall, J.J. and Wright, M.C., 2010. Southern extent of The Geysers high temperature reservoir based on seismic and geochemical evidence. *Geothermal Resources Council Transactions*, 34, pp.1199-1202.

Benz, H.M., Chouet, B.A., Dawson, P.B., Lahr, J.C., Page, R.A. and Hole, J.A., 1996. Three-dimensional P and S wave velocity structure of Redoubt Volcano, Alaska. *Journal of Geophysical Research: Solid Earth*, 101(B4), pp.8111-8128.

Berge, P., Hutchings, L., Wagoner, J. and Kasameyer, P., 2001. Rock Physics Interpretation of P-Wave Q and Velocity Structure, Geology, Fluids, and Fractures at the Southeast Portion of The Geysers Geothermal Reservoir. *TRANSACTIONS-GEOTHERMAL RESOURCES COUNCIL*, pp.383-390.

Bernard, P., and A. Zollo (1989), The Irpinia (Italy) 1980 earthquake: Detailed analysis of a complex normal faulting. *J. Geophys. Res.*, 94(B2), 1631–1647.

Berryman, J.G., 1980a. Long-wavelength propagation in composite elastic media I. Ellipsoidal inclusions. *The Journal of the Acoustical Society of America*, 68(6), pp.1820-1831.

Berryman, J.G., 1980b. Long-wavelength propagation in composite elastic media II. Ellipsoidal inclusions. *The Journal of the Acoustical Society of America*, 68(6), pp.1820-1831.

Bertani, R., 2012. Geothermal power generation in the world 2005–2010 update report. *Geothermics*, 41, pp.1-29.

Bianco, F., Del Pezzo, E., Saccorotti, G. and Ventura, G., 2004. The role of hydrothermal fluids in triggering the July–August 2000 seismic swarm at Campi Flegrei, Italy: evidence from seismological and mesostructural data. *Journal of Volcanology and Geothermal Research*, 133(1), pp.229-246.

Biot, M.A., 1956. Theory of propagation of elastic waves in a fluid-saturated porous solid. I. Low-frequency range. *The Journal of the acoustical Society of america*, 28(2), pp.168-178.

Boitnott, G.N. and Bonner, B.P., 1994, January. Characterization of rock for constraining reservoir scale tomography at the Geysers geothermal field. In *Proceedings, Nineteenth Workshop on Geothermal Reservoir Engineering* (pp. 18-20).

- Boncio, P., Lavecchia, G. and Pace, B., 2004. Defining a model of 3D seismogenic sources for Seismic Hazard Assessment applications: the case of central Apennines (Italy). *Journal of Seismology*, 8(3), pp.407-425.
- Boitnott, G.N. and Bonner, B.P., 1994, January. Characterization of rock for constraining reservoir scale tomography at the Geysers geothermal field. In *Proceedings, Nineteenth Workshop on Geothermal Reservoir Engineering* (pp. 18-20).
- Bosl, W.J. and Nur, A., 2002. Aftershocks and pore fluid diffusion following the 1992 Landers earthquake. *Journal of Geophysical Research: Solid Earth*, 107(B12).
- Brie, A., Pampuri, F., Marsala, A.F. and Meazza, O., 1995, January. Shear sonic interpretation in gas-bearing sands. In *SPE Annual Technical Conference and Exhibition*. Society of Petroleum Engineers.
- Brittle, K.F., Lines, L.R., and Dey, A.K., 2001. Vibroseis deconvolution: a comparison of cross-correlation and frequency-domain sweep deconvolution. *Geophys. Prosp.*, 49, 675-686.
- Brown, L.D., Chapin, C.E., Sanford, A.R., Kaufman, S. and Oliver, J., 1980. Deep structure of the Rio Grande rift from seismic reflection profiling. *Journal of Geophysical Research: Solid Earth*, 85(B9), pp.4773-4800.
- Bruno, P.P.G., Ricciardi, G.P., Petrillo, Z., Di Fiore, V., Troiano, A. and Chiodini, G., 2007. Geophysical and hydrogeological experiments from a shallow hydrothermal system at Solfatara Volcano, Campi Flegrei, Italy: Response to caldera unrest. *Journal of Geophysical Research: Solid Earth*, 112(B6).
- Burrige, R. and Keller, J.B., 1981. Poroelasticity equations derived from microstructure. *The Journal of the Acoustical Society of America*, 70(4), pp.1140-1146.
- Burrige, R. and Vargas, C.A., 1979. The fundamental solution in dynamic poroelasticity. *Geophysical Journal International*, 58(1), pp.61-90.
- Byrdina, S., Vandemeulebrouck, J., Cardellini, C., Legaz, A., Camerlynck, C., Chiodini, G., Lebourg, T., Gresse, M., Bascou, P., Motos, G. and Carrier, A., 2014. Relations between electrical resistivity, carbon dioxide flux, and self-potential in the shallow hydrothermal system of Solfatara (Phlegrean Fields, Italy). *Journal of volcanology and geothermal research*, 283, pp.172-182.
- Caine, J.S., Evans, J.P. and Forster, C.B., 1996. Fault zone architecture and permeability structure. *Geology*, 24(11), pp.1025-1028.
- Caliro, S., Chiodini, G., Moretti, R., Avino, R., Granieri, D., Russo, M. and Fiebig, J., 2007. The origin of the fumaroles of La Solfatara (Campi Flegrei, south Italy). *Geochimica et Cosmochimica Acta*, 71(12), pp.3040-3055.
- Castagna, J.P., Batzle, M.L. and Kan, T.K., 1993. Rock physics—The link between rock properties and AVO response. *Offset-dependent reflectivity—Theory and practice of AVO analysis: SEG*, 8, pp.135-171.
- Caudill, M., 1989. Neural nets primer, part VI. *AI Expert*, 4(2), pp.61-67.
- Cavanaugh, J. E., and Shumway, R. H. A bootstrap variant of AIC for state-space model selection. *Statistica Sinica*, 473-496(1997).
- Chiarabba, C., De Gori, P. and Boschi, E., 2009. Pore-pressure migration along a normal-fault system resolved by time-repeated seismic tomography. *Geology*, 37(1), pp.67-70.
- Chiaraluca, L., Valoroso, L., Piccinini, D., Di Stefano, R. and De Gori, P., 2011. The anatomy of the 2009 L'Aquila normal fault system (central Italy) imaged by high resolution foreshock and aftershock locations. *Journal of Geophysical Research: Solid Earth*, 116(B12).

- Chiodini, G., Todesco, M., Caliro, S., Del Gaudio, C., Macedonio, G. and Russo, M., 2003. Magma degassing as a trigger of bradyseismic events: The case of Phlegrean Fields (Italy). *Geophysical Research Letters*, 30(8).
- Chiodini, G., Cardellini, C., Amato, A., Boschi, E., Caliro, S., Frondini, F. and Ventura, G., 2004. Carbon dioxide Earth degassing and seismogenesis in central and southern Italy. *Geophysical Research Letters*, 31(7).
- Chiodini, G., D. Granieri, R. Avino, S. Caliro, A. Costa, and C. Werner (2005), Carbon dioxide diffuse degassing and estimation of heat release from volcanic and hydrothermal systems, *J. Geophys. Res.*, 110, B08204.
- Chiodini, G., 2009. CO₂/CH₄ ratio in fumaroles a powerful tool to detect magma degassing episodes at quiescent volcanoes. *Geophysical Research Letters*, 36(2).
- Chopra, S. and Marfurt, K.J., 2007. *Seismic attributes for prospect identification and reservoir characterization*. Society of Exploration Geophysicists and European Association of Geoscientists and Engineers.
- Ciotoli, G., Bigi, S., Tartarello, C., Sacco, P., Lombardi, S., Ascione, A. and Mazzoli, S., 2014. Soil gas distribution in the main coseismic surface rupture zone of the 1980, Ms= 6.9, Irpinia earthquake (southern Italy). *Journal of Geophysical Research: Solid Earth*, 119(3), pp.2440-2461.
- Cocco, M., Chiarabba, C., Di Bona, M., Selvaggi, G., Margheriti, L., Frepoli, A., Lucente, F.P., Basili, A., Jongmans, D. and Campillo, M., 1999. The April 1996 Irpinia seismic sequence: evidence for fault interaction. *Journal of seismology*, 3(1), pp.105-117.
- Coco, A., Gottsmann, J., Whitaker, F., Rust, A., Currenti, G., Jasim, A. and Bunney, S., 2016. Numerical models for ground deformation and gravity changes during volcanic unrest: simulating the hydrothermal system dynamics of a restless caldera. *Solid Earth*, 7(2), p.557.
- Convertito, V., Maercklin, N., Sharma, N. and Zollo, A., 2012. From induced seismicity to direct time-dependent seismic hazard. *Bulletin of the Seismological Society of America*, 102(6), pp.2563-2573.
- Cox, D.T., Kobayashi, N. and Okayasu, A., 1995. Vertical variations of fluid velocities and shear stress in surf zones. In *Coastal Engineering 1994* (pp. 98-112).
- Cusano, P., Petrosino, S. and Saccorotti, G., 2008. Hydrothermal origin for sustained long-period (LP) activity at Campi Flegrei volcanic complex, Italy. *Journal of Volcanology and Geothermal Research*, 177(4), pp.1035-1044.
- d'Agostino, N., Jackson, J.A., Dramis, F. and Funicello, R., 2001. Interactions between mantle upwelling, drainage evolution and active normal faulting: an example from the central Apennines (Italy). *Geophysical Journal International*, 147(2), pp.475-497.
- Dai, H. and MacBeth, C., 1997. The application of back-propagation neural network to automatic picking seismic arrivals from single-component recordings. *Journal of Geophysical Research: Solid Earth*, 102(B7), pp.15105-15113.
- Davis, T.L. and Benson, R.D., 2001. Monitoring production processes by 4-D multicomponent seismic surveys at Vacuum Field, New Mexico. In *SEG Technical Program Expanded Abstracts 2001* (pp. 1616-1618). Society of Exploration Geophysicists.
- de Ceia, M.A., Misságia, R.M., Neto, I.L. and Archilha, N., 2015. Relationship between the consolidation parameter, porosity and aspect ratio in microporous carbonate rocks. *Journal of Applied Geophysics*, 122, pp.111-121.
- De Landro, G., Amoroso, O., Stabile, T.A., Matrullo, E., Lomax, A. and Zollo, A., 2015. High-precision differential earthquake location in 3-D models: evidence for a rheological barrier controlling the

microseismicity at the Irpinia fault zone in southern Apennines. *Geophysical Journal International*, 203(3), pp.1821-1831.

De Landro, G., Amoroso, O., Russo, G., Zollo, A. High resolution 3D imaging of the Irpinia active fault zone part 2: Modelling of rock physical properties. *European Seismological Commission 35th General Assembly*. ESC2016-317-1, Vienna (2016).

Lorenzo, S., Zollo, A. and Mongelli, F., 2001. Source parameters and three-dimensional attenuation structure from the inversion of microearthquake pulse width data: Qp imaging and inferences on the thermal state of the Campi Flegrei caldera (southern Italy). *Journal of Geophysical Research: Solid Earth*, 106(B8), pp.16265-16286.

De Luca, G., Scarpa, R., Filippi, L., Gorini, A., Marcucci, S., Marsan, P., Milana, G. and Zambonelli, E., 2000. A detailed analysis of two seismic sequences in Abruzzo, Central Apennines, Italy. *Journal of Seismology*, 4(1), pp.1-21.

De Matteis, R., Matrullo, E., Rivera, L., Stabile, T.A., Pasquale, G. and Zollo, A., 2012. Fault delineation and regional stress direction from the analysis of background microseismicity in the southern Apennines, Italy. *Bulletin of the Seismological Society of America*, 102(4), pp.1899-1907.

De Natale, G., Pingue, F., Allard, P. and Zollo, A., 1991. Geophysical and geochemical modelling of the 1982–1984 unrest phenomena at Campi Flegrei caldera (southern Italy). *Journal of Volcanology and Geothermal Research*, 48(1-2), pp.199-222.

De Siena, L., Del Pezzo, E. and Bianco, F., 2010. Seismic attenuation imaging of Campi Flegrei: Evidence of gas reservoirs, hydrothermal basins, and feeding systems. *Journal of Geophysical Research: Solid Earth*, 115(B9).

De Vivo, B., Rolandi, G., Gans, P.B., Calvert, A., Bohrsen, W.A., Spera, F.J. and Belkin, H.E., 2001. New constraints on the pyroclastic eruptive history of the Campanian volcanic Plain (Italy). *Mineralogy and Petrology*, 73(1-3), pp.47-65.

Del Gaudio, C., Aquino, I., Ricciardi, G.P., Ricco, C. and Scandone, R., 2010. Unrest episodes at Campi Flegrei: A reconstruction of vertical ground movements during 1905–2009. *Journal of Volcanology and Geothermal Research*, 195(1), pp.48-56.

Di Bucci, D., Ravaglia, A., Seno, S., Toscani, G., Fracassi, U. and Valensise, G., 2006. Seismotectonics of the southern Apennines and Adriatic foreland: Insights on active regional E-W shear zones from analogue modelling. *Tectonics*, 25(4).

Di Luccio, F., Fukuyama, E. and Pino, N.A., 2005. The 2002 Molise earthquake sequence: What can we learn about the tectonics of southern Italy?. *Tectonophysics*, 405(1), pp.141-154.

Di Stefano, R., Chiarabba, C., Chiaraluce, L., Cocco, M., De Gori, P., Piccinini, D. and Valoroso, L., 2011. Fault zone properties affecting the rupture evolution of the 2009 (Mw 6.1) L'Aquila earthquake (central Italy): Insights from seismic tomography. *Geophysical Research Letters*, 38(10).

Diehl, T., Deichmann, N., Kissling, E. and Husen, S., 2009. Automatic S-wave picker for local earthquake tomography. *Bulletin of the Seismological Society of America*, 99(3), pp.1906-1920.

Dodge, D.A., Beroza, G.C. and Ellsworth, W.L., 1995. Foreshock sequence of the 1992 Landers, California, earthquake and its implications for earthquake nucleation. *Journal of Geophysical Research: Solid Earth*, 100(B6), pp.9865-9880.

Domenico, S.N., 1976. Effect of brine-gas mixture on velocity in an unconsolidated sand reservoir. *Geophysics*, 41(5), pp.882-894.

- Duputel, Z., Ferrazzini, V., Brenguier, F., Shapiro, N., Campillo, M. and Nercessian, A., 2009. Real time monitoring of relative velocity changes using ambient seismic noise at the Piton de la Fournaise volcano (La Réunion) from January 2006 to June 2007. *Journal of Volcanology and Geothermal Research*, 184(1), pp.164-173.
- Dupuy, B., Garambois, S. and Virieux, J., 2016. Estimation of rock physics properties from seismic attributes—Part 1: Strategy and sensitivity analysis. *Geophysics*, 81(3), pp.M35-M53.
- Dvorkin, J., Mavko, G. and Nur, A., 1995. Squirt flow in fully saturated rocks. *Geophysics*, 60(1), pp.97-107.
- Dvorkin, J., Mavko, G. and Nur, A., 1999. Overpressure detection from compressional-and shear-wave data. *Geophysical Research Letters*, 26, pp.3417-3420.
- Dvorkin, J., Helgerud, M.B., Waite, W.F., Kirby, S.H. and Nur, A., 2000. Introduction to physical properties and elasticity models. In *Natural Gas Hydrate* (pp. 245-260). Springer Netherlands.
- Eastwood, J., Johnston, D., Huang, X., Craft, K. and Workman, R., 1998. Processing for robust time-lapse seismic analysis: Gulf of Mexico example, Lena field. In *SEG Technical Program Expanded Abstracts 1998* (pp. 20-23). Society of Exploration Geophysicists.
- Eberhart-Phillips, D. and Oppenheimer, D.H., 1984. Induced seismicity in The Geysers geothermal area, California. *Journal of Geophysical Research: Solid Earth*, 89(B2), pp.1191-1207.
- Eberhart-Phillips, D., 1986. Three-dimensional velocity structure in northern California Coast Ranges from inversion of local earthquake arrival times. *Bulletin of the Seismological Society of America*, 76(4), pp.1025-1052.
- Ebrom, D., Nolte, B., Purnell, G., Sukup, D. and Krail, P., 1998. Analysis of multicomponent seismic data from offshore Gulf of Mexico. In *SEG Technical Program Expanded Abstracts 1998* (pp. 162-165). Society of Exploration Geophysicists.
- Ehrenberg, S.N. and Nadeau, P.H., 2005. Sandstone vs. carbonate petroleum reservoirs: A global perspective on porosity-depth and porosity-permeability relationships. *AAPG bulletin*, 89(4), pp.435-445.
- Ekstrom, B., Jacobson, G., Ohman, O. and Sjodin, H., Pharmacia Biosensor Ab, 1994. *Microfluidic structure and process for its manufacture*. U.S. Patent 5,376,252.
- Elliott, S.E. and Wiley, B.F., 1975. Compressional velocities of partially saturated, unconsolidated sands. *Geophysics*, 40(6), pp.949-954.
- Ellsworth, W.L. and Beroza, G.C., 1995. Seismic evidence for an earthquake nucleation phase. *Science*, 268(5212), p.851.
- A. Emolo, N. Maercklin, E. Matrullo, A. Orefice, O. Amoroso, V. Convertito, A. Zollo. (2012). S43D-2500: Analysis of induced seismicity at The Geysers geothermal field, California. *Conference Paper*. AGU Fall Meeting, American Geophysical Union, At San Francisco, California.
- Emolo, A., Convertito, V. and Cantore, L., 2010. Ground-motion predictive equations for low-magnitude earthquakes in the Campania–Lucania area, Southern Italy. *Journal of Geophysics and Engineering*, 8(1), p.46.
- Evans, J.R. and Zucca, J.J., 1993. Active source, high-resolution (NeHT) tomography: velocity and Q. *Seismic Tomography: Theory and Practice*, pp.695-732.
- Fahlman, S.E. and Lebiere, C., 1990. The cascade-correlation learning architecture.

- Foulger, G.R., Julian, B.R., Pitt, A.M., Hill, D.P., Malin, P.E. and Shalev, E., 2003. Three-dimensional crustal structure of Long Valley caldera, California, and evidence for the migration of CO₂ under Mammoth Mountain. *Journal of Geophysical Research: Solid Earth*, 108(B3).
- Frank, F.C., 1965. On dilatancy in relation to seismic sources. *Reviews of Geophysics*, 3(4), pp.485-503.
- Gaeta, F. S., De Natale, G., Peluso, F., Mastrolorenzo, G., Castagnolo, D., Troise, C., Pingue, F., Mita, D.G. and Rossano, S. 1998. Genesis and evolution of unrest episodes at Phlegraean Fields caldera: the role of the thermal fluid dynamical processes in the geothermal system. *J. Geophys. Res.* **103**, 20,921–20,933.
- Galadini, F. and Galli, P., 1999. The Holocene paleoearthquakes on the 1915 Avezano earthquake faults (central Italy): implications for active tectonics in the central Apennines. *Tectonophysics*, 308(1), pp.143-170.
- Gassmann, F., 1951. Elastic waves through a packing of spheres. *Geophysics*, 16(4), pp.673-685.
- Gomberg, J.S., Shedlock, K.M. and Roecker, S.W., 1990. The effect of S-wave arrival times on the accuracy of hypocenter estimation. *Bulletin of the Seismological Society of America*, 80(6A), pp.1605-1628.
- Got, J.L., Fréchet, J. and Klein, F.W., 1994. Deep fault plane geometry inferred from multiplet relative. *Journal of Geophysical research*, 99(94), pp.375-386.
- Grasso, J.R. and Wittlinger, G., 1990. Ten years of seismic monitoring over a gas field. *Bulletin of the Seismological Society of America*, 80(2), pp.450-473.
- Gritto, R. and Jarpe, S.P., 2014. Temporal variations of V P/V S-ratio at The Geysers geothermal field, USA. *Geothermics*, 52, pp.112-119.
- Guerin, G., He, W., Anderson, R.N., Xu, L. and Mello, U.T., 2000, January. Optimization of Reservoir Simulation and Petrophysical Characterization in 4D Seismic. In *Offshore Technology Conference*. Offshore Technology Conference.
- Gunasekera, R.C., Foulger, G.R. and Julian, B.R., 2003. Reservoir depletion at The Geysers geothermal area, California, shown by four-dimensional seismic tomography. *Journal of Geophysical Research: Solid Earth*, 108(B3).
- Gunasekera, R.C., Foulger, G.R. and Julian, B.R., 2003. Reservoir depletion at The Geysers geothermal area, California, shown by four-dimensional seismic tomography. *Journal of Geophysical Research: Solid Earth*, 108(B3).
- Gupta, H.K., Ward, R.W. and Lin, T.L., 1982. Seismic wave velocity investigation at The Geysers-Clear Lake geothermal field, California. *Geophysics*, 47(5), pp.819-824.
- Hainzl, S., 2004. Seismicity patterns of earthquake swarms due to fluid intrusion and stress triggering. *Geophysical Journal International*, 159(3), pp.1090-1096.
- Hainzl, S. and Ogata, Y., 2005. Detecting fluid signals in seismicity data through statistical earthquake modelling. *Journal of Geophysical Research: Solid Earth*, 110(B5).
- Hainzl, S., 2004. Seismicity patterns of earthquake swarms due to fluid intrusion and stress triggering. *Geophysical Journal International*, 159(3), pp.1090-1096.
- Hamada, G.M., 2004. Reservoir fluids identification using Vp/Vs ratio?. *Oil & Gas Science and Technology*, 59(6), pp.649-654.
- Han, D.H., Nur, A. and Morgan, D., 1986. Effects of porosity and clay content on wave velocities in sandstones. *Geophysics*, 51(11), pp.2093-2107.

- Hantschel, T. and Kauerauf, A.I., 2009. *Fundamentals of basin and petroleum systems modelling*. Springer Science & Business Media.
- Hainzl, S. and Ogata, Y., 2005. Detecting fluid signals in seismicity data through statistical earthquake modelling. *Journal of Geophysical Research: Solid Earth*, 110(B5).
- Hardebeck, J.L. and Hauksson, E., 1999. Role of fluids in faulting inferred from stress field signatures. *Science*, 285(5425), pp.236-239.
- Hardebeck, J.L., 2006. Homogeneity of small-scale earthquake faulting, stress, and fault strength. *Bulletin of the Seismological Society of America*, 96(5), pp.1675-1688.
- Harris, A., Dehn, J., Patrick, M., Calvari, S., Ripepe, M. and Lodato, L., 2005. Lava effusion rates from hand-held thermal infrared imagery: an example from the June 2003 effusive activity at Stromboli. *Bulletin of Volcanology*, 68(2), pp.107-117.
- Hauksson, E. and Shearer, P.M., 2006. Attenuation models (QP and QS) in three dimensions of the southern California crust: Inferred fluid saturation at seismogenic depths. *Journal of Geophysical Research: Solid Earth*, 111(B5).
- Ho-Liu, P., Kanamori, H. and Clayton, R.W., 1988. Applications of attenuation tomography to Imperial Valley and Coso-Indian Wells region, southern California. *Journal of Geophysical Research: Solid Earth*, 93(B9), pp.10501-10520.
- Husen, S. and Kissling, E., 2001. Postseismic fluid flow after the large subduction earthquake of Antofagasta, Chile. *Geology*, 29(9), pp.847-850.
- Husen, S., Taylor, R., Smith, R.B. and Healsler, H., 2004. Changes in geyser eruption behavior and remotely triggered seismicity in Yellowstone National Park produced by the 2002 M 7.9 Denali fault earthquake, Alaska. *Geology*, 32(6), pp.537-540.
- Iannaccone, G., Zollo, A., Elia, L., Convertito, V., Satriano, C., Martino, C., Festa, G., Lancieri, M., Bobbio, A., Stabile, T.A. and Vassallo, M., 2010. A prototype system for earthquake early-warning and alert management in southern Italy. *Bulletin of Earthquake Engineering*, 8(5), pp.1105-1129.
- Improta, L., Zollo, A., Bruno, P.P., Herrero, A. and Villani, F., 2003. High-resolution seismic tomography across the 1980 (Ms 6.9) Southern Italy earthquake fault scarp. *Geophysical research letters*, 30(10).
- Improta, L., De Gori, P. and Chiarabba, C., 2014. New insights into crustal structure, Cenozoic magmatism, CO₂ degassing, and seismogenesis in the southern Apennines and Irpinia region from local earthquake tomography. *Journal of Geophysical Research: Solid Earth*, 119(11), pp.8283-8311.
- Inversi, B., Scrocca, D., Montegrossi, G., Livani, M., Petracchini, L., Brandano, M., Brillì, M., Giustini, F., Recanati, R., Gola, G. and Polemio, M., 2013. 3D geological modelling of a fractured carbonate reservoir for the study of medium enthalpy geothermal resource in the Southern Apennines (Campania Region, Italy). In *Extended abstract, European Geothermal Congress*.
- Isaia, R., Vitale, S., Di Giuseppe, M.G., Iannuzzi, E., Tramparulo, F.D.A. and Troiano, A., 2015. Stratigraphy, structure, and volcano-tectonic evolution of Solfatara maar-diatreme (Campi Flegrei, Italy). *Geological Society of America Bulletin*, 127(9-10), pp.1485-1504.
- Johnston, D.H., Eastwood, J.E., Shyeh, J.J., Vauthrin, R., Khan, M. and Stanley, L.R., 2000. Using legacy seismic data in an integrated time-lapse study: Lena Field, Gulf of Mexico. *The Leading Edge*, 19(3), pp.294-302.
- Johnston, D.H., Toksöz, M.N. and Timur, A., 1979. Attenuation of seismic waves in dry and saturated rocks: II. Mechanisms. *Geophysics*, 44(4), pp.691-711.
- Julian, B.R. and Foulger, G.R., 2010. Time-dependent seismic tomography. *Geophysical Journal International*, 182(3), pp.1327-1338.

- Julian, B.R., Pitt, A.M. and Foulger, G.R., 1998. Seismic image of a CO₂ reservoir beneath a seismically active volcano. *Geophysical Journal International*, 133(1), pp.F7-F10.
- Kanamori, H., 2005. Real-time seismology and earthquake damage mitigation. *Annu. Rev. Earth Planet. Sci.*, 33, pp.195-214.
- Kirkpatrick, A., Peterson, J.E. and Majer, E.L., 1997. Three-dimensional compressional and shear-wave seismic velocity models for the Southeast Geysers geothermal field, California. In *Proceedings, 22nd Stanford Workshop on Geothermal Reservoir Engineering* (pp. 399-410).
- Kisslinger, C. and Engdahl, E.R., 1973. The interpretation of the Wadati diagram with relaxed assumptions. *Bulletin of the Seismological Society of America*, 63(5), pp.1723-1736.
- Kisslinger, C., 1975. Processes during the Matsushiro, Japan, earthquake swarm as revealed by leveling, gravity, and spring-flow observations. *Geology*, 3(2), pp.57-62.
- Kjartansson, E. and Denlinger, R., 1977, September. Seismic wave attenuation due to thermal relaxation in porous media. In *47th Annual International SEG Meeting*.
- Landrø, M., Solheim, O.A., Hilde, E., Ekren, B.O. and Strønen, L.K., 1999. The Gullfaks 4D seismic study. *Petroleum Geoscience*, 5(3), pp.213-226.
- Latorre, D., Virieux, J., Monfret, T., Monteiller, V., Vanorio, T., Got, J.L. and Lyon-Caen, H., 2004. A new seismic tomography of Aigion area (Gulf of Corinth, Greece) from the 1991 data set. *Geophysical Journal International*, 159(3), pp.1013-1031.
- Latorre, D., Amato, A. and Chiarabba, C., 2010. High-resolution seismic imaging of the Mw5. 7, 2002 Molise, southern Italy, earthquake area: Evidence of deep fault reactivation. *Tectonics*, 29(4).
- Lee, T.C. and Delaney, P.T., 1987. Frictional heating and pore pressure rise due to a fault slip. *Geophysical Journal International*, 88(3), pp.569-591.
- Lee, M.W., 2005. *Proposed moduli of dry rock and their application to predicting elastic velocities of sandstones* (No. 2005-5119).
- Letort, J., Roux, P., Vandemeulebrouck, J., Coutant, O., Cros, E., Wathelet, M., Cardellini, C. and Avino, R., 2012. High-resolution shallow seismic tomography of a hydrothermal area: application to the Solfatara, Pozzuoli. *Geophysical Journal International*, 189(3), pp.1725-1733.
- Lin, G. and Shearer, P.M., 2009. Evidence for water-filled cracks in earthquake source regions. *Geophysical Research Letters*, 36(17).
- Loke, M.H. and Barker, R.D., 1996. Rapid least-squares inversion of apparent resistivity pseudosections by a quasi-Newton method. *Geophysical prospecting*, 44(1), pp.131-152.
- Loke, M.H. and Dahlin, T., 2002. A comparison of the Gauss-Newton and quasi-Newton methods in resistivity imaging inversion. *Journal of Applied Geophysics*, 49(3), pp.149-162.
- Lomax, A., Virieux, J., Volant, P. and Berge-Thierry, C., 2000. Probabilistic earthquake location in 3D and layered models. In *Advances in seismic event location* (pp. 101-134). Springer Netherlands.
- Lomax, A., Michelini, A. and Curtis, A., 2009. Earthquake Earthquake Location Earthquake location, Direct, Global-Search Global-search Methods. In *Encyclopedia of complexity and systems science* (pp. 2449-2473). Springer New York.
- Lucente, F.P., De Gori, P., Margheriti, L., Piccinini, D., Di Bona, M., Chiarabba, C. and Agostinetti, N.P., 2010. Temporal variation of seismic velocity and anisotropy before the 2009 MW 6.3 L'Aquila earthquake, Italy. *Geology*, 38(11), pp.1015-1018.

- Lumley, D.E., 1995. *Seismic time-lapse monitoring of subsurface fluid flow* (No. 91). Stanford University.
- Lumley, D.E., 2001. Time-lapse seismic reservoir monitoring. *Geophysics*, 66(1), pp.50-53.
- Lutter, W.J., Nowack, R.L. and Braile, L.W., 1990. Seismic imaging of upper crustal structure using travel times from the PASSCAL Ouachita experiment. *J. geophys. Res*, 95, pp.4621-4631.
- Majer, E.L. and McEvilly, T.V., 1979. Seismological investigations at The Geysers geothermal field. *Geophysics*, 44(2), pp.246-269.
- Majer, E.L. and Peterson, J.E., 2007. The impact of injection on seismicity at The Geysers, California Geothermal Field. *International Journal of Rock Mechanics and Mining Sciences*, 44(8), pp.1079-1090.
- Majer, E.L., Baria, R., Stark, M., Oates, S., Bommer, J., Smith, B. and Asanuma, H., 2007. Induced seismicity associated with enhanced geothermal systems. *Geothermics*, 36(3), pp.185-222.
- Matrullo, E., De Matteis, R., Satriano, C., Amoroso, O. and Zollo, A., 2013. An improved 1-D seismic velocity model for seismological studies in the Campania–Lucania region (Southern Italy). *Geophysical Journal International*, 195(1), pp.460-473.
- Mavko, G., Mukerji, T. and Dvorkin, J., 2009. *The rock physics handbook: Tools for seismic analysis of porous media*. Cambridge university press.
- Mavko, G.M. and Nur, A., 1979. Wave attenuation in partially saturated rocks. *Geophysics*, 44(2), pp.161-178.
- Maxwell, S.C., Rutledge, J., Jones, R. and Fehler, M., 2010. Petroleum reservoir characterization using downhole microseismic monitoring. *Geophysics*, 75(5), pp.75A129-75A137.
- Majer, E.L., Baria, R., Stark, M., Oates, S., Bommer, J., Smith, B. and Asanuma, H., 2007. Induced seismicity associated with enhanced geothermal systems. *Geothermics*, 36(3), pp.185-222.
- McNitt, J. R., Henneberger, R. C., Koenig, J. B. and Robertson-Tait, A. (1989) Stratigraphic and structural controls of the occurrence of steam at The Geysers. *Geotherm. Resour. Coun. Trans.* 13,461-465.
- Menke, W., 1989. Discrete inverse theory.
- Michael, A.J. and Eberhart-Phillips, D., 1991. Relations among fault behavior, subsurface geology, and three-dimensional velocity models. *Science*, 253(5020), p.651.
- Michelini, A. and Lomax, A., 2004. The effect of velocity structure errors on double-difference earthquake location. *Geophysical Research Letters*, 31(9).
- Michelini, A. and McEvilly, T.V., 1991. Seismological studies at Parkfield. I. Simultaneous inversion for velocity structure and hypocenters using cubic B-splines parameterization. *Bulletin of the Seismological Society of America*, 81(2), pp.524-552.
- Monteiller, V., Got, J.L., Virieux, J. and Okubo, P., 2005. An efficient algorithm for double-difference tomography and location in heterogeneous media, with an application to the Kilauea Volcano. *Journal of Geophysical Research: Solid Earth*, 110(B12).
- Montone, P., Amato, A. and Pondrelli, S., 1999. Active stress map of Italy. *Journal of Geophysical Research: Solid Earth*, 104(B11), pp.25595-25610.
- Mora, M.M., Lesage, P., Valette, B., Alvarado, G.E., Leandro, C., Métaixian, J.P. and Dorel, J., 2006. Shallow velocity structure and seismic site effects at Arenal volcano, Costa Rica. *Journal of volcanology and geothermal research*, 152(1), pp.121-139.
- Morozov, I.B., 2008. Geometrical attenuation, frequency dependence of Q, and the absorption band problem. *Geophysical Journal International*, 175(1), pp.239-252.

- Mosegaard, K. and Tarantola, A., 1995. Monte Carlo sampling of solutions to inverse problems. *Journal of Geophysical Research: Solid Earth*, 100(B7), pp.12431-12447.
- Mostardini, F. and S. Merlini (2004), Appennino centro-meridionale. Sezioni geologiche e proposta di modello strutturale, Memorie della Società Geologica Italiana, 35,177-202.
- Noir, J., Jacques, E., Bekri, S., Adler, P.M., Tapponnier, P. and King, G.C.P., 1997. Fluid flow triggered migration of events in the 1989 Dobi earthquake sequence of Central Afar. *Geophysical Research Letters*, 24(18), pp.2335-2338.
- Nur, A. and Booker, J.R., 1972. Aftershocks caused by pore fluid flow?. *Science*, 175(4024), pp.885-887.
- Nur, A. and Simmons, G., 1969. Stress-induced velocity anisotropy in rock: An experimental study. *Journal of Geophysical Research*, 74(27), pp.6667-6674.
- Nur, A., 1972. Dilatancy, pore fluids, and premonitory variations of ts/tp travel times. *Bulletin of the Seismological society of America*, 62(5), pp.1217-1222.
- O'Connell, R.J. and Budiansky, B., 1974. Seismic velocities in dry and saturated cracked solids. *Journal of Geophysical Research*, 79(35), pp.5412-5426.
- O'Connell, D.R. and Johnson, L.R., 1991. Progressive inversion for hypocenters and P wave and S wave velocity structure: Application to The Geysers, California, geothermal field. *Journal of Geophysical Research: Solid Earth*, 96(B4), pp.6223-6236.
- O'Connell, R.J. and Budiansky, B., 1977. Viscoelastic properties of fluid-saturated cracked solids. *Journal of Geophysical Research*, 82(36), pp.5719-5735.
- Olson, E.L. and Allen, R.M., 2005. The deterministic nature of earthquake rupture. *Nature*, 438(7065), pp.212-215.
- Orsi, G., De Vita, S. and Di Vito, M., 1996. The restless, resurgent Campi Flegrei nested caldera (Italy): constraints on its evolution and configuration. *Journal of Volcanology and Geothermal Research*, 74(3-4), pp.179-214.
- Paige, C.C. and Saunders, M.A., 1982. LSQR: An algorithm for sparse linear equations and sparse least squares. *ACM transactions on Mathematical Software*, 8(1), pp.43-71.
- Valensise, G. and Pantosti, D., 2001. The investigation of potential earthquake sources in peninsular Italy: a review. *Journal of Seismology*, 5(3), pp.287-306.
- Patacca, E., Sartori, R. and Scandone, P., 1990. Tyrrhenian basin and Apenninic arcs: kinematic relations since late Tortonian times. *Mem. Soc. Geol. It*, 45(1), pp.425-451.
- Patacca, E., Scandone, P.A.O.L.O., Bellatalla, M., Perilli, N. and Santini, U., 1992. The Numidian-sand event in the Southern Apennines. *Mem. Sci. Geol. Padova*, 43, pp.297-337. Patacca & Scandone 2001
- Patacca, E. and Scandone, P., 2004. A geological transect across the Southern Apennines along the seismic line CROP 04. *Field trip guidebooks 32nd IGC. Memorie Descrittive Carta Geologica d'Italia, Florence*, 63, p.P20.
- Patanè, D., Barberi, G., Cocina, O., De Gori, P. and Chiarabba, C., 2006. Time-resolved seismic tomography detects magma intrusions at Mount Etna. *Science*, 313(5788), pp.821-823.
- Pavlis, G.L., 1986. Appraising earthquake hypocenter location errors: A complete, practical approach for single-event locations. *Bulletin of the Seismological Society of America*, 76(6), pp.1699-1717.

- Pescatore, T., Renda, P., Schiattarella, M. and Tramutoli, M., 1999. Stratigraphic and structural relationships between Meso-Cenozoic Lagonegro basin and coeval carbonate platforms in southern Apennines, Italy. *Tectonophysics*, 315(1), pp.269-286.
- Petrillo, Z., Chiodini, G., Mangiacapra, A., Caliro, S., Capuano, P., Russo, G., Cardellini, C. and Avino, R., 2013. Defining a 3D physical model for the hydrothermal circulation at Campi Flegrei caldera (Italy). *Journal of volcanology and geothermal research*, 264, pp.172-182.
- Podvin, P. and Lecomte, I., 1991. Finite difference computation of traveltimes in very contrasted velocity models: a massively parallel approach and its associated tools. *Geophysical Journal International*, 105(1), pp.271-284.
- Poupinet, G., Ellsworth, W.L. and Frechet, J., 1984. Monitoring velocity variations in the crust using earthquake doublets: An application to the Calaveras Fault, California. *Journal of Geophysical Research: Solid Earth*, 89(B7), pp.5719-5731.
- Pride, S.R. and Berryman, J.G., 1998. Connecting theory to experiment in poroelasticity. *Journal of the Mechanics and Physics of Solids*, 46(4), pp.719-747.
- Pride, S.R. and Berryman, J.G., 2003. Linear dynamics of double-porosity dual-permeability materials. I. Governing equations and acoustic attenuation. *Physical Review E*, 68(3), p.036603.
- Pride, S.R., 2005. Relationships between seismic and hydrological properties. In *Hydrogeophysics* (pp. 253-290). Springer Netherlands.
- Pride, S.R., Gangi, A.F. and Morgan, F.D., 1992. Deriving the equations of motion for porous isotropic media. *The Journal of the Acoustical Society of America*, 92(6), pp.3278-3290.
- Ratdomopurbo, A. and Poupinet, G., 1995. Monitoring a temporal change of seismic velocity in a volcano: Application to the 1992 eruption of Mt. Merapi (Indonesia). *Geophysical research letters*, 22(7), pp.775-778.
- Rawlinson, N. and Spakman, W., 2016. On the use of sensitivity tests in seismic tomography. *Geophysical Journal International*, 205(2), pp.1221-1243.
- Raymer, L.L., Hunt, E.R. and Gardner, J.S., 1980, January. An improved sonic transit time-to-porosity transform. In *SPWLA 21st annual logging symposium*. Society of Petrophysicists and Well-Log Analysts.
- Revil, A. and Florsch, N., 2010. Determination of permeability from spectral induced polarization in granular media. *Geophysical Journal International*, 181(3), pp.1480-1498.
- Rickett, J. and Lumley, D.E., 1998. A cross-equalization processing flow for off-the-shelf 4D seismic data. In *SEG Technical Program Expanded Abstracts 1998* (pp. 16-19). Society of Exploration Geophysicists.
- Rigo, A., Lyon-Caen, H., Armijo, R., Deschamps, A., Hatzfeld, D., Makropoulos, K., Papadimitriou, P. & Kassaras, I. 1996. A microseismic study in the western part of the Gulf of Corinth (Greece): Implications for large-scale normal faulting mechanisms, *Geophys. J. Int.*, 126, 663-688, doi 10.1111/j.1365-246X.1996.tb04697.x.
- Roure, F., Casero, P. and Vially, R., 1991. Growth processes and melange formation in the southern Apennines accretionary wedge. *Earth and Planetary Science Letters*, 102(3-4), pp.395-412.
- Rowe, C.A., Aster, R.C., Borchers, B. and Young, C.J., 2002. An automatic, adaptive algorithm for refining phase picks in large seismic data sets. *Bulletin of the Seismological Society of America*, 92(5), pp.1660-1674.
- Rumelhart, D.E., McClelland, J.L. and PDP Research Group. In *Parallel Distributed Processing: Explorations in the Microstructure of Cognition*, Vol. 1 . 12-21 (MIT Press, Cambridge MA, 1986).

- Saccorotti, G., Petrosino, S., Bianco, F., Castellano, M., Galluzzo, D., La Rocca, M., Del Pezzo, E., Zaccarelli, L. and Cusano, P., 2007. Seismicity associated with the 2004–2006 renewed ground uplift at Campi Flegrei Caldera, Italy. *Physics of the Earth and Planetary Interiors*, 165(1), pp.14-24.
- Scandone, P., 1972. *Studi di geologia lucana: carta dei terreni della serie calcareo-silico-marnosa e note illustrative*. S. Marellino.
- Schmoker, J.W. and Halley, R.B., 1982. Carbonate porosity versus depth: a predictable relation for south Florida. *AAPG bulletin*, 66(12), pp.2561-2570.
- Scholz, C.H., Sykes, L.R. and Aggarwal, Y.P., 1973. Earthquake prediction: A physical basis. *Science*, 181(4102), pp.803-810.
- Scrocca, D., Carminati, E. and Doglioni, C., 2005. Deep structure of the southern Apennines, Italy: Thin-skinned or thick-skinned?. *Tectonics*, 24(3).
- Serlenga, V., Lorenzo, S., Russo, G., Amoroso, O., Garambois, S., Virieux, J. and Zollo, A., 2016. A three-dimensional QP imaging of the shallowest subsurface of Campi Flegrei offshore caldera, southern Italy. *Geophysical Research Letters*, 43(21).
- Serra, M., Festa, G., Roux, P., Gresse, M., Vandemeulebrouck, J. and Zollo, A., 2016. A strongly heterogeneous hydrothermal area imaged by surface waves: the case of Solfatara, Campi Flegrei, Italy. *Geophysical Journal International*, 205(3), pp.1813-1822.
- Shapiro, S.A., Patzig, R., Rothert, E. and Rindschwentner, J., 2003. Triggering of seismicity by pore-pressure perturbations: Permeability-related signatures of the phenomenon. *Pure and applied geophysics*, 160(5-6), pp.1051-1066.
- Sibson, R.H., 1992. Implications of fault-valve behaviour for rupture nucleation and recurrence. *Tectonophysics*, 211(1-4), pp.283-293.
- Sissons, B.A. and Dibble, R.R., 1981. A seismic refraction experiment southeast of Ruapehu volcano. *New Zealand journal of geology and geophysics*, 24(1), pp.31-38.
- Stabile, T.A., Satriano, C., Orefice, A., Festa, G. and Zollo, A., 2012. Anatomy of a microearthquake sequence on an active normal fault. *Scientific reports*, 2.
- Stabile, T.A., Iannaccone, G., Zollo, A., Lomax, A., Ferulano, M.F., Vetri, M.L.V. and Barzaghi, L.P., 2013. A comprehensive approach for evaluating network performance in surface and borehole seismic monitoring. *Geophysical Journal International*, 192(2), pp.793-806.
- Stark, M.A., 1992. Microearthquakes—a tool to track injected water in The Geysers reservoir. *Monograph on the Geysers geothermal field, Special report*, (17), pp.111-117.
- Stark, M., 2003. Seismic evidence for a long-lived enhanced geothermal system (EGS) in the Northern Geysers Reservoir. *TRANSACTIONS-GEOTHERMAL RESOURCES COUNCIL*, pp.727-732.
- Stark, M.A. and Davis, S.D., 1996. Remotely triggered microearthquakes at The Geysers geothermal field, California. *Geophysical research letters*, 23(9), pp.945-948.
- Stark, M.A., 1990. Imaging injected water in The Geysers reservoir using microearthquake data. *Geothermal Resources Council Trans*, 14, pp.1697-1704.
- Talwani, P. and Acree, S., 1985. Pore pressure diffusion and the mechanism of reservoir-induced seismicity. In *Earthquake Prediction* (pp. 947-965). Birkhäuser Basel.
- Tarantola, A., 2005. *Inverse problem theory and methods for model parameter estimation*. Society for Industrial and Applied Mathematics.

- Thompson, R.C. and Gundersen, R.P., 1992. The orientation of steam-bearing fractures at The Geysers geothermal field. *Geotherm. Res. Council Special Rep*, 17, pp.65-68.
- Thurber, C., Roecker, S., Zhang, H., Baher, S. and Ellsworth, W., 2004. Fine-scale structure of the San Andreas fault zone and location of the SAFOD target earthquakes. *Geophysical Research Letters*, 31(12).
- Thurber, C.H., 1993. Local earthquake tomography: velocities and Vp/Vs-theory. *Seismic tomography: theory and practice*, pp.563-583.
- Toksöz, M.N., Cheng, C.H. and Timur, A., 1976. Velocities of seismic waves in porous rocks. *Geophysics*, 41(4), pp.621-645.
- Toksöz, M.N., Johnston, D.H. and Timur, A., 1979. Attenuation of seismic waves in dry and saturated rocks: I. Laboratory measurements. *Geophysics*, 44(4), pp.681-690.
- Toomey, D.R. and Foulger, G.R., 1989. Tomographic inversion of local earthquake data from the Hengill-Grensdalur central volcano complex, Iceland. *Journal of Geophysical Research: Solid Earth*, 94(B12), pp.17497-17510.
- Tramelli, A., Del Pezzo, E., Bianco, F. and Boschi, E., 2006. 3D scattering image of the Campi Flegrei caldera (Southern Italy): new hints on the position of the old caldera rim. *Physics of the Earth and Planetary Interiors*, 155(3), pp.269-280.
- Trippetta, F., Collettini, C., Barchi, M.R., Lupattelli, A. and Mirabella, F., 2013. A multidisciplinary study of a natural example of a CO₂ geological reservoir in central Italy. *International Journal of Greenhouse Gas Control*, 12, pp.72-83.
- Utsu, T., 1992. On seismicity. *Report of the Joint Research Institute for Statistical Mathematics*, 34, pp.139-157.
- Valoroso, L., Chiaraluce, L., Piccinini, D., Di Stefano, R., Schaff, D. and Waldhauser, F., 2013. Radiography of a normal fault system by 64,000 high-precision earthquake locations: The 2009 L'Aquila (central Italy) case study. *Journal of Geophysical Research: Solid Earth*, 118(3), pp.1156-1176.
- Valoroso, L., Improta, L., De Gori, P. and Chiarabba, C., 2011. Upper crustal structure, seismicity and pore pressure variations in an extensional seismic belt through 3-D and 4-D VP and VP/VS models: The example of the Val d'Agri area (southern Italy). *Journal of Geophysical Research: Solid Earth*, 116(B7).
- Vanorio, T., Virieux, J., Capuano, P. and Russo, G., 2005. Three-dimensional seismic tomography from P wave and S wave microearthquake travel times and rock physics characterization of the Campi Flegrei Caldera. *Journal of Geophysical Research: Solid Earth*, 110(B3).
- Vesnaver, A.L., Accaino, F., Bohm, G., Madrussani, G., Pajchel, J., Rossi, G. and Moro, G.D., 2003. Time-lapse tomography. *Geophysics*, 68(3), pp.815-823.
- Wadati, K. and Oki, S., 1933. On the travel time of earthquake waves.(Part II). *Journal of the Meteorological Society of Japan. Ser. II*, 11(1), pp.14-28.
- Waldhauser, F. and Ellsworth, W.L., 2000. A double-difference earthquake location algorithm: Method and application to the northern Hayward fault, California. *Bulletin of the Seismological Society of America*, 90(6), pp.1353-1368.
- Wasserman, P.D., 1989. *Neural computing* (pp. 44-54). Van Nostrand Reinhold, New York.
- Whitcomb, J.H., Garmany, J.D. and Anderson, D.L., 1973. Earthquake prediction: Variation of seismic velocities before the San Francisco earthquake. *Science*, 180(4086), pp.632-635.
- Winkler, K. and Nur, A., 1979. Pore fluids and seismic attenuation in rocks. *Geophysical Research Letters*, 6(1), pp.1-4.

- Wyllie, M.R.J., Gregory, A.R. and Gardner, L.W., 1956. Elastic wave velocities in heterogeneous and porous media. *Geophysics*, 21(1), pp.41-70.
- Zollo, A., D'auria, L., De Matteis, R., Herrero, A., Virieux, J. and Gasparini, P., 2002. Bayesian estimation of 2-D P-velocity models from active seismic arrival time data: imaging of the shallow structure of Mt Vesuvius (Southern Italy). *Geophysical Journal International*, 151(2), pp.566-582.
- Zollo, A., Maercklin, N., Vassallo, M., Dello Iacono, D., Virieux, J. and Gasparini, P., 2008. Seismic reflections reveal a massive melt layer feeding Campi Flegrei caldera. *Geophysical Research Letters*, 35(12).
- Zollo, A., Orefice, A. and Convertito, V., 2014. Source parameter scaling and radiation efficiency of microearthquakes along the Irpinia fault zone in southern Apennines, Italy. *Journal of Geophysical Research: Solid Earth*, 119(4), pp.3256-3275.
- Zucca, J.J., Hutchings, L.J. and Kasameyer, P.W., 1994. Seismic velocity and attenuation structure of the Geysers geothermal field, California. *Geothermics*, 23(2), pp.111-126.